APPLIED STUDY AND MODELING OF PENETRATION DEPTH FOR SLOT DIE COATING ONTO POROUS SUBSTRATES

A Dissertation
Presented to
The Academic Faculty

By

Xiaoyu Ding

In Partial Fulfillment
Of the Requirements for the Degree
Doctor of Philosophy in Mechanical Engineering

Georgia Institute of Technology

May 2014

Approved by:

Dr. Tequila A. L. Harris, Advisor
G.W. Woodruff School of Mechanical Engineering
Georgia Institute of Technology

Dr. Thomas F. Fuller, Advisor
School of Chemical & Bimolecular Engineering
Georgia Institute of Technology

Dr. Marc K. Smith
G.W. Woodruff School of Mechanical Engineering
Georgia Institute of Technology

Dr. Victor Breedveld
School of Chemical & Bimolecular Engineering
Georgia Institute of Technology

Dr. Yan Wang
G.W. Woodruff School of Mechanical Engineering
Georgia Institute of Technology

Date Approved: 02/20/2014

谨以此文献给我的母校清华：

自强不息，厚德载物。

ACKNOWLEDGEMENTS

First, I would like to thank my advisers Dr. Harris and Dr. Fuller, who changed my life by giving me the opportunity to join their research groups. I am really thankful for their advice, guidance and mentorship during my Ph.D. study. Without their continuous support I would not be able to accomplish my research tasks.

I would like to extend my appreciation to committee members: Dr. Smith, Dr. Breedveld and Dr. Wang for providing valuable research advice and insightful comments for the improvement of this work.

I would also like to thank Sima Didari, Brain Setzler and Erin Redmond for their collaboration in several parts of this work.

My parents, Yunhua Ding and Rulan Wang, have always been very supportive of my work and assisted enormously towards my personal, professional and spiritual development. I can never thank you enough for all of your love and encouragement during these years.

TABLE OF CONTENTS

LIST OF TABLES

LIST OF FIGURES

NOMENCLATURE

A_t	Area of a carbon paper sample
c	Coefficient of the model of break line boundary
Ca	Capillary number
g	Acceleration of gravity
h	Penetration depth
h_0	Penetration depth at $x = 0$
h_f	Final penetration depth at the outlet
h_j	Penetration depth at each control point
H	Stand-off height
j	Index of each control point
k	Permeability of porous media
L_1	Left channel length
L_2	Right channel length
m	Consistency index of apparent viscosity of a non-Newtonian fluid
m_1	Pressure gradient in the left channel for coating a Newtonian fluid
m_2	Pressure gradient in the right channel for coating a Newtonian fluid
m_3	Pressure gradient in the left channel for coating a non-Newtonian fluid
m_4	Pressure gradient in the right channel for coating a non-Newtonian fluid
n	Flow behavior index of apparent viscosity of a non-Newtonian fluid
p	Pressure
p_{air}	Reference pressure of air

p_c	Capillary pressure
p_j	Pressure at each control point
p_{liquid}	Pressure at the front of penetrated fluid
p_{max}	Maximum pressure at the center slot
$p_{non\text{-}wetting}$	Pressure of non-wetting phase
$p_{wetting}$	Pressure of wetting phase
q_1	Flow rate in left channel
q_2	Flow rate in the right channel
Q	Inlet volumetric flow rate of slot coating
Q_1	A fixed flow rate
Q_{bh}	Highest flow rate on the break line boundary
Q_{bl}	Lowest flow rate on the break line boundary
r	Average pore radius
R_{hf}	Ohmic Resistance
R_m	Membrane Resistance
R_{bulk}	Electronic resistance of all other current-carrying components except membrane
$R_{contact}$	Contact resistance
Δs	Interval distance between adjacent control points
t	Wet thickness of a coated film
t_{min}	Minimum wet thickness of a coated film
Δt	Interval time moving from one control point to next
u_j	Vertical velocity at each control point

u_x	Horizontal moving speed of the leaking wall
u_y	Vertical leaking speed of the leaking wall
v_p	Penetration velocity
V	Coating speed
V_b	Coating speed of break line boundary
V_h	Coating speed of air entrainment boundary
$V_{h\text{-}p}$	Coating speed of air entrainment boundary for a porous substrate
$V_{h\text{-}s}$	Coating speed of air entrainment boundary for a solid substrate
V_l	Coating speed of dripping boundary
$V_{l\text{-}p}$	Coating speed of dripping boundary for a porous substrate
$V_{l\text{-}s}$	Coating speed of dripping boundary for a solid substrate
W	Slot width
x	Coordinate along the coating direction
X_1	Left die lip length
X_2	Right die lip length
y	Coordinate vertical to the coating direction
I, II, III	Index of regions of coating on a porous medium
1, **2**, **3**	Index of regions of coating window
A, B, B_c, C, C_c, D, E, F, G, and I	Variables defined in analytical expressions of final penetration depth
M_t, M_f, and M_p	Weight variables defined in the measurement of penetration depth

s_1, s_2, s_3, and s_4	Position variables defined in derivation of penetration depth for a negative capillary pressure

Greek letters

ε	Porosity of porous media
μ	Viscosity of a Newtonian fluid
μ_{app}	Apparent viscosity of a non-Newtonian fluid
μ_{eff}	Effective viscosity defined in Blake-Kozeny equation
$\bar{\mu}$	Viscosity term defined in non-Newtonian lubrication equation
α	Contact angle on the substrate
β	Contact angle on the die
ρ	Fluid density
ρ_a	Area density of carbon paper
σ	Surface tension
θ	Contact angle of coating fluid on the surface of carbon paper

π_1, π_2, π_3, π_4, π_5, π_6	Dimensionless pi-terms

SUMMARY

A distinctive field in the coatings industry is the coating of porous media, with broad applications in paper, apparel, textile, electronics, bioengineering, filtration and energy sector. A primary industrial scale process that can be used to coat porous media in a fast and flexible manner is slot die extrusion. A major concern when coating porous media with a wetting fluid is fluid penetration into the substrate. Although some level of penetration is desirable to obtain specific material properties, inadequate or excessive fluid penetration can negatively affect the strength, functionality or performance of the resulting material. In spite of its apparent industrial importance, limited modeling and experimental work has been conducted to study fluid penetration into porous media during fabrication. The effects of processing parameters on the penetration depth, the effects of penetration on material quality, and the method to predict and control the penetration depth are not well understood. This dissertation is composed of two parts.

Part I is an applied study for coating onto porous media. This part focuses on the first objective of this dissertation which is to elucidate clearly the feasibility, advantages and disadvantages of the direct coating method as a potential fabrication route for membrane electrode assembly (MEA). MEA samples are fabricated using both traditional and the direct coating methods. Then, the quality and performance of the MEA samples are examined. Experimental results in Part I demonstrate that it is feasible to fabricate MEAs using the direct coating method. However, Nafion® solution penetrates into the catalyst layer during the coating process and causes lower performance of fuel cells, which is the motivation for Part II of this thesis.

The objective of Part II is to fundamentally understand the fluid penetration process and predict the penetration depth when directly coating porous media, using a comprehensive approach. A series of computational and analytical models are developed to predict the penetration depth for both Newtonian and non-Newtonian fluids with or without capillary pressure. Finally the accuracy of developed models are validated through experiments. The relative error between the predicted and experimentally measured penetration depth is generally lower than 20%.

CHAPTER 1. INTRODUCTION

1.1 Application of coating porous media

Coating porous media is a distinctive field in the coating industry which has broad applications including paper, textiles, electronics, filtration and energy sectors. In the paper industry, coatings have been found to improve the surface appearance by providing smooth, glossy and colored surfaces [1-3]; and also to improve printability by aiding the transfer and setting of the printed ink [4-6]. In addition, coated layers have been shown to provide protective or functional properties for papers, such as resistance to grease, moisture, ultraviolent radiation, pollutant gasses, mold and bacteria [7]. The market for specialty chemicals used for paper production is about $16 billon, majority of which is attributed to chemicals used as coatings [8].

In the textile and clothing industry, coating has been widely used to reinforce the fabrics [9, 10] or provide other special functions and properties. For example, phase-change materials or silicon carbide coatings have been shown to provide thermal insulation for sporting clothes to maintain a suitable temperature for the human body [11]. Polyurethane (PU) coatings have been used to add a breathable waterproof property to clothes [12]. A back coating such as acrylic resin loaded with ammonium polyphosphate has been shown to have fire retardance property for textiles [13]. Coating conductive polymer such as poly(3,4-ethylenedioxythiophene) (PEDOT) has been used to produce electro-active fabrics [14]. The coated fabric industry is about $3 billion in the US alone [15].

1.2 Objectives

The overall motivation of this thesis is to determine and investigate key technical

issues related with coating porous media by experimental, modeling and analytical work.

1.2.1 Manufacturing of polymer electrolyte membrane fuel cells

In addition to applications in the paper, textile and clothing industries, coating porous media also has broad potential applications in other fields such as electronics [16], bioengineering, filtration [17, 18] and in the energy sector to fabricate functional multilayer structures. One typical example is polymer electrolyte membrane (PEM) fuel cells. Polymer electrolyte membrane (PEM) fuel cells are a prominent energy source for portable and transportation applications that require clean, quiet, and efficient power.[19] Significant advances in research and development have been made over the last several decades;[19] however, slow fabrication speeds and high fabrication costs[20] still remain significant barriers to the extensive commercialization of PEM fuel cells.

The basic physical design of a single PEM fuel cell consists of two bipolar plates sandwiching one membrane electrode assembly (MEA). A number of cells are connected in series to form a fuel-cell stack. The MEA is constructed from two gas diffusion layers (GDLs), two catalyst layers (typically containing platinum, carbon, and ionomer) and one electrolyte membrane. As the place for oxidation and reduction half reactions, the MEA plays a key role in a fuel cell; its characteristics and quality directly determine the overall performance of an individual cell or a stack. In addition, an extremely large quantity of MEAs will be required to realize widespread use of PEM fuel cells. For example, hundreds of millions MEAs per year would be needed to supply the laptop computer market.[21] Considering other potential big markets, such as the transportation and electronics sectors, the demand for mass production of MEAs will be a critical issue to the commercialization of PEM fuel cells.

MEAs are traditionally manufactured by two methods, the membrane-based method or the GDL-based method.[22] Both manufacturing methods are difficult to employ for mass production of MEAs due to various problems or limitations, so the manufacturing has been largely conducted by hand[23]. Furthermore, in traditional methods, the membrane has to be produced separately prior to the assembly, using processes such as extrusion or casting.[24, 25] This separate fabrication process makes the whole production line of MEAs more complex.

In order to overcome the limitations of traditional methods, another category of MEA fabrication techniques which are characterized by direct coating of the membrane solution onto the catalyzed GDL has become of interest.[26-31] The direct coating method eliminates the separate membrane fabrication process before assembly, thus it has the potential to facilitate integrating the whole production line of MEA. Furthermore, compared to the GDL-based method, these methods are expected to enhance the contact between the catalyst layer and membrane. However, this category of method is only conceptual in some patents [26-31], and little information about the manufacturing process is available, thus detailed studies are required for implementation. For example, characteristics and performance of the MEA fabricated by the direct coating method must be researched to determine the effectiveness of the new method. In addition, the penetration of the membrane solution into catalyst layer and its effect on the performance of the fuel cell have to be examined and analyzed.

To this end, **the first objective of current study is to elucidate the feasibility, advantages and disadvantages of the direct coating method as a potential fabrication route for MEA in PEM fuel cells.** In current study, a new MEA fabrication

process based on directly coating membrane solution onto porous catalyzed GDL is first presented. Then, the quality and performance of the MEA samples are examined. Three important quality issues have been studied, membrane uniformity, membrane penetration and annealing condition. All factors if not properly controlled can impact the performance of the fuel cell.

1.2.2 Fluid penetration during coating on porous media

The fluid penetration into porous substrates is not only significant because it affects the performance of fuel cells but also as an important common technical issue in the whole coating industry. Hence, a deeper study specifically on the penetration issue of coating porous media is warranted.

In general, when coating a porous medium, some level of the penetration is usually desirable to obtain specific material properties, but inadequate or excessive penetration is limiting. For textile coating, penetration directly affects the bond strength between coated layer and the substrate [15]. If the penetration depth is too low the desired adhesion of coating to the substrate will not be obtained. For paper printing and coating, penetration of ink directly affects the appearance of the printed paper [32, 33]. Low penetration can cause ink peel-off [34]; while severe penetration can degrade the surface smoothness [1]. In addition, penetration depth also affects the functionality and performance of the resulting material [35]. Penetration also changes the coating parameters needed for a desired film thickness and the operational limits of the coating process, thus affecting the cost of production. Both too high or too low can lead to unwarranted expense [36]. Therefore, predicting and controlling penetration depth during direct coating on porous media is not only significant in assuring the desired appearance, properties, and

performance of the resulting material, but also important in controlling the cost of production. However, in spite of this apparent importance, limited studies exist to fundamentally understand the penetration process and to predict the penetration depth based on industrial scale coating processes. To date, the analytical relationship between processing parameters and final penetration depth is not well understood. Further, the effect of penetration on the operational limits of coating process has not been studied.

To this end, **the second objective of current research is to fundamentally understand the fluid penetration process and predict the penetration depth during direct coating on porous media using a holistic methodology (computational and analytical modeling and experimental validation).** It is hypothesized that by understanding the correlation between the porous media, the coating fluid, and the coating process, the penetration depth of the fluid into the porous medium can be predicted. Both Newtonian and non-Newtonian fluids will be studied.

1.3 Selection of the coating process

Several industry scale processes have been used for coating porous media such as roll coating [37], blade coating [38, 39], dip coating [40] and slot die coating [36, 41, 42]. All of them are well-known high-speed coating techniques suited for mass production. However, if the thickness of the coated layer needs to be controlled precisely, slot die coating is usually preferred because it is a pre-metered process [43]. Another major benefit of slot die coating is that multiple layers can be coated simultaneously [44, 45]. Recently the effectiveness of slot die coating has been demonstrated in the manufacture of polymer solar cells [46-48], which is a typical multilayer structure. **In the current study only slot**

die coating is investigated, but the framework and conclusions may be extended to similar coating processes, such as roll coating and blade coating.

1.4 Research questions and tasks

Based on above discussion, this study has two parts. The first part is an applied study of coating on porous media to investigate the feasibility, effectiveness and efficiency of the new MEA manufacturing technique based on direct coating porous catalyzed GDL. The second part is modeling fluid penetration depth while coating porous substrates. In order to fulfill two general research objectives, following research questions will be explored:

Manufacture of multilayer materials by direct coating

- Can multilayer functional materials composed of porous media and thin films be made by using advanced roll-to-roll manufacturing processes?
- What impact does direct coating of thin films onto porous media have on the performance of devices, such as PEM fuel cells that utilize multilayer functional materials?

Modeling of penetration depth:

- What are the analytical relationships between penetration depth and processing parameters for Newtonian and non-Newtonian fluids directly slot coated onto porous media? Critical parameters that may impact the penetration include coating conditions (flow rate, coating speed and geometry of slot die setting), characteristics of porous media (permeability and porosity) and properties of coated fluids (viscosity, capillary force, etc.).

- Does there exist an upper and lower coating boundary that provides an understanding of coating defects that will originate in the material during fabrication?

To answer above research questions, following experimental, modeling and analytical work will be conducted:

Manufacture of MEA based on direct coating:

- Developing a new MEA fabrication procedure based on directly coating membrane solution onto catalyzed GDL.
- Experimentally studying the uniformity and penetration of membrane coated onto catalyzed GDL.
- Experimentally studying the effects of annealing time and humidity on the performance of solution cast polymer electrolyte membrane.
- Experimentally studying the characteristics and performance of MEA samples made by the new fabrication procedure.

Modeling of penetration depth:

- Building computational fluid dynamics (CFD) models to simulate the slot die coating on porous media.
- Developing analytical models to predict the final penetration depth without/with considering the capillary effect and initially validating the analytical results by comparing them with the results from the CFD models.
- Investigating the effects of different processing parameters on penetration depth using the developed models.
- Experimentally validating the developed models.

- Developing models of operational limits for slot die coating on solid and porous substrates based on analytical analysis and numerical simulation.

1.5 Thesis Layout

This thesis is composed of two parts. Part I, which includes Chapter 2-4, is an applied study on coating porous media. The aim is to understand the feasibility, effectiveness and efficiency of a new MEA manufacturing technique based on direct coating membrane solution onto porous catalyzed GDL. In Part II, which includes Chapter 5-9, modeling the penetration depth of a fluid while coating porous media is the focus.

In Chapter 2, a new MEA fabrication procedure based on directly coating membrane solution onto catalyzed GDL is presented. The uniformity and penetration of membrane into catalyzed GDL is experimentally studied.

In Chapter 3, the effects of annealing time and humidity on the performance of solution cast polymer electrolyte membrane are experimentally studied.

In Chapter 4, the characteristics and performance of MEA samples made by the new fabrication procedure are experimentally studied.

In Chapter 5, some backgrounds and literature review of coating onto porous media are provided.

In Chapter 6, computational fluid dynamics (CFD) models to simulate the slot die coating onto porous media are built, and a case study is conducted to illustrate the characteristics of penetration process.

In Chapter 7, a series of analytical models to predict the final penetration depth without/with considering the capillary effect are developed.

In Chapter 8, a series of models of operational limits for slot die coating on solid and porous substrates are developed based on analytical analysis and numerical simulation. Some of the models are experimentally validated.

In Chapter 9, developed models of penetration depth are validated numerically and experimentally. Then, the effects of different processing parameters on penetration depth are studied using the models.

In Chapter 10, the contributions of current study are presented. A discussion on how the current study can be further extended in the future is also provided.

PART I: APPLIED STUDY FOR SLOT DIE COATING ONTO POROUS MEDIA

Part I is an applied study for coating onto porous media, which is based on published work by Ding et al. [49-52]. This part focuses on the first objective of this dissertation which is to elucidate clearly the feasibility, advantages and disadvantages of the direct coating method as a potential fabrication route for MEA. Specifically, a new MEA fabrication process based on directly coating membrane solution onto porous catalyzed GDL is first presented. Then, the quality and performance of the MEA samples are examined. Three important quality issues are studied, membrane uniformity, membrane penetration and annealing condition. All factors if not properly controlled can impact the performance of the fuel cell. Fulfillment of this research objective will have a direct impact on the PEM fuel cells manufacturing industry, providing valuable data and guidance for the mass production of PEM fuel cells in a cost efficient way.

CHAPTER 2. FEASIBILITY OF MEA FABRICATION USING DIRECT COATING CATALYZED GDLS

2.1 Introduction

As discussed in Chapter 1, PEM fuel cells are a prominent energy source for portable and transportation applications that require clean, quiet, and efficient power. Key components of a PEM fuel cell are depicted in Figure 2.1. The basic physical design consists of two electrodes (a negative anode and a positive cathode), which are separated by the membrane material. The construction of two gas diffusion layers, membrane, and two catalyst layers (typically platinum) is typically referred to as a MEA. Then, the MEAs are placed between two electrically conductive bipolar plates to create a single PEM fuel cell.

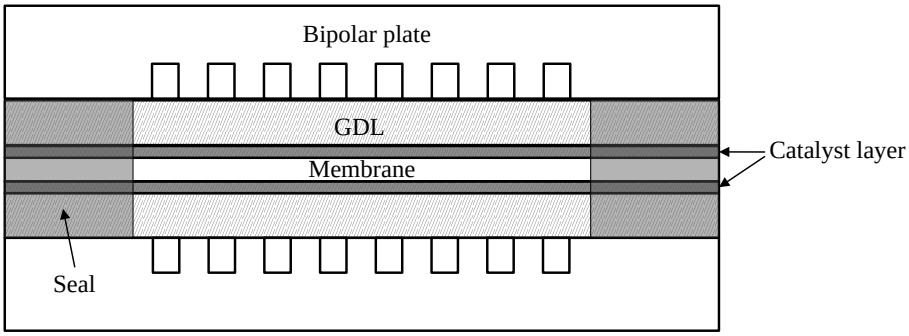

Figure 2.1 Schematic structure of a single typical PEM fuel cell.

As the place for oxidation and reduction half reactions, the MEA plays a key role in a fuel cell; its characteristics and quality directly determine the overall performance of an individual cell or a stack. In addition, the demand for mass production of MEAs will be a critical issue to the commercialization of PEM fuel cells.

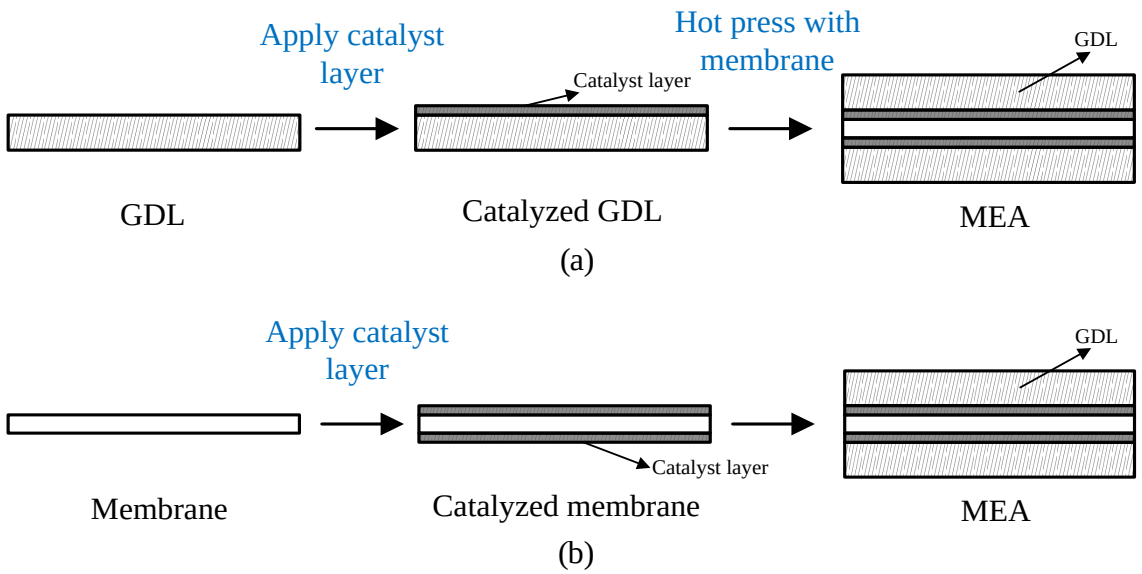

Figure 2.2 Schematic of traditional MEA fabrication methods. (a) GDL-based method and (b) membrane-based method

MEAs are traditionally manufactured by two methods, GDL-based method and the membrane-based method.[22] As shown in Figure 2.2(a), in the GDL-based method, a catalyst layer is applied onto one side of the GDL forming a catalyst-coated GDL (CCG).[53] Then, the electrolyte membrane is sandwiched between two CCGs under high temperature and pressure to form the MEA. Because the bond is generated by hot pressing a solid catalyst layer to the membrane, one problem this method can encounter is the relatively low contact area between the membrane and catalyst layer. Tang et al. showed that MEAs made from hot pressing have higher contact resistance and charge-transfer resistance as compared with those made from catalyzed membrane.[54] Good cell performance requires good contact, or more specifically that the high frequency resistance is low and the electrochemical active area (ECA) is high. Attempts have been made to overcome this problem. For example, Han et al. patented an approach whereby a metal layer is randomly deposited on membrane that has specific surface roughness to

strengthen the adherence between the membrane and catalyst layer.[55] However, processes employing such treatment will be more complex and difficult to control; and, the high pressure required may crush the fibers in the electrode, thus reducing gas permeability.

In the membrane-based method, the catalyst layers are initially applied onto both sides of the membrane to get the catalyst coated membrane (CCM). Then the CCM is deposited between two GDLs with or without hot-pressing. The schematic of membrane-based method is shown in Figure 2.2(b). Up to now, two techniques have been employed to apply catalyst material onto the membrane. One is characterized by direct deposition, the other one is characterized by indirect deposition. In the direct deposition method, a catalyst ink/slurry is directly applied onto the membrane.[56-59] Usually a spray coating technique is used, since good contact between the catalyst layer and membrane can be obtained, resulting in lower ionic resistance and better performance. However, the processing time is extensive, because repeated spraying operations are required to obtain the necessary catalyst loading and thickness. Furthermore, considerable valuable catalyst material can be lost while spraying. Faster coating techniques, such as slot die coating, roll coating and blade coating, etc., can be employed to increase the production rate. However, these techniques will have manufacturing limitations too. One challenge is that the membrane will swell and deform when it is in direct contact with a large amount of ink/slurry containing solvents. This swelling causes handling difficulties and a non-uniform catalyst layer distribution.[60] Hence, without extensive research the direct deposition method is difficult to employ for mass production operation.

The indirect deposition method is usually referred to as the decal method. Here, the catalyst ink/slurry is coated onto another substrate (backing film) first. After drying, the catalyst layer is transferred to the membrane by hot pressing.[61] An advantage of this technique is that membrane swelling and deformation problems are minimized. However, the manufacturing cost will be increased due to the use of release film and the introduction of the hot pressing operation. Compared with the GDL-based technique the decal method results in lower area of contact between the catalyst layer and membrane.

In order to overcome the limitations of traditional methods, another category of MEA fabrication techniques which are characterized by direct coating of the membrane onto the catalyst layer has become of interest.[26-31] When two MEA halves (i.e., coated anode side and coated cathode side) are hot pressed to form an MEA the internal resistance has been found to increase.[26, 27] Grot combined the decal transfer method with direct coating and hot pressing, which resulted in increased production cost and manufacturing complexity.[28, 29] Uchida et al. [30] and O'Brien et al., [31] directly coated on catalyst decals without hot pressing. They coated a second catalyst layer onto the top-side of the membrane and then later attached the GDLs to form the MEA. The direct coating method eliminates the separate membrane fabrication process before assembly, thus it has the potential to facilitate integrating the whole production line of MEA. Furthermore, compared to the GDL-based method, these methods are expected to enhance the contact between catalyst layer and membrane. However, this category of method is only conceptual in some patents [26-31], and little information about the manufacturing process is available, thus detailed studies are required for implementation.

For example, characteristics and performance of the MEA fabricated by the direct coating method must be researched to determine the effectiveness of the new method.

There are advantages and disadvantages of each MEA fabrication approach. Therefore, rather than promote one approach over another, the objective of this study is to elucidate clearly the feasibility, advantages and disadvantages of the direct coating method as another potential fabrication route. In this Chapter, a new MEA fabrication process based on directly coating membrane solution onto catalyzed GDL is first presented. Then, the feasibility of this method is studied by examining the membrane uniformity and membrane penetration into the catalyzed GDL. Both factors if not properly controlled can negatively impact the performance of the MEA. The uniformity of the coated membrane will directly affect the bond quantity between the membrane and the "top" GDL and consequently the final performance of the MEA. The penetration of membrane will change the weight ratio between ionomer and platinum; subsequently altering the balance of the ionic conductivity and electronic conductivity as well as gas access.

2.2 Materials

Nafion® D2021 with 20-22 wt% polymer content was purchased from Ion Power and used as the membrane solution. Material properties that have significant effects on coating process were measured. Surface tension was measured as 0.024 N/m by using the pendent drop method. The static contact angle on Toray 060 carbon paper was 12° measured with the sessile drop technique. A TA Instrument ARES rheometer was used to measure the viscosity, where it was found that the solution is shear-thinning with flow consistency index m = 4.335 Pa s^n and flow behavior index n = 0.52. Toray 060 carbon

paper was chosen as the GDL purchased from Fuel Cell Earth. The GDL was pretreated with a micro-porous layer (MPL) and catalyst layer with a Pt loading 0.5 mg/cm^2 by the supplier.

2.3 Slot die coating

A continuous Roll-feed Imaging System (RFIS), as depicted in Figure 2.3, was used to facilitate the MEA coating process. As shown, the RFIS is a roll-to-roll system capable of conducting full-scale automated extrusion in a controlled environment consisting of a sealed chamber, temperature, speed, and environmental controls. The solution of membrane material, which is stored in container, is forced through the slot die by the high pressure from the nitrogen tank. The flow rate is controlled by adjusting the pressure from the tank. Finally the solution is coated onto the moving PET substrate that carries the catalyzed GDL.

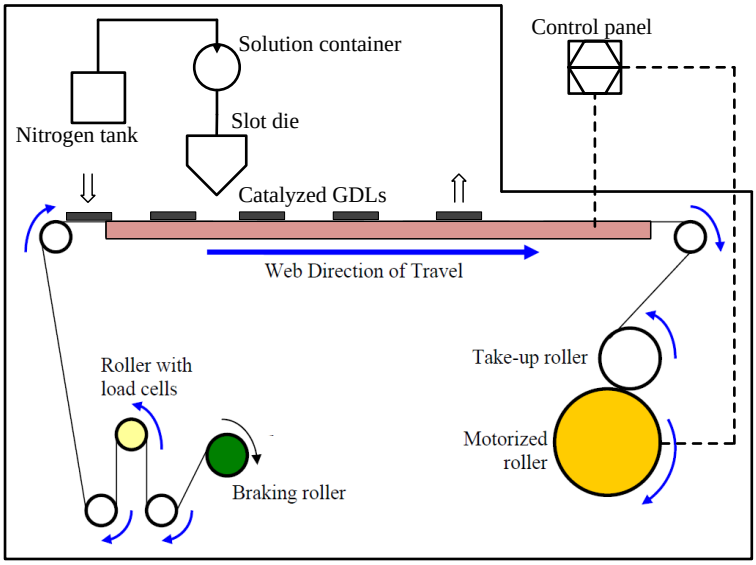

Figure 2.3 Schematic diagram of the roll feed imaging system used for coating GDLs. [50]

An important component of the RFIS is the slot die, because the final quality of the membrane is influenced by its geometry. Generally, slot die coating allows for a pre-metered amount of fluid to be dispensed in a controlled manner (e.g. deposited thickness) at relatively high speeds for low viscosity materials such as the Nafion® dispersion. In addition, slot die coating has been shown to be flexible, repeatable, and to produce highly uniform defect-free film.[44, 62, 63]

A schematic depicting a localized view of the slot die coating process and the most influential parameters is shown in Figure 2.4. The membrane solution is delivered at a constant flow rate, *Q*, from a fixed gap, *W*, on the slot die. The slot die produces a uniform and stable coating bead onto the moving catalyzed GDL with a coating speed, *V*. After drying, a membrane will be formed on the catalyst layer.

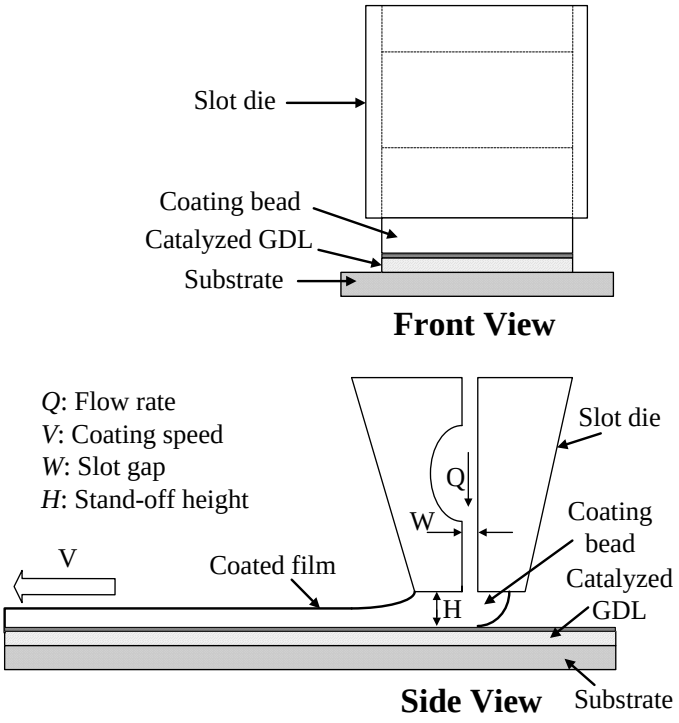

Figure 2.4 Schematic illustrating the slot die coating of membrane solution onto a catalyzed GDL. [50]

Although the coating speed for the slot die coating can be fast and the overall quality of the film uniform and defect free, there are limitations. There is a relationship between flow rate and coating speed for which high quality coatings void of defects can be obtained, known as the coating window[44, 62, 63]. In order to have good coating, the flow rate and coating speed must be confined within the upper and lower coating window boundaries, where for a given flow rate there exist a minimum and maximum coating speed. Common coating defects of extrusion slot coating are air entrainment, dripping, ribbing, breaking lines, pinholes, and holes[64], which are influenced by viscosity, surface tension, geometrical variables of the slot die such as slot gap and coating gap and surface roughness. The coating window for slot die coating onto solid and porous substrates will be discussed in detail in Chapter 8.

2.4 MEA fabrication procedure

The MEA fabrication process is depicted in Figure 2.5. The general steps include: 1) directly coating the membrane solution onto the catalyzed GDL by forcing the material through the slot, forming a membrane layer on the catalyzed GDL. 2) Drying and annealing the first membrane layer. 3) Assembling the MEA. This can be done in various ways. One option is directly coating another catalyst layer on top of the first cured membrane layer. Then another GDL is applied onto the catalyst layer with or without hot pressing. Another option is hot-pressing another catalyzed GDL onto the membrane. 4) Sealing the MEA. This also can be done in various ways. One of them is impregnating sealant material into the edge zone of the MEA[65, 66]. The number of fabrication steps compared to the conventional MEA manufacturing process is expected to be reduced, since for example the membrane will not require a separate fabrication process.

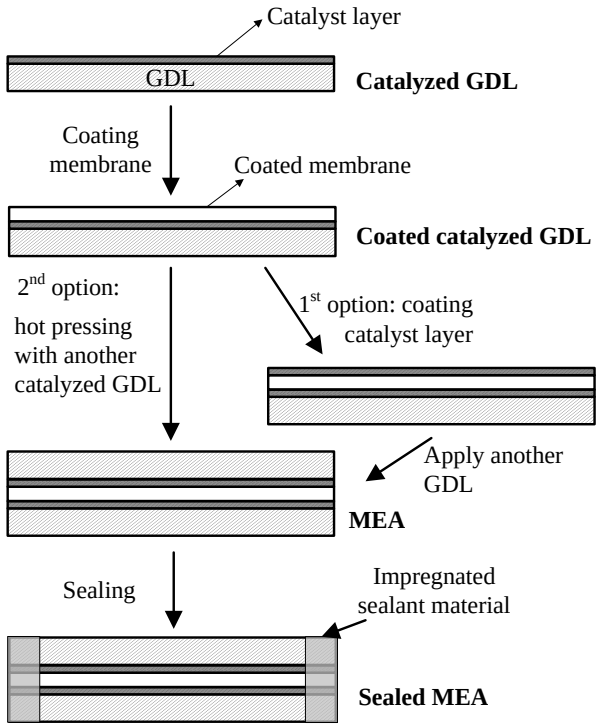

Figure 2.5 Schematically detailed procedure of the new MEA fabrication technique. [50]

All coating tests were conducted at room temperature, 25℃. Slot gap, stand-off height and slot width were fixed as 0.254 mm, 0.406 mm and 50.80 mm, respectively. The flow rate of the Nafion® dispersion was 2.3 ml/min. As mentioned above, there will be a range of proper coating speeds that allow for defect-free coated membrane. In order to determine this range, coating tests were conducted on glass plates. It was found that the coating process did not cause macroscopic defects at coating speeds between 0.5 to 0.6 cm/s.

Preliminary coating tests were conducted on the purchased catalyzed GDL with MPL in order to evaluate the quality of the coated membrane. Each sample was cut to 1 x 1 cm^2 and directly coated under a 5 cm slot opening to form the coated membrane on catalyst layer. A coating speed of 0.6 cm/s was used. After coating, samples were

immediately extracted from the substrate and left in the room environment for at least 10 hours to dry. Two important quality issues were investigated, membrane uniformity and membrane penetration into the catalyzed GDL. To study the uniformity of the membrane, surface and cross-section morphology of the coated membranes were observed by Microscope (Nikon: Eclipse E600) and scanning electron microscopy (SEM: Hitachi S-3700N VP-SEM). Energy-dispersive X-ray spectroscopy (EDX) tests were conducted to qualify and quantify the penetration of Nafion® into the catalyst layer by analyzing the percentage of fluorine present in catalyst layer.

2.5 Uniformity of coated membrane

An SEM image of the cross section of a purchased catalyzed GDL is shown in Figure 2.6(a). The MPL, catalyst, and carbon paper can be clearly seen. As depicted, there are large cracks and the surface is not uniform. These cracks may be related to the processing technique used to make the sample, which is not disclosed by the provider. A microscopic top view of the Nafion® coated GDL is shown in Figure 2.6(b), where more visible cracking across the surface can be seen. To verify the presence of the Nafion®, SEM images were taken as shown in Figure 2.6(c) – (d). It is evident from these images that the Nafion® dispersion was coated on the surface of the catalyzed GDL. However, the coated membranes on the catalyzed GDLs were non-uniform because of the surface roughness and quality of the uncoated samples, such as cracks on the catalyst layer. As indicated in Figure 2.6(d), the Nafion® dispersion will fill any cracks during the coating process.

In order to increase the uniformity of the coated membranes, a pressing operation was introduced, which significantly decreased the surface roughness of the catalyst layer.

The purchased catalyzed GDLs were pressed between two glass plates under 2 kPa of pressure at room temperature for 180 seconds. Then, using the same coating process mentioned previously, the samples were coated. The morphology of the resulting samples is shown in Figure 2.7(a) – (d). A cross sectional view of an uncoated pressed sample is shown in Figure 2.7(a) and a top view of a coated pressed sample is shown in Figure 2.7(b). Figure 2.7(c) – (d) are cross sectional SEM images of the coated catalyzed GDL. From these pictures, it can be seen that the thickness of the coated catalyzed GDL surface is more uniform than those without pressing.

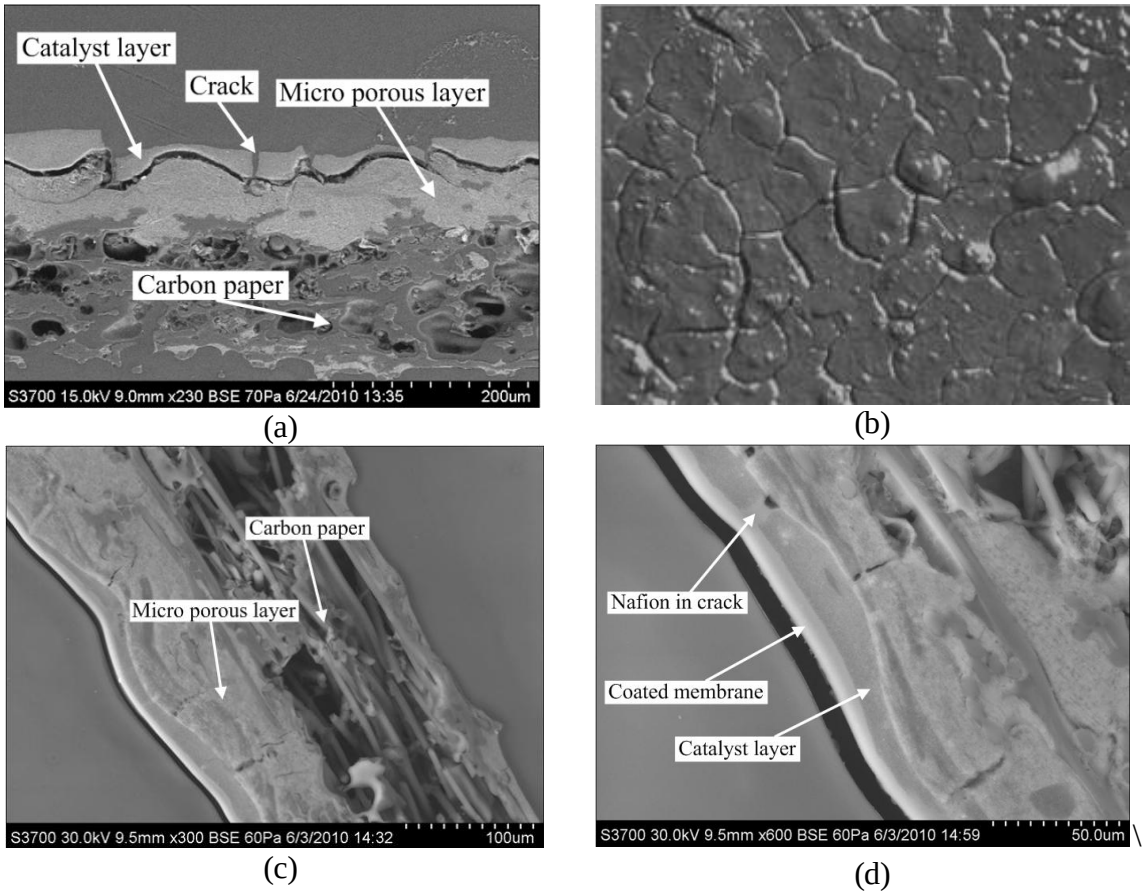

Figure 2.6 (a) SEM image of an uncoated catalyzed GDL, (b) microscopic image of the surface of the coated GDL, and cross sectional SEM images of the coated GDL at (c) x300 magnification and (d) x600 magnification. [50]

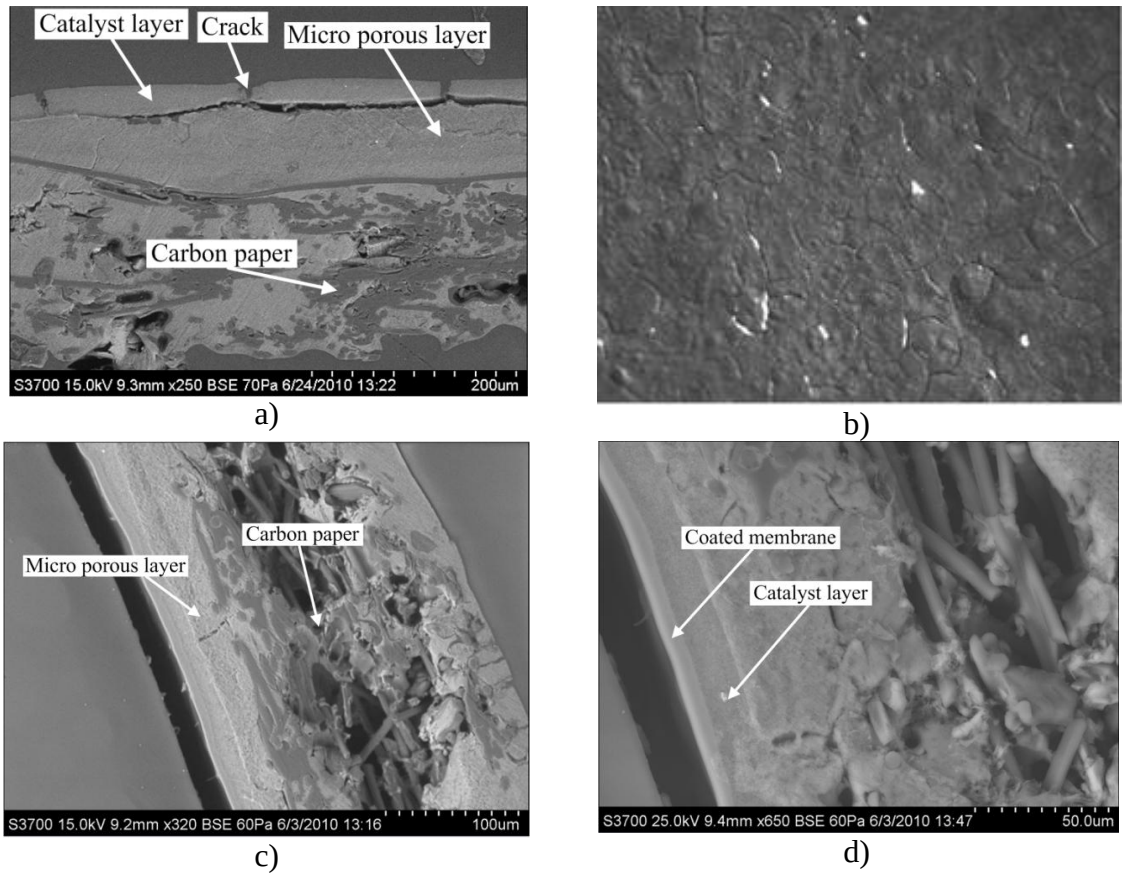

Figure 2.7 (a) SEM image of an uncoated catalyzed GDL that has been pressed, (b) microscopic image of the surface of the coated GDL, and cross sectional SEM images of the coated GDL at (c) x320 magnification and (d) x650 magnification. [50]

The above experimental results show that the uniformity of coated membrane depends on the surface quality of the catalyzed GDL. Hence, the fabrication of the catalyst layer must be controlled to obtain a flat and crack-free surface; otherwise, an alternative processing step will be required such as a pressing operation, to improve the membrane uniformity.

2.6 Penetration of coated membrane

EDX tests were conducted on the plain catalyzed GDLs without coating and the coated catalyzed GDLs to compare the percentage of fluorine in the catalyst layer. More than 10 measured points along the mid-plane of the catalyst layer of each GDL sample

were selected. Figure 2.8 depicts an example of the measured points and the EDX result in the uncoated catalyst layer. It was found that the average fluorine percentage in uncoated catalyst layer was approximately 8.9 w%, whereas the percentage in the coated catalyst layer was approximately 20.2 w%.

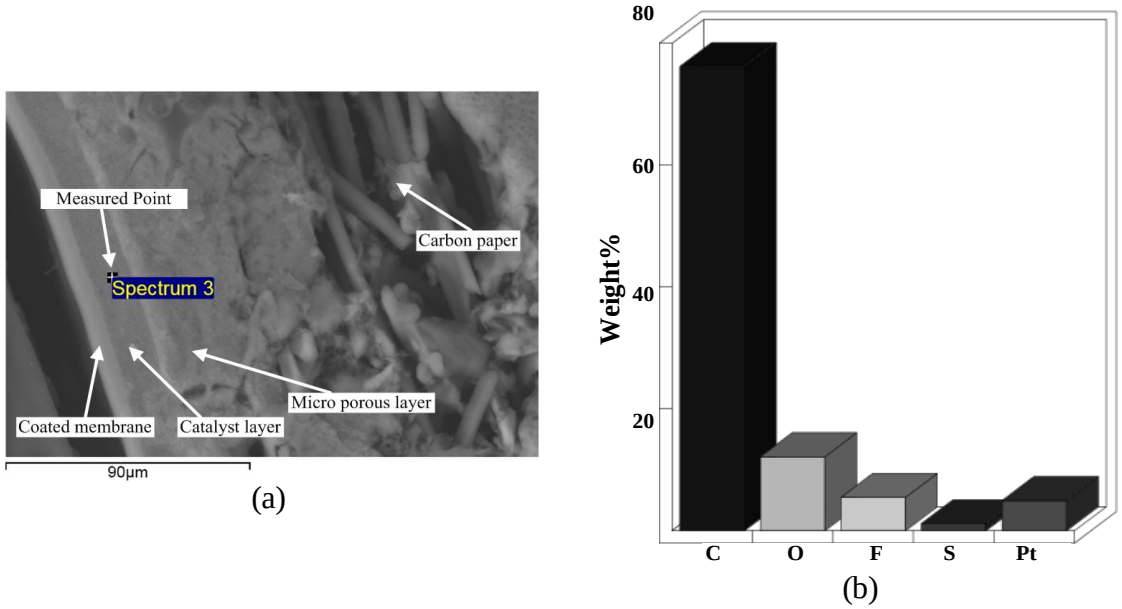

Figure 2.8 (a) A measured point in the center of the catalyst layer, (b) EDX result in uncoated catalyst layer. [50]

Penetration of Nafion® into the catalyst layer is a significant problem, based on the EDX results. In order to decrease the penetration of the ionomer, rapid evaporation of the alcohol based solvents from the dispersion is essential. A set of experiments was conducted to study the feasibility of decreasing the penetration of Nafion® through the GDL with the use of forced convective air flow. Other techniques that can be used include increasing the substrate temperature and concentrating the Nafion® dispersion. Immediately after coating the catalyzed GDL films under the same conditions, air was blown over the samples for 10 minutes. Then, the samples were left in the room environment for 10 hours.

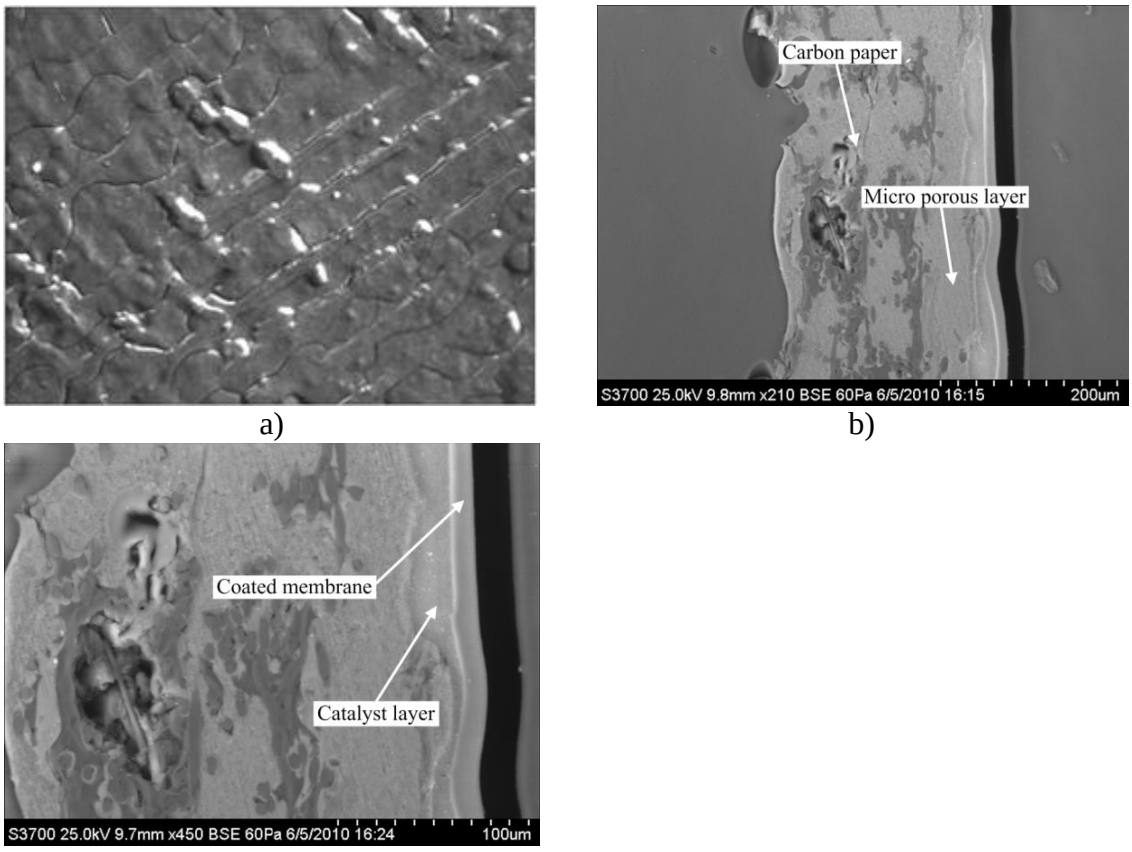

a) b) c)

Figure 2.9 (a) Microscopic image of the air blown surface of a coated unpressed GDL and cross sectional SEM images at (b) x210 magnification and (c) x450 magnification. [50]

Comparing the microscopic images shown in Figure 2.6(b) and Figure 2.9(a), it is seen that the membranes where air was blown over the sample had a smoother surface, and it appears that the quality of Nafion® is better. It should be noted that the surface quality of the coated film also depends upon the surface quality of the catalyzed GDL as mentioned above. Furthermore, comparing the SEM images of Figure 2.6(d) and Figure 2.9(c), it is shown that the membrane thickness of the sample without the use of forced convection air flow was about 5 µm, whereas the sample that was blown with air was 10 µm thick indicating a reduced penetration.

For further validation, EDX measurements were also taken on the air blown samples. As shown in Figure 2.10, the percentage of fluorine in the catalyst layer for the air blown samples is 15.7 w%, which is lower than 20.2 w% in samples without blowing, which means the penetration has decreased.

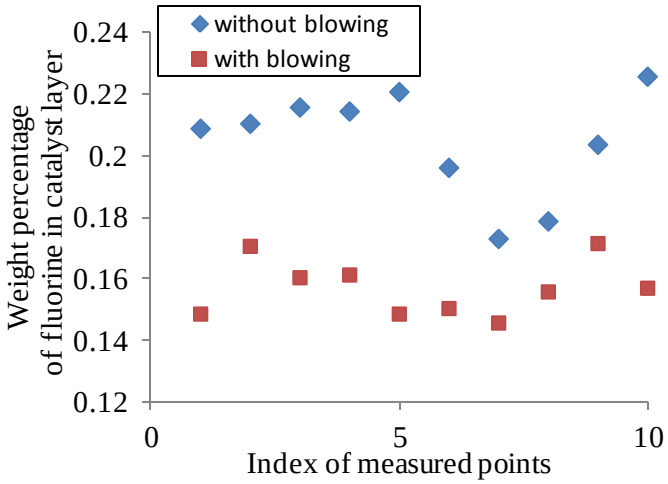

Figure 2.10 Fluorine percentage on some measured points in catalyst layer. [50]

Although some penetration still exists, these preliminary results demonstrate the feasibility to effectively decreasing the penetration of Nafion® by accelerating the solvent evaporation. More experiments could be done on the effects of increasing substrate temperature and concentrating the Nafion® dispersion. In addition, the existence of the MPL may affect the penetration, which will be discussed more in Chapter 4.

2.7 Conclusions

A new fabrication technique to make an MEA using extrusion slot coating to directly coat membrane solution onto catalyzed GDL was presented. This method does not require a separate fabrication process for membrane fabrication before assembly, thus reducing the fabrication steps to produce an MEA compared to conventional methods.

Preliminary coating tests show that the Nafion® dispersion can be directly coated onto the catalyzed GDL forming a membrane on top of the catalyst layer. However, the coated membranes were non-uniform because of the surface roughness and cracks of the catalyst layer. Consequently, the Nafion® would penetrate into the catalyst layer during the coating. In order to decrease the impact of such defects on the quality of the coated membrane, pressing operation and rapid evaporation technique were introduced as pre-processing and post-processing operations, respectively. Results show that pressing the catalyzed GDLs can modify the uniformity of the coated membrane significantly, but more work still has to be done to optimize the pressing parameters. Using the evaporation technique the penetration of Nafion® into the catalyst was decreased by 40%, demonstrating the feasibility to address the penetration problem by accelerating the solvent evaporation.

CHAPTER 3. EFFECTS OF ANNEALING CONDITION ON THE PERFORMANCE OF NAFION® MEMBRANES

3.1 Introduction

In Chapter 2, a new MEA fabrication process based on directly coating membrane solution onto catalyzed GDL was presented, and the feasibility of this method has been studied by examining the membrane uniformity and membrane penetration into the catalyzed GDL. After the direct coating process, the coated Nafion membrane must be annealed to get enhanced mechanical properties and performance. This is the second step of the MEA fabrication procedure proposed in Chapter 2. The annealing time can directly affect the speed and cost of mass producing PEM fuel cells. In order to decrease the annealing time, it is necessary to understand the effects of annealing condition on the performance of fuel cells, as discussed in Chapter 3, which is based on published work by Ding et al. [52]

A traditional approach to fabricate Nafion® membrane is casting from polymer solution [67-69]. However, the solvent plays a vital role in the quality of the membrane. Solution cast Nafion® membranes from aliphatic alcohol/water mixtures at room temperature have poor mechanical properties and dissolves in a variety of polar solvents, especially in water [70, 71]. To enhance the properties of the cast membranes, two solvent-based evaporation approaches have been developed.

In the first approach, high boiling point solvents (e.g., dimethylformamide) are used to make the Nafion® solution. The solution is heated to a temperature above the glass-transition temperature, T_g, of Nafion® during drying resulting in a high-quality membrane [68-71]. The improvement in mechanical properties by thermal treatment is

believed to be related to an inverted micelle structure caused by high temperature, which also increases the crystallinity of the polymer [72, 73]. A second, simpler method of fabricating the membrane is to directly evaporate the solvents (e.g., aliphatic alcohol/water mixtures) from solution at room temperature or slightly higher, and then anneal the membrane at a temperature above its T_g. However, no standard approach has been reported for the annealing process. The annealing temperature discussed in the literature varies from 120 ℃ to 165 ℃, and the annealing time varies from 30 min to 12 hours [72-75]. In these studies, the temperature and time in the annealing process are controlled; however, the effects of humidity during annealing on the membrane performance or properties were not taken into account. Werner et al. [76] mentioned annealing cast Nafion® membranes at 100 % relative humidity, but very limited information was provided.

Many authors have investigated the physical, chemical, and mechanical properties of annealed cast membranes [69-71, 73-75], but few have studied the impact that annealing has on performance of the cast membranes in fuel cells. Vengatesan et al. [72] compared the fuel-cell performance of solution cast membranes made from different annealing conditions with commercial membrane. However, the annealing time was in excess of 3 hours, and the performance results were limited to high cell potentials (above 0.6 volts), which neglected the performance at high current densities where mass-transfer effects are important.

In this Chapter, the effects of annealing time and humidity on the performance of solution cast Nafion® membranes are investigated experimentally. An annealing temperature of 120 ℃ was chosen to make 50 μm thick cast membranes which were

annealed from 10 to 60 min in a dry or humid oven, to obtain the finished membranes. Then a catalyst layer was applied to both sides of annealed membranes to make MEAs. X-ray diffraction (XRD) patterns, cell performance, membrane resistance, H_2 crossover current, and ultimate tensile strength were measured to analyze and compare the performance and characteristics of different membranes, including a commercial Nafion® membrane.

3.2 Experimental procedure

3.2.1 Preparation of solution cast membranes

Nafion® D2021 with 20-22 wt% polymer content was used to make the solution cast membranes. The solvent was a mixture of water, 1-propanol, ethanol, an unspecified mix of ethers and other volatile organic compounds. 5.5 g of solution was allowed to dry on the bottom surface of an in-house made cubic glass container, which is 4 x 4 x 1 in, for 16 hrs. The glass container was kept horizontally to ensure that the membranes had uniform thickness. It was found that the membranes would crack during the drying process if the ambient temperature was too low or if the air flow above the solution was too turbulent. In order to avoid cracking, the glass container was put on a 30 ℃ hot plate and covered with a permeable tissue paper, which can isolate outside air flow while allowing the solvents to evaporate. Then the cast membranes were annealed in an oven at 120 ℃ to enhance their mechanical properties. Two conditions (dry and wet) were created in the oven to study the effects of moisture during annealing. In the dry condition, desiccants made of anhydrous calcium sulfate were kept in the oven to absorb any excess moisture. The relative humidity was believed to be close to zero. In the wet situation, a beaker containing 1000 ml of water was kept in the oven to generate a wet environment.

The temperature of water was measured to be around 90 ℃ during the tests. The relative humidity in the wet oven could be approximated by the ratio of saturated vapor pressure at 90 ℃ and 120 ℃, which results in 35% RH.

The cast membranes were annealed for 10, 30 and 60 min under wet or dry conditions and were classified based on the annealing time and condition, e.g., Wet-10, Dry-10, etc., as listed in Table 3-1. The annealed membranes either disengaged from the glass container or were easily removed with tweezers after immersion in de-ionized water for about 10 to 20 min. In order to measure the dry thickness, all samples were dried at 60 ℃ for 3 hours and the dry thicknesses were measured immediately, using a Mitutoyo digital thickness gauge. The dry thicknesses of all samples were 50±5 μm.

Table 3-1 Annealing conditions of initial casting membranes (120 ℃). [52]

Membrane	Annealing humidity	Annealing time (min)
Wet-10	Humid	10
Wet-30	Humid	30
Wet-60	Humid	60
Dry-10	Dry	10
Dry-30	Dry	30
Dry-60	Dry	60

In previous studies, it was found that cast Nafion® membranes often have a light yellow color after annealing [68, 73]. In this study, it was observed that membranes, annealed under the humid conditions discussed were transparent, similar to those purchased commercially; whereas, those annealed in dry conditions were light or dark yellow color. The intensity of the color seems to be dependent upon the annealing and drying time. The membrane appeared darker when longer annealing times or shorter

drying times were tested. Furthermore, the yellowish color may be attributed to residual solvents or impurities in the membrane. However, it should be noted that the membrane color, which gradually faded during preconditioning of the fuel cell, did not have an effect on the performance. As an added precaution, the color can be eliminated by boiling the membranes in 3% hydrogen peroxide solution.

3.2.2 Preparation of MEAs

MEAs were made by spraying catalyst ink onto the cast and commercial membrane with a manual airbrush, purchased from Paasche. A platinum loading of 0.31 mg/cm^2 with a standard deviation of 0.063 mg/cm^2 was sprayed on the anode and cathode sides. The desired catalyst loading was controlled by continuously weighing each sample during the coating process. Catalyst ink was prepared with 46.7 wt% Pt/C, Nafion® D2021, isopropyl alcohol and de-ionized water. The weight ratio among Pt/C powder, Nafion® D2021, isopropyl alcohol and de-ionized water is 1 : 2.19 : 7.66 : 4.19. The Nafion® content in the final catalyst layer is 30 wt%. The catalyst ink was blended with an ultrasonic mixer for 30 min before spraying a 5 x 5 cm catalyst area on an 8 x 8 cm membrane. Toray 060 carbon paper was chosen as GDL. The catalyzed membranes were placed between two 5 x 5 cm GDLs without hot pressing, then assembled with gaskets and bipolar plates in a test cell.

3.2.3 Preconditioning and tests of new MEAs

To obtain the performance characteristics, I-V characteristics, AC impedance spectroscopy, linear sweep voltammetry, cyclic voltammetry were measured. Before these tests, all new MEA samples were preconditioned based on DuPont's MEA Preconditioning and Qualification Protocol [77]. Specifically, stoichiometry ratios were set

to 2.0 and back pressures were set to 170 kPa for both anode side (hydrogen) and cathode side (air), temperatures were fixed at 85 ℃ for the anode inlet, cathode inlet and cell, which are denoted as 85/85/85 ℃ (anode/cathode/cell). The cell was run at 0.2 V for 10 min, then it was switched to 1 V for 30 s. This cycle was repeated 80 times for the whole preconditioning process.

The membrane samples were characterized using XRD. The membrane samples were coated onto silicon wafers and cured under various conditions, as described above. XRD patterns were measured using X'Pert PRO diffractometer, (PANalytical) at scanning speeds of 0.02 °/sec and an accelerating voltage of 45 kV.

Performance of the cell was evaluated by measuring I-V characteristics and power density using a Scribner 850E fuel-cell test station. The dry-gas flow rates were fixed at 0.3 and 2 L/min for anode side (hydrogen) and cathode side (air), respectively. The fuel cell hardware, which is a single cell unit, was bought from Scribner Associates Inc. The flow field of the bipolar plate is triple serpentine, with dimensions of 5 x 5 cm. The temperatures were set to 75/75/80 ℃ (anode/cathode/cell). No back pressure was used.

Membrane resistance was determined with AC impedance spectroscopy using an Autolab potentiostat and NOVA software. The spectra were recorded between 50 mHz and 10 kHz with a current amplitude of 0.025 A. When conducting the resistance tests, flow rates were fixed at 1 and 2 L/min for anode (hydrogen) and cathode (air), respectively. Before starting the test, hydrogen and air flowed through the cell for about 20 min to fully humidify the membranes. The temperatures were set to 80/80/80 ℃ (anode/cathode/cell).

H_2 crossover current was obtained by linear sweep voltammetry, and the electrochemical active area (ECA) was measured by cyclic voltammetry. For these two tests, flow rates were fixed at 0.2 L/min for both anode (hydrogen) and cathode (nitrogen), temperatures were set to 35/35/35 ℃ (anode/cathode/cell), and the scan rates were set to 2 and 20 mV s-1, for the respective tests.

3.3 Experimental results and discussion

A summary of the results from the tests and measurements conducted on the samples is provided in Table 3-2. Detailed analysis can be found in the subsequent sections.

3.3.1 Crystallinity versus annealing condition

The microstructure of Nafion® is known to be semicrystalline [78]. A diffraction angle of 18° with a sharp peak is characteristic for Nafion® membrane [79]. XRD patterns for the samples annealed under dry and wet conditions, as well as an un-annealed sample, are shown in Figure 3.1. Membranes annealed under dry conditions followed characteristics expected of Nafion®, although the sharp peak at the diffraction angle was slightly shifted, 17.68° (Dry-10), 17.77° (Dry-30), and 17.78° (Dry-60). As annealing time increases under dry conditions, the XRD pattern of the membrane aligns more with the expected crystalline behavior of Nafion®. From the data in Figure 3.1, the crystallinity of samples annealed under dry conditions is calculated to be 12% (Dry-10), 16.5% (Dry-30) and 17% (Dry-60). It can be seen that the crystallinity does not change much after 30 min. Furthermore, it is evident that the patterns for the un-annealed Nafion® membrane is wider and shifts to a lower diffraction angle of 17.36°, illustrating

Table 3-2 Summarization of the XRD test, performance test, AC impedance spectroscopy test, cyclic voltammetry test, sweep voltammetry tests and tensile strength test.* [52]

	XRD	**I-V characteristics**			**Impedance spectroscopy**	**Cyclic voltammetry**	**Sweep voltammetry**	**Tensile strength**
Samples	Diffraction angle (°)	Open circuit voltage (V)	Voltage at 1000 mA/cm^2 (V)	Voltage at 1500 mA/cm^2 (V)	R_{hf} at 80/80/80 ℃ (Ohm cm^2)	ECA (m^2/g)	Crossover current at 0.4 V (mA/cm^2)	(Mpa)
NR-212	-	0.999±0.028	0.598±0.002	0.447±0.019	0.076	54.0	0.50	24.9±1.0
Wet-60	17.35	0.987±0.001	0.602±0.011	0.465±0.001	0.078	56.0	0.69	-
Wet-30	17.11	0.984±0.003	0.601±0.002	0.457±0.017	0.078	49.7	0.54	-
Wet-10	17.54	1.003±0.010	0.572±0.017	0.363±0.057	0.087	50.1	0.50	-
Dry-60	17.78	1.01	0.617	0.471	0.078	51.7	0.73	23.6±1.3
Dry-30	17.77	1.015±0.007	0.609±0.011	0.452±0.028	0.076	55.9	0.52	23.2±1.9
Dry-10	17.68	1.02	0.616	0.441	0.075	49.7	0.56	16.9±0.8
Dry-5	-	-	-	-	-	-	-	13.0±0.3
Non-annealed	17.36	-	-	-	-	-	-	-

* : Multiple samples have been made and tested for the performance and tensile strength for each annealing condition. Specifically, for I-V characteristics, values of NR 212 are averaged from 4 samples; values of Wet-60, Wet-30, Wet-10 and Dry-30 are averaged from 2 samples; values of Dry-60 and Dry-10 only obtained from 1 sample. For tensile strength, values of NR 212, Dry-60, Dry-30 and Dry-10 are averaged from 3 samples; value of Dry-5 is averaged from 2 samples. For XRD, impedance spectroscopy, cyclic and sweep voltammetry, only one sample for each annealing condition is reported.

that if the membrane is not annealed, the degree of crystallinity is significantly reduced. Similar patterns were observed for membranes annealed under wet conditions, the patterns are wider and shifted to lower diffraction angles, 17.54° (Wet-10), 17.11° (Wet-30) and 17.35° (Wet-60). The crystallinity of the un-annealed sample and samples annealed under wet conditions is calculated to be zero.

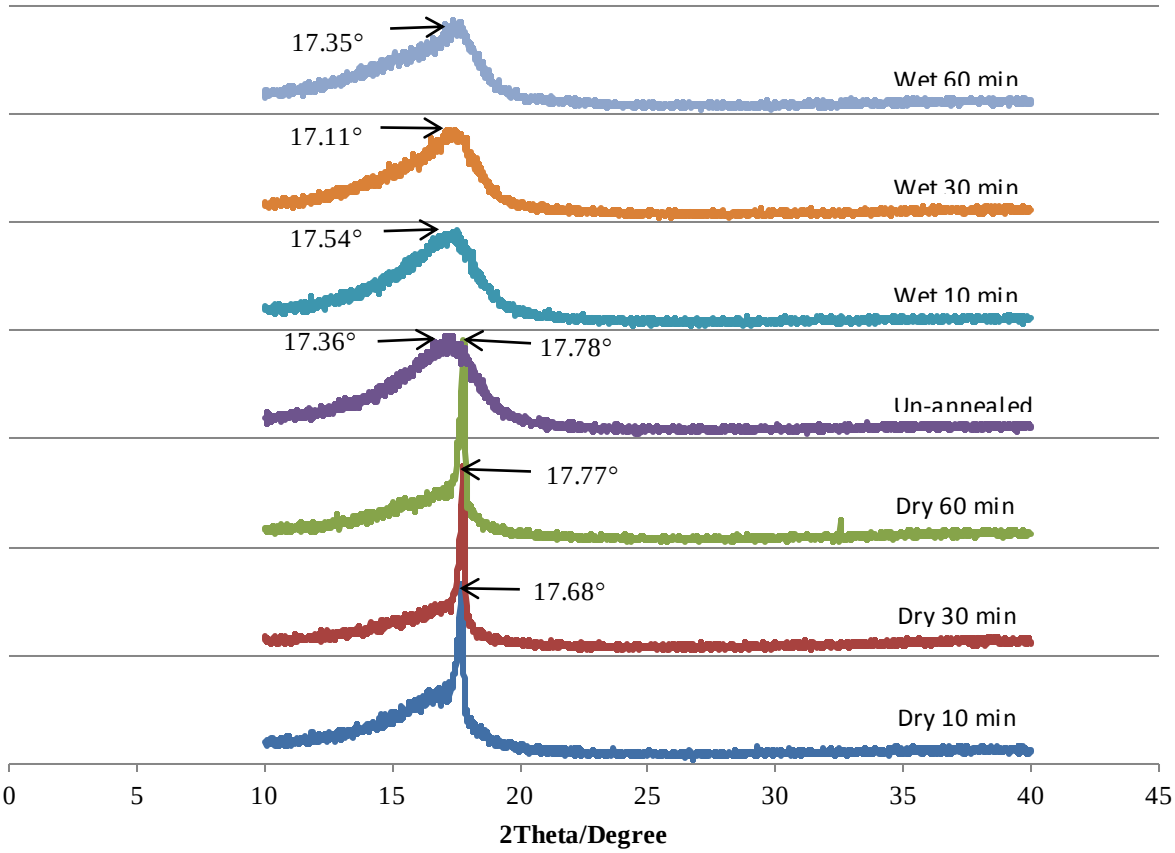

Figure 3.1 XRD patterns of the membrane samples under various annealing conditions.

3.3.2 Performance versus annealing condition

The effects of annealing solution cast Nafion® membranes in humid and dry conditions on the performance of polymer electrolyte membrane fuel cells are depicted in

Figure 3.2, for typical samples. It can be seen that all solution cast membranes perform similarly to the commercial membrane. However, in the humid annealing condition, the membrane annealed for 10 min (Wet-10) performs slightly worse at voltages below 0.6 V. When the annealing time is longer than 30 min, no obvious performance changes were found; hence, Wet-30 and Wet-60 perform similarly to commercial membrane over the entire voltage range. In the dry annealing condition, all membranes (Dry-10, Dry-30 and Dry-60) perform almost the same as commercial membrane. The slight performance difference between NR-212, Wet-30, Wet-60, Dry-10, Dry-30 and Dry-60 might be caused by the fluctuation of catalyst loading and membrane thickness, or other measurement errors. These results demonstrate that based on initial performance, a significantly lower annealing time (10 min under dry conditions) may be used, with negligible differences in performance to state-of-the-art membranes. This reduction in annealing time would be especially advantageous during mass production of membrane materials.

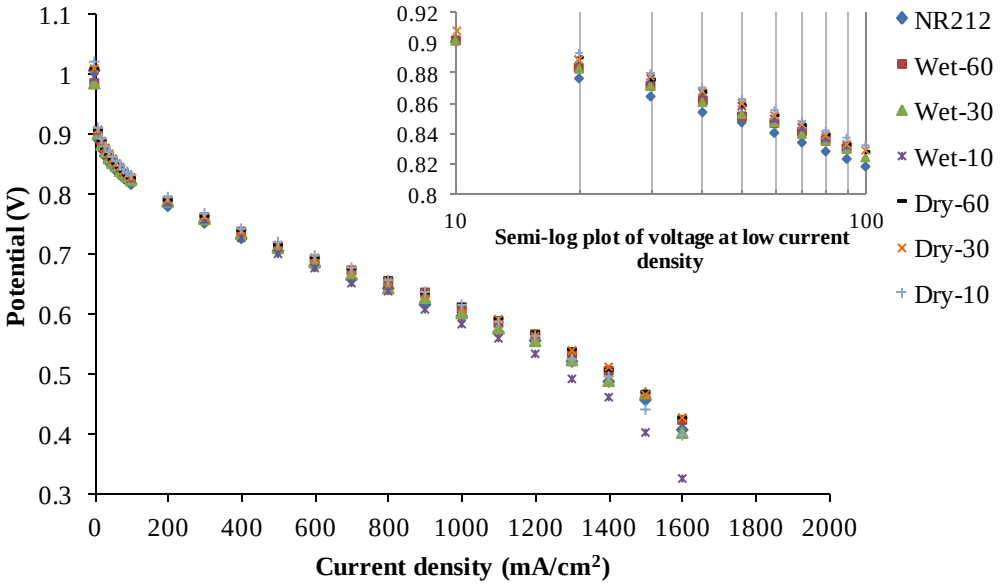

Figure 3.2 Effects of annealing condition on performance of single cells. [52]

3.3.3 Membrane resistance versus annealing condition

In order to analyze the effects of annealing condition on the membrane resistance, which directly determine the cell performance, AC impedance spectroscopy tests were used. Nyquist plots for the single cells fabricated with the solution cast membranes and Nafion® NR-212 at 80/80/80 ℃ (anode/cathode/cell) are shown in Figure 3.3. It can be seen that the result for each MEA is approximately equal. This data suggest that the effective charge-transfer resistance within the catalyst layer and the mass-transport limitations within the gas diffusion media are approximately the same. Thus, the slightly lower performance of Wet-10 observed in Figure 3.2 is not due to either of these factors.

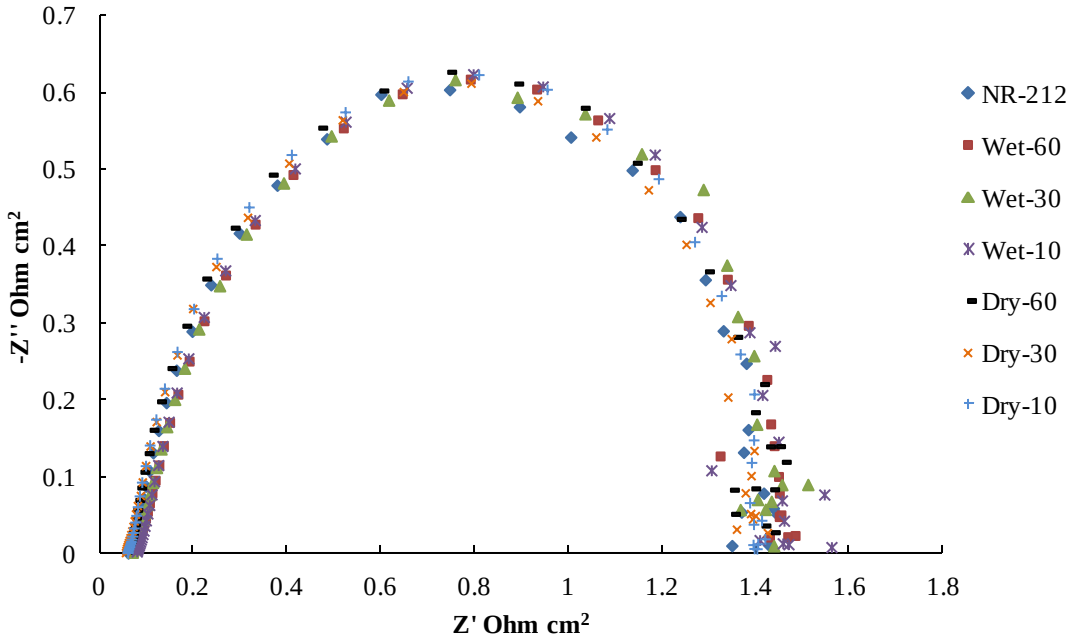

Figure 3.3 Effects of annealing condition on Nyquist plots of the single cells. [52]

Ohmic resistance (R_{hf}) of the cell was obtained. R_{hf} includes membrane resistance (R_m), electronic resistance of all other current-carrying components, such as GDL, bipolar plates and leads (R_{bulk}) and contact resistances ($R_{contact}$). R_{bulk} and $R_{contact}$ were considered constant for all cells. Thus, knowing R_{hf} will allow for directly solving R_m given R_{hf} =

$R_{bulk}+Rc_{contact}+R_m$. R_{hf} for all cells made from solution cast membranes and commercial NR-212 at 80/80/80 ℃ were measured. The results are shown in Table 3-2. When using NR-212 membrane, it was observed that R_{hf} (0.076 Ohm-cm^2) was higher than R_m (0.028 Ohm-cm^2), where R_m was calculated from the ionic conductivity value of 0.95 S/cm reported by Kidena et al. [80] Furthermore, it is shown that all cast membranes will have approximately the same R_{hf} as NR-212 after annealing for 10 min in dry conditions, and that further increasing the annealing time does not significantly change R_{hf}. However, it seems that the membrane annealed for 10 min in humid conditions has 16% higher R_{hf} (0.087 Ohm-cm2) than NR-212. This may be attributed to the inadequate crystallization of the membrane at the lower annealing time for wet conditions, which negatively impacts the ionic conductivity. Resistance test results coincide with previous performance test results well.

3.3.4 Cyclic voltammetry versus annealing condition

ECA was evaluated by cyclic voltammetry to ensure the same catalyst properties of all samples, thus confirming the previous performance and membrane resistance tests results. A typical cyclic voltammogram of the sample NR-212 is shown in Figure 3.4. The difference between the ECA measurements is relatively low, having values of 54.0, 56.0, 49.7, 50.1, 51.7, 55.9, and 49.7 m^2/g, for NR-212, Wet-60, Wet-30, Wet-10, Dry-60, Dry-30 and Dry-10, respectively. Hence, all samples have similar catalyst surface area in contact with the ionomer, which verifies that the lower performance of Wet-10 membrane was not caused by lower catalyst activity.

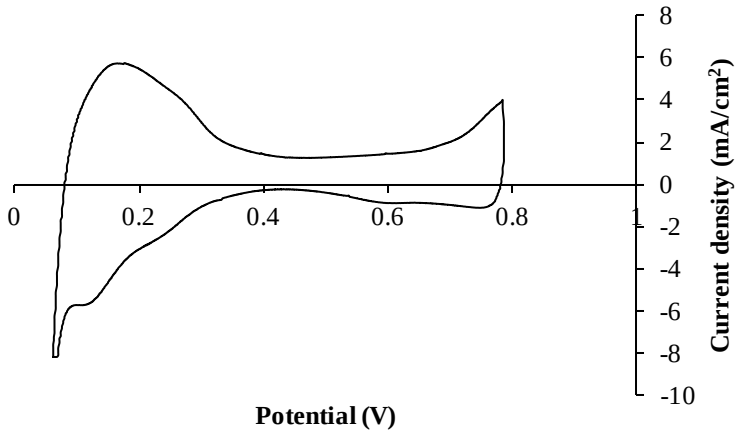

Figure 3.4 Cyclic voltammogram of MEA made from commercial membrane NR-212. [52]

3.3.5 H_2 crossover Current versus Annealing Condition

It was found that the H_2 crossover current of all the solution cast membranes and the commercial membrane were low, between 0.5 to 0.8 mA/cm2, as shown in Figure 3.5 and Table 3-2. It was also found that membranes annealed for 10 and 30 min have similar H_2 crossover current as the commercial membrane. However, slightly higher H_2 crossover currents were observed for the membranes annealed for 60 min, which were around 0.7 to 0.8 mA/cm^2.

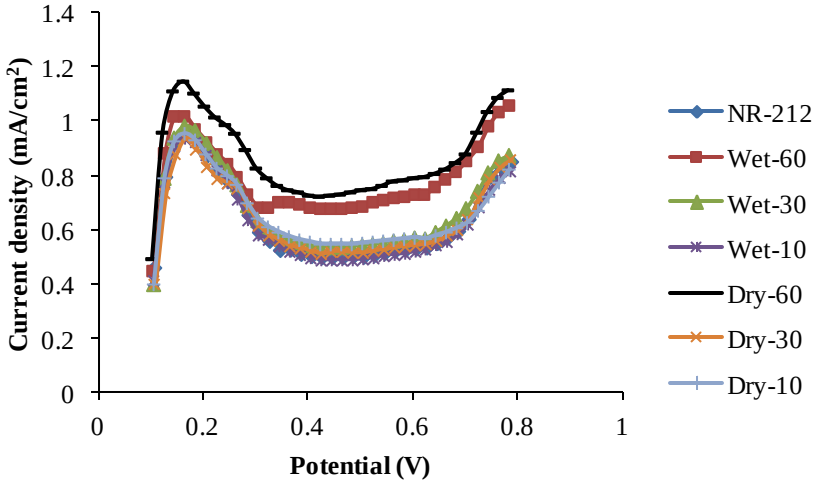

Figure 3.5 Effects of annealing condition on H_2 crossover current of casting membranes. [52]

3.3.6 Tensile strength

From the above performance test results, an annealing time of 10 min in dry conditions was found to be sufficient from a performance standpoint. However, the mechanical strength of the samples in dry conditions is also of interest. Tensile tests were conducted on samples Dry-10, Dry-30, Dry-60 and NR-212. An additional sample, Dry-5, annealed for only 5 min was also tested for comparison. It was found that the tensile strength of different samples were 13.0 MPa (Dry-5), 16.9 MPa (Dry-10), 23.2 MPa (Dry-30), 23.6 MPa (Dry-60) and 24.9 MPa (NR-212). Thus, it is concluded that the tensile strength increases with annealing time from 5 to 30 min. Yet after 30 min, there is no significant change in tensile strength. Further, it was found that for samples annealed longer than 30 min the tensile strength is approximately the same as that of NR-212 measured in-house and reported previously [67]. Although, the tensile strength of Dry-10 is about 32% lower than NR-212, this lower strength alone does not preclude the use of a 10 min annealing time.

3.4 Conclusions

Effects of annealing condition on the performance of solution cast Nafion® membranes were studied experimentally. It has been found that solution cast membranes annealed under both dry and humid conditions, for 10 - 60 min, will have similar performance as commercial membranes in fuel cells. However, it was observed that membranes annealed for 10 min in the humid oven (i.e., Wet-10) performs slightly worse at voltages below 0.6 V. The annealing time and humidity probably impacts the final resistance, and thus, the performance of cast membranes. XRD tests showed that a dry annealing condition is necessary to ensure similar crystallinity for cast membranes and

commercial membranes. Tensile tests showed that cast membranes annealed for 30 and 60 min in dry annealing condition have similar tensile strength to the commercial membrane; while the tensile strength of the membrane annealed for 10 min is about 32% lower than commercial membrane. However, this difference is expected to decrease if a higher annealing temperature can be used. The significant result from this work is that a much lower annealing time (10 min) is sufficient for making cast membranes with similar performance as commercial membranes in fuel cells, which is advantageous for scale-up mass production processing

CHAPTER 4. CHARACTERISTICS AND PERFORMANCE OF MEAS FABRICATED USING DIRECT COATING CATALYZED GDLS

4.1 Introduction

In Chapter 2, a detailed MEA fabrication procedure based on slot die coating onto catalyzed GDLs was discussed. There are four basic steps of this new procedure: coating, annealing, assembling and sealing. In Chapter 2, the feasibility of the membrane coating step was experimentally examined and analyzed. In Chapter 3, the conditions for the annealing step were experimentally studied. In this chapter, the last two steps will be discussed and the characteristics and performance of MEA samples fabricated by this new technique will be tested to compare with two MEAs made using traditional methods.

4.2 MEAs fabrication

4.2.1 Coating on catalyzed GDL without MPL

The surface quality of the catalyst layer directly affects the uniformity of coated membrane. Thus, an in-house made catalyzed GDL with flat and crack-free catalyst layer surface was used for tests to ensure the highest quality surface. These catalyzed GDLs were made by uniformly spraying catalyst ink onto carbon paper using an air brush. The platinum loading was 0.3 mg/cm^2 with a standard deviation of 0.063 mg/cm^2. An MPL was not applied this time so that the effect of MPL on penetration could be investigated by comparing with the results in Chapter 2.

A 4x4 cm^2 Toray 060 carbon paper with a 3x3 cm^2 catalyst layer on the center top was directly coated with the membrane solution. In order to realize mass production, it is

expected that the membrane will be directly coated onto a moving substrate, such as a catalyzed gas diffusion layer, with the proper thickness in one pass at mass production rates (e.g., 100 cm/s – 1 m/s). However, in this study the feasibility of the new MEA fabrication method is presented for solution being coated onto a moving catalyzed GDL at relatively low speeds, in order to control the coating process. Specifically, each sample was coated five times with a coating speed of 0.5 cm/s to achieve the desired thickness of membrane. Air was forced or blown across the surface to decrease the penetration of ionomer. It was found that the membrane tended to crack under turbulent air flow for larger samples, e.g., 4x4 cm^2. It was also found that higher environmental temperatures help prevent cracking. Thus, after each coating, the sample was dried under blown air for 5 min and then moved to a 60 ℃ oven for 30 min.

The increase in thickness and dry weight of the catalyzed GDL were measured after each coating. The thickness at 16 fixed positions was measured and averaged. The dry weight was measured after drying in the oven. Several samples were made; the results of a typical sample are shown in Figure 4.1. Due to the fixed flow rate and speed of coating, the increase in dry weight after each coating is constant, 0.042 g. With reference to the dry density, 2.132 g/cm^3 (measured from casting membrane on glass), of Nafion® membrane the volume of a 0.042 g membrane should be 0.0197 cm^3. Thus, for a 4x4 cm^2 area, the thickness will be 12.3 μm, which is the theoretical dry thickness increase after each coating. However, it is evident from Figure 4.1, that the membrane thickness only slightly increases, about 4 μm, after the 1^{st} and 2^{nd} coatings. It is apparently much thinner than the theoretical value, which means initially most of the solution penetrates into catalyzed GDL. This was distinctly different with what was observed in previous coating

tests using purchased catalyzed GDL with an MPL, where the coated membrane was around 10 μm after the 1st coating under an even higher coating speed, 0.6 cm/s, which theoretically should cause thinner membrane. This means that the MPL prevents penetration of Nafion® effectively, since the membrane was thicker.

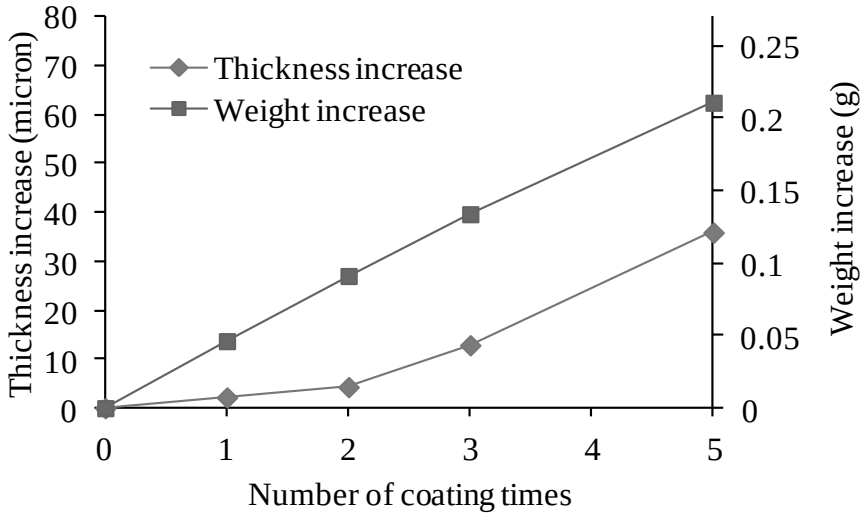

Figure 4.1 Thickness and weight increase of the coated catalyzed GDL with number of coating times. [50]

After the 3rd coating it can be seen from Figure 4.1 that the dry thickness of the coated membrane increased by 9 μm, which means that the penetration reduced. It is believed that this increase in thickness change is due to the decreased porosity from the 1st and 2nd coatings. In addition, the total increase of membrane thickness for the 4th and 5th coating was about 23 μm, which means there was almost no penetration of Nafion® in these two coatings. Finally, the entire weight increase was about 0.21 g, which should theoretically form a 62 μm thick film on a 4x4 cm^2 area. However, the actual increase in total thickness on top of the catalyst layer was only 36 μm due to the penetration, as discussed above.

4.2.2 Samples annealing, assembling and sealing

After drying, the obtained coated samples were annealed in a 120℃ oven for 10 min. The effectiveness of this annealing condition has been examined in Chapter 3. Then, as shown in Figure 4.2, a 3x3 cm^2 catalyst layer was directly sprayed on top of the coated membrane, and another 3x3 cm^2 GDL was put on top of the sprayed catalyst layer without hot pressing to form the MEA. MEAs made from *directly* coated catalyzed GDL will be called D-MEA from hence forth. In addition, the top *sprayed* catalyst layer will be referred to as the sprayed side, while the bottom catalyst layer (where the membrane was coated) will be referred to as the coated side.

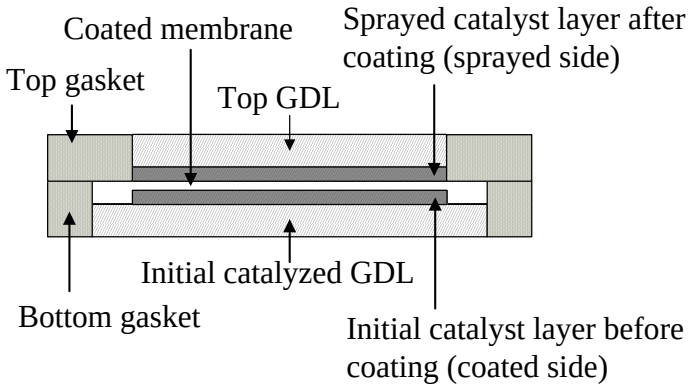

Figure 4.2 Structure and sealing of MEA fabricated from directly coated catalyzed GDL. [50]

The whole D-MEA was sealed by two layers of gasket material (top gasket and bottom gasket in Figure 4.2). The overlap between the top gasket and peripheral area of the coated membrane was used to prevent leakage and crossover. This MEA fabrication and sealing method was selected because it is well suited for small quantity laboratory scale fabrication. The complete process discussed in Chapter 2, which includes hot pressing and sealant material injection operations, is well-suited for large scale production and was not applied in this preliminary demonstration.

4.2.3 MEAs fabricated by a traditional method

In order to facilitate performance comparison, two MEAs were fabricated using the traditional approach. One was made of commercial NR-212. The other one was made of in-house cast membrane that had the same dry thickness with the NR-212, 50 μm. It was annealed under the same conditions as the above D-MEAs (120 ℃ for 10 min). Both traditional MEAs were made by spraying catalyst ink directly on membrane. Then they were joined with two GDLs without hot pressing. All MEAs, including D-MEAs and traditional MEAs, were made from the same catalyst ink and had the same platinum loading on both sides of the membrane, 0.3 mg/cm^2.

4.3 Performance test

The performance of the MEAs was evaluated by measuring I-V characteristics with a Scribner 850E fuel-cell test station. For more indepth analysis, AC impedance spectroscopy, cyclic voltammetry, and sweep voltammetry tests were also conducted. The D-MEAs were tested in two orientations, (1) with the sprayed side as the cathode and (2) with the coated side as the cathode. Performance results, Nyquist plots and cyclic voltammograms, are shown in Figure 4.3 to Figure 4.5, respectively. Important results are summarized in Table 4-1 for comparison.

From Figure 4.3, it can be seen that the two traditional MEAs performed about the same. When the sprayed side was used as the cathode, the overall performance of D-MEA was closer to that of the traditional MEAs. However D-MEA's performance was much lower when the coated side was used as the cathode. From Figure 4.4, membrane resistances were approximated by the high frequency intercepts with the real axis on the Nyquist plot. It was found that the resistance was 0.061, 0.057, 0.068 and 0.062 Ohm cm^2

for NR -212, membrane cast on glass, D-MEA (sprayed side as cathode) and D-MEA (coated side as cathode) respectively, as shown in Table 4-1. Considering unavoidable measurement errors, these differences are considered small and should not be the reason for performance differences. However, as shown in Figure 4.4, traditional MEAs have an apparently smaller high frequency arc radius than D-MEA. Especially when the coated side was used as the cathode, the D-MEA has the largest high frequency arc radius, which indicates a severe oxygen transport limitation exists. In order to find the reason of the oxygen transport limitation, the performance test was also conducted using heliox (mixture of 21% oxygen and 79% helium) instead of air in the cathode. As shown in Figure 4.3, when the coated side was used as the cathode, the D-MEA performed better with heliox, but it was still much lower than other cases. These results suggest that the oxygen transport limitation was in both the gas and liquid phases, here the liquid phase consists of the electrolyte Nafion and water. It is suspected that excessive Nafion® and lower porosity were present in the coated side. Therefore, the primary cause of the poor performance was the penetration of Nafion® into the catalyst layer and GDL during coating.

The effect of Nafion® penetration could also be demonstrated by comparing the ECA of different cases. For traditional MEAs made from NR-212 and membrane cast on glass, and the D-MEA when the sprayed side was used as the cathode, the ECAs were very close, measured as 49.8, 48.5 and 48.5 m^2/g, respectively (Table 4-1). Whereas when the coated side was used as the cathode, much higher ECA, 84.4 m^2/g, was found for the D-MEA. Since all initial catalyst layers were made from the same material and procedure, their initial ECAs should be the same. Thus, the higher ECA value of the

coated side must be caused by the coating process. Specifically, it indicates higher Nafion® content caused by penetration during the coating. From the linear voltammetry tests, it is found that the crossover currents of the traditional MEAs and the D-MEA are low and the difference between the values is 0.2 ± 0.03 mA/cm^2. This small difference should not result in a significant change in performance.

Based on above analysis, the poor performance of the D-MEA could be explained in the following way. Due to the sluggish kinetics of the oxygen reduction reaction, the electrochemical activity in the cathode side will dominate the overall performance of the fuel cell. When the coated side was used as the cathode, the performance was much worse due to the higher charge transfer resistance and correspondingly lower electrochemical activity. This is because of the penetration of Nafion® in this side, which decreases the porosity and also alters the balance of ionic conductivity and electronic conductivity. When the sprayed side was used as the cathode, the performance was much closer to that of traditional MEAs. However, due to the lower electrochemical activity in the coated side, the overall performance was still lower than traditional MEAs.

To increase the performance of the cell, modifications to the coated side of the MEA are required. For instance, membrane solution penetration into the catalyzed GDL has to be decreased. Incorporating an MPL into the MEA and accelerating the evaporation of solvents by forced convection are plausible methods of decreasing the penetration of the solution. Furthermore, the initial weight ratio of Nafion® in the catalyst layer can be decreased to balance the increase of Nafion® due to the inherent penetration.

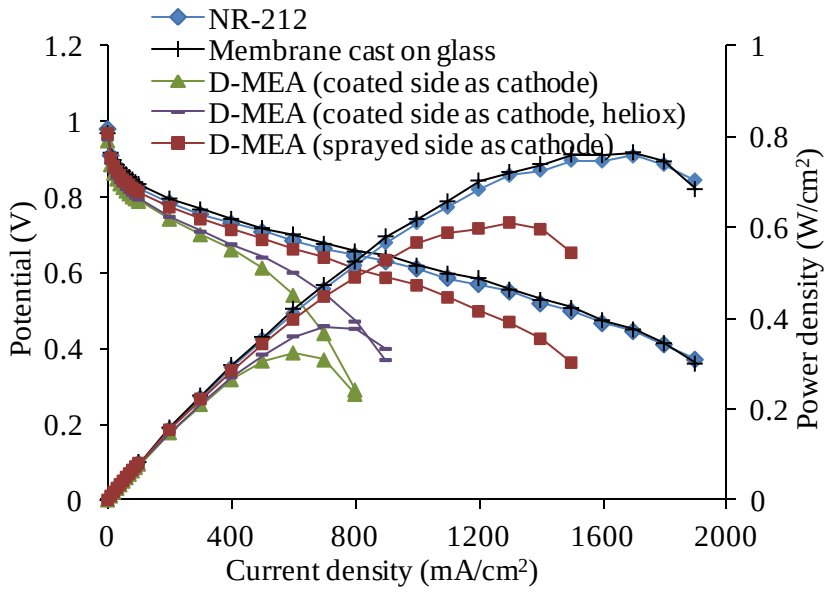

Figure 4.3 Comparison of D-MEA and traditional MEAs. Flow rate = 0.3 L/min for anode (H_2) and = 2 L/min for cathode (air). Temperature = 75/75/80 ℃ (anode humidifier/cathode humidifier/cell). [50]

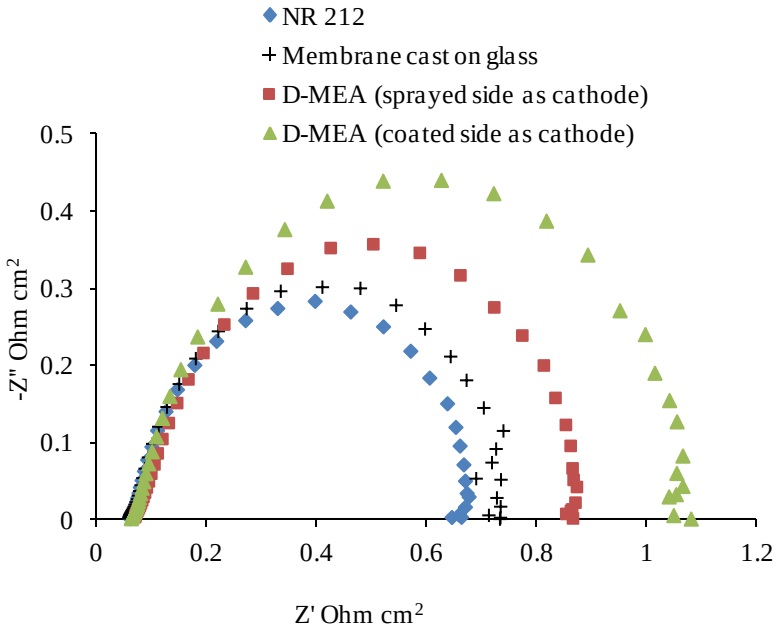

Figure 4.4 Nyquist plots of single cells. Flow rate = 1 L/min for the anode (H_2) and 2 L/min for cathode (O_2). Temperature =80/80/80 ℃ (anode humidifier/cathode humidifier/cell). [50]

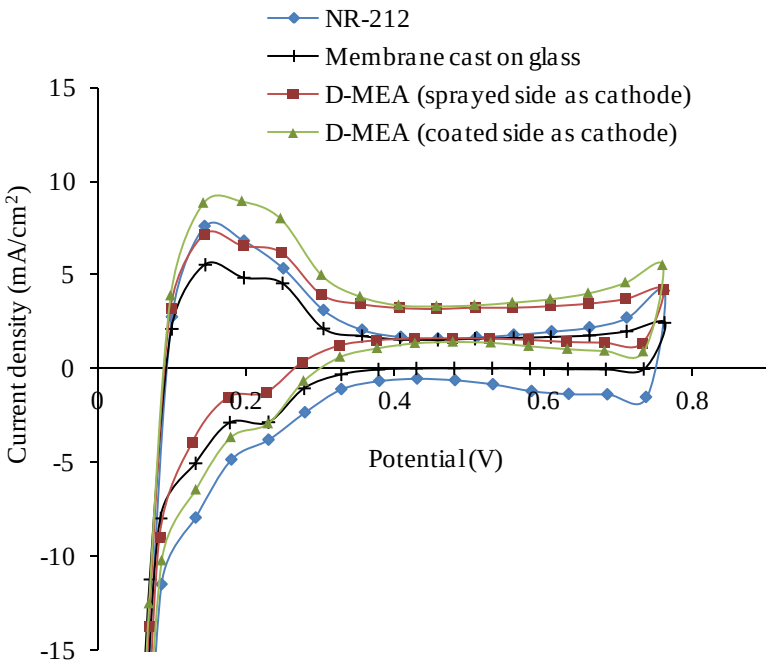

Figure 4.5 Cyclic voltammogram of single cells. Flow rate = 0.2 L/min at anode (H_2) and cathode (N_2). Scan rate = 20 mV s^{-1}. Temperature =35/35/35 ℃ (anode humidifier/cathode humidifier/cell). The reduction charge densities were evaluated within the potential window 0.4 to 0.1 V for ECA calculation in Table 4-1. [50]

Table 4-1 Summarization of the performance test, AC impedance spectroscopy test and cyclic and sweep voltammetry tests. For sweep voltammetry test, scan rate was 2 mV s^{-1}, all other conditions were the same as cyclic voltammetry test as explained in the caption of Figure 4.6. The H_2 crossover current density was chosen at potential value 0.4 V. [50]

		I-V characteristics		Impedance spectroscopy		Cyclic voltammetry	Sweep voltammetry
Samples		**Voltage at 100 mA/cm^2 (V)**	**Voltage at 1000 mA/cm^2 (V)**	**High frequency intercept (Ohm cm^2)**	**Low frequency intercept (Ohm cm^2)**	**Electrochemical active area (m^2/g)**	**Crossover current (mA/cm^2)**
Traditional MEAs	NR - 212	0.823	0.610	0.061	0.646	49.8	0.50
	Membrane cast on glass	0.834	0.618	0.057	0.733	48.5	0.56
D-MEA	Sprayed side as cathode	0.813	0.566	0.068	0.853	48.5	0.73
	Coated side as cathode	0.788	<0.2	0.062	1.049	84.4	

4.4 Conclusions

A new fabrication technique to make an MEA using extrusion slot coating to directly coat membrane solution onto catalyzed GDL was presented. Preliminary coating tests show that the Nafion® dispersion can be directly coated onto the catalyzed GDL, forming a membrane on top of the catalyst layer. However, a critical issue is that an excessive amount of Nafion® penetrates into the catalyst layer during the coating. However, it has been shown that the penetration can be reduced by incorporating an MPL and accelerating the evaporation of the solvents via forced convection. MEAs fabricated by this new technique perform well, when compared to traditional MEAs, however, more work is needed to further increase the performance.

SUMMARY OF PART I

As an applied study for coating porous media, a new MEA fabrication procedure was developed, by which, catalyzed GDLs have been directly coated with Nafion® solution, using a slot die coating technique. Based on the experimental results and discussions in Chapters 2, 3 and 4, the most important conclusions are summarized as follows:

- It is feasible to fabricate MEAs for PEM fuel cells using direct coating polymer electrolyte membrane onto porous catalyzed GDL.
- The number of fabrication steps compared to the conventional MEA manufacturing processes is expected to be reduced, since the membranes will not require a separate fabrication process. Therefore, the new process has the potential to facilitate the mass production of MEAs.
- The coated membranes might be non-uniform because of the roughness and cracks of the catalyzed layer surface. The uniformity of the membrane could be improved by introducing pre-processing operations, such as pressing operation.
- Nafion® solution penetrates into the catalyst layer during the coating process. The penetration could be attenuated by introducing rapid evaporation techniques or an MPL layer.
- An annealing time of 10min in dry conditions is sufficient for making the coated membranes with good strength and performance.
- The penetration of Nafion® solution decreases the porosity of the catalyst layer and alters the balance of its ionic conductivity and electronic conductivity, thus negatively affects the performance of fuel cells.

In Part I of this dissertation, the feasibility, advantages and disadvantages of directly coating porous media as a potential fabrication route for MEAs were clearly elucidated, thus fulfilling the first objective of this dissertation. The results from Part I (Chapter 2-4) are expected to have a direct impact on the PEM fuel cells manufacturing industry, providing valuable data and guidance for the mass production of PEM fuel cells in a cost efficient way. However, the work is broadly applicable to the coating industry.

From the results of Part I, it was found that the penetration of coated Nafion® solution into catalyzed GDL is a dominant factor affecting the performance of fuel cells. Subsequently, this motivated a deeper study specifically on the penetration issue of coating porous media, which is the topic of Part II.

PART II: MODELING OF PENETRATION DEPTH FOR SLOT DIE COATING ONTO POROUS MEDIA

It has been found in Part I that the penetration of coated Nafion® solution into catalyzed GDL is a dominant factor affecting the performance of fuel cells. Actually, the fluid penetration into porous substrates is not only significant in the manufacturing of fuel cells but also an important common technical issue in the coating industry. Predicting and controlling penetration depth while directly coating porous media is not only significant in assuring the desired appearance, properties, and performance of the resulting material, but also important in controlling the cost of production.

The objective of Part II is to fundamentally understand the fluid penetration process and predict the penetration depth when directly coating porous media, using a comprehensive approach. Specifically, computational and analytical models for predicting the penetration depth will be developed and experiments will be conducted to validate the models. Based on these models, the relationship between processing parameters and final penetration depth will be analyzed, for both Newtonian and non-Newtonian fluids. Fulfillment of the research work in Part II will provide effective and efficient analytical tools which can facilitate predicting and controlling the penetration depth for coating porous media. Thus, this work is expected to have a broad impact on the field of coating porous media, contributing to increases in quality and productivity.

CHAPTER 5. INTRODUCTION AND BACKGROUND OF MODELING THE PENETRATION

5.1 Introduction

Several important technical challenges exist with coating porous media: coating uniformity [81], surface morphology [82-84], manufacturing flexibility [85], and penetration depth [15, 36, 42, 86-90] to name a few. Of specific interest is the penetration depth. In general, when coating a porous medium, some level of penetration is desirable to obtain specific material properties, but inadequate or excessive penetration would be limiting. For textile coating, penetration directly affects the bond strength between the coated layer and the substrate [15]. If the penetration depth is too low the desired adhesion of coating to the substrate will not be obtained. For paper printing and coating, penetration of ink directly affects the appearance of the printed paper [32, 33]. Low penetration can even cause ink peel-off [34]; whereas excessive penetration can degrade the surface smoothness of the coated linerboards [1]. In addition, penetration depth also affects the functionality and performance of the resulting material [35]. One example is the coated catalyzed GDLs used in low-temperature PEM fuel cells. It has been shown in Part I of this dissertation that excessive penetration restricts gas transport and alters the balance of ionic conductivity and electronic conductivity, thus, reducing the performance of the fuel cell. Furthermore, penetration changes the coating parameters needed for a desired film thickness and the operational limits of the coating process, and thus affects the cost of the production. Both too high or too low of a coating thickness can lead to unwarranted expense [36]. Therefore, predicting and controlling penetration depth when directly coating porous media is not only significant in assuring the desired appearance, properties,

and performance of the resulting material, but also important in controlling the cost of production. In spite of its importance, only limited studies exist to fundamentally understand the penetration process and to predict the penetration based on industrial-scale coating processes.

5.2 Previous modeling work

When modeling the fluid penetration when directly coating porous media, one major concern is how to model the flow of fluid in the porous media. Several traditional methods exist. The micro-scale approaches include the pore-network model [36, 42], Lattice-Boltzmann method, [91, 92] or solving the Navier-Stokes equations [93]. All of these micro-scale methods require detailed morphology information of the porous media, the geometrical details, and even an extremely fine mesh of the microstructure of the porous media to simulate the flow behavior. Thus, they are computationally time consuming and are typically applied only to small domains. From the macro-scale, simpler governing equations, such as Darcy's law, have been used [94]. Darcy's law does not need the microstructural information through the porous media; instead it uses the permeability and porosity to describe the transport characteristics of the porous media. However, it is still difficult to couple the fluid flow in the porous media (called porous flow) governed by the 2-D Darcy's law with the free flow field of the coating bead (called free flow) in a coating process. The convergence is problematic due to the complex coupling of pressure, velocity, and phase variable between the porous flow and free flow. Furthermore, the quantity of elements for the porous flow domain can be large for specific conditions, which will cause a time consuming calculation. In this study, a new approach based on 1-D Darcy's law is proposed to simulate the penetration when coating porous media.

Specifically, a computational fluid dynamics (CFD) model embedded with control points is used to simulate the penetration process.

Another major concern of modeling fluid penetration when directly coating porous media is how to determine the pressure in the coating bead. In this region, the flow in the coating bead is coupled with the flow in the porous media, which means the pressure in the coating bead and the penetration in porous media are dependent on one another. However, for simplification, some modeling approaches decouple these two flows. Letzelter and Eklund [88, 89] assumed a piece-wise constant pressure distribution in their analytical model to predict the dewatering behavior in a blade-coating process on paper. Yesilalan and Warner [15] derived an analytical equation to predict the maximum possible penetration depth into a woven fabric during the blade-coating process. In their model, the pressure distribution on the porous substrate was approximated by the pressure distribution for coating onto a solid substrate, which was derived from lubrication theory. The penetration process was modeled by the 1-D Darcy's law. Their predicted penetration depths were about three times less than the measured depths and only qualitatively showed the same trend as the experimental results.

Although an approximate pressure distribution simplifies the model, it introduces error, which may not be trivial for specific conditions. To avoid such error, some researchers coupled the flow in the coating bead to the flow in porous media. Chen and Scriven [90] developed an analytical model to predict the penetration of fluid into a porous substrate for a flooded-nip-blade coating process. Their model used a modified lubrication theory, which calculates the pressure field and penetration depth simultaneously. In addition, their model accounted for substrate deformation and trapped

air compression. Ninness et al. [87] used a similar method to study the penetration of coating fluid into the porous web for a metered-sized-press coating process. Devisetti and Bousfield [86] extended the model of Ninness et al. by taking into account the deformation of the rubber covered roll during roll coating. They experimentally measured the pressure profile, rubber deformation and film thickness and found that high-viscosity-fluid behavior agrees well with model predictions. Compared with the work using approximate pressure distributions, model predictions that couple the two flows more realistically agree with the actual dynamics, resulting in more reasonable pressure distribution and penetration depth. However, one drawback of these analytical models is that they do not provide an easily solved explicit expression of the final penetration depth. Instead they consist of solving several equations by a finite-difference technique, which is relatively complex.

Non-continuum modeling work has also been conducted. Ghassemzadeh et al. [36, 42] conducted extensive simulations on liquid penetration into paper during a slot-coating process. They built a 3-D pore network model of the paper based on the representative statistical distribution of its microstructure. Their model allows for the effect of micro-structural characteristics of paper on penetration to be studied, and it more precisely depicts the spatial distribution of a coating fluid in the paper compared with the above macro-scale models [15, 86-90]. However, modeling the microstructure of paper requires morphological information, which is usually difficult to measure [95]. In addition, similar to models developed by Letzelter and Eklund [88], as well as Yesilalan et al. [15], the model developed by Ghassemzadeh et al. does not couple the flow in the coating bead with the

flow in the porous media. Specifically, only approximate pressure distributions were applied on top of the paper to mimic the pressure effect from the coating bead.

5.3 Limitations of previous modeling work

Previous modeling work has been summarized and compared in Table 5-1.

It can be seen from Table 5-1 that previous modeling work has the following limitations:

- Some previous models decouple the flow in the coating bead and the flow in the porous media [15, 36, 42, 88, 89, 95].
- Those models which couple two flows together do not provide a simple expression of the penetration depth and require a complex calculation procedure [86, 87, 90].
- All modeling work in previous studies are for Newtonian fluids in spite of most solutions used in the coating industry are non-Newtonian.
- Only very limited experimental data are available to validate the predicted penetration depth, possibly due to the difficulty of the measuring penetration depth inside of the porous media.

Based on previous studies, it is evident that the analytical relationship between processing parameters and the final penetration depth is still not clear nor is it well understood, and more experimental work must be conducted to validate the accuracy of modeling work.

Table 5-1 Summary of previous modeling work of penetration depth

Authors	Governing equations		Coupling	Coating method	Numerical /analytical	Fluid type	Experimental validation
	in coating bead	in porous media					
K. Chen and L. Scriven [90]	Lubrication theory	Darcy's law	Yes	Blade coating	Analytical (iterative)	Newtonian	No
P. Letzelter and D. Eklund [88, 89]	Piece-wise constant pressure distribution	Kozeny-Carman equation	No	Blade coating	Analytical	Newtonian	No
B. Ninness, et al. [87]	Lubrication theory	Darcy's law	Yes	Metered size press	Analytical (iterative)	Newtonian	No
J. Ghassemzadeh et al. [36, 42]	Navier-Stokes equations	Pore network model	No	Slot die coating	Numerical	Newtonian	No
H. Yesilalan et al. [15]	Lubrication theory	Darcy's law	No	Blade coating	Analytical (iterative)	Newtonian	Very limited
S. Devisetti and D. Bousfield [86]	Lubrication theory	Darcy's law	Yes	Roll coating	Analytical (iterative)	Newtonian	No*

***** Provided experimental results are not the measurement of penetration depth.

5.4 Plan for current modeling work

In order to overcome drawbacks of the above modeling approaches, a framework that can be utilized to understand and predict the penetration depth of direct coating on porous media will be developed. Specifically, two series of models will be developed, one using CFD and the other based on analytical methods, for coating Newtonian and non-Newtonian fluids. Using CFD, Navier-Stokes equations will be solved to account for flow in the coating bead, while simultaneously solving the flow in the porous media. Analytical models will be developed to provide simple expressions of final penetration depth based on lubrication equations for Newtonian and non-Newtonian fluids [96], Darcy's law and a modified Blake-Kozeny equation [97, 98]. With these models the penetration depth can be quickly solved while accounting for the influence of material properties and processing conditions. In the current study slot die coating will be the processing method considered.

5.5 Modeling domain

A localized view of the slot-die coating process on a porous substrate and the main influential parameters are shown in Figure 5.1. The coated fluid is delivered at a constant 2-D flow rate, *Q*, from a fixed slot gap, *W*, onto a moving substrate with a coating speed, *V*. It can be seen from Figure 5.1 that penetration starts from a point between the left die lip and the gap of the slot die and continues until the liquid has transformed to a solid film. Based on the governing forces of penetration and the state of coated fluid, the coating process can be divided into three regions, as shown in Figure 5.1. In Region I, the penetration is mainly governed by the pressure in the coating bead and the capillary force in the porous media. The pressure pushes the fluid into the substrate,

while the capillary force can either absorb or prevent fluid penetration into the pores of the substrate depending on the wetting properties (e.g., contact angle). The time that the substrate is exposed to this region is usually very short; it could be as short as milliseconds [36]. Thus, the fluid properties can be taken as constant in this region. In Region II, the coated fluid undergoes a phase transition from liquid to solid, which is usually controlled by the evaporation of the solvent. During this process, the rate of penetration is mainly governed by capillary forces. Gravity effects are typically ignored in Regions I and II. The significance of gravitational force depends on its relative magnitude compared with viscous and capillary forces. In Region III, the coated fluid has fully transformed into solid film. Hence, a portion of the coated material remains atop the substrate, forming a solid film; while another portion fills the pores of the porous media. Coating porous media by using other techniques like roll coating and blade coating could be divided into the similar regions like Figure 5.1.

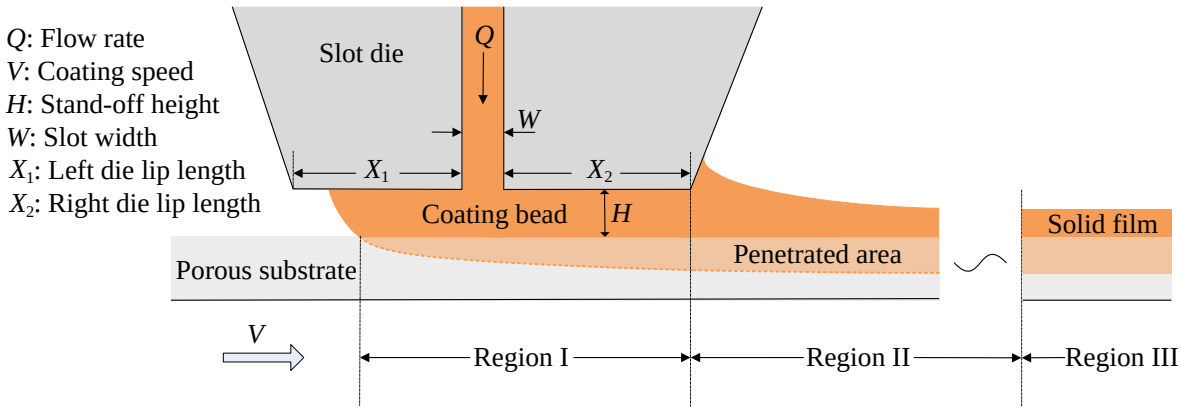

Figure 5.1 Schematic illustrating the slot die coating on a porous substrate. [99]

Earlier studies that focused on fluid penetration into porous media have been limited to penetration in Region I. This restriction is possibly due to the uncertainty of

material properties of Region II, which makes it difficult to model the penetration of that region. However, if the coating fluid is highly viscous, and if the capillary force and gravitational force are relatively small, the penetration changes during the phase transition process will be relatively small. As previous studies, the penetration in Region I will be modeled in current study (Chapter 6 and 7). In addition, the penetration in Region II will also be discussed (Chapter 9).

5.6 Assumption of capillary pressure

The capillary pressure can either absorb or prevent fluid penetration into the porous media depending on the magnitude of the contact angle. If the contact angle is lower than 90°, the capillary pressure is expected to absorb the fluid into the porous media, since it will have a hydrophilic nature. Otherwise, the fluid will be repelled because of the hydrophobic nature. The contact angle and capillary pressure with the two phase flow in the porous media are very complex issues [100, 101]. Either the actual contact angle or the capillary pressure is not a constant value [102]. The discussion of dynamic contact angle or dynamic capillary pressure is out of the scope of current study. In this study, for simplification, the capillary pressure is assumed to be approximately constant to evaluate the overall capillary effect during the penetration process. The capillary pressure is defined as a constant positive value when it absorbs the fluid into the porous media (hydrophilic or contact angle < 90°); or a negative value when it pushes fluid out of the porous media (hydrophobic or contact angle > 90°).

CHAPTER 6. CFD MODELING OF PENETRATION DEPTH

6.1 Introduction

In this chapter, CFD models using commercial software, COMSOL 4.2a, are developed to study the penetration process of slot die coating on porous media. Models for Newtonian and non-Newtonian fluids are developed separately. The penetration depth and pressure distribution along the porous media are calculated using the CFD model for Newtonian fluids to illustrate the characteristics of the penetration process. Important conclusions from this chapter will be used as the basis for making assumptions for analytical models in the following chapter. This chapter is based on published work by Ding et al. [99, 103]

6.2 Geometry and boundary conditions

COMSOL 4.2a is used in this study to develop CFD models. The geometry and boundary conditions of CFD models are shown in Figure 6.1. The reference pressure (atmosphere pressure) is set to zero. The domain is a Laminar Two-Phase Flow (Level set) module, which is a standard module in COMSOL. As shown in Figure 6.1, the slot die is composed of several no-slip walls, and the porous media substrate is composed of two moving walls and several control points that create small outlets (leaking walls) between adjacent control points. Control points are used to simulate the penetration process in the porous media substrate. They are only applied under the slot die because the penetration in Region I is of interest.

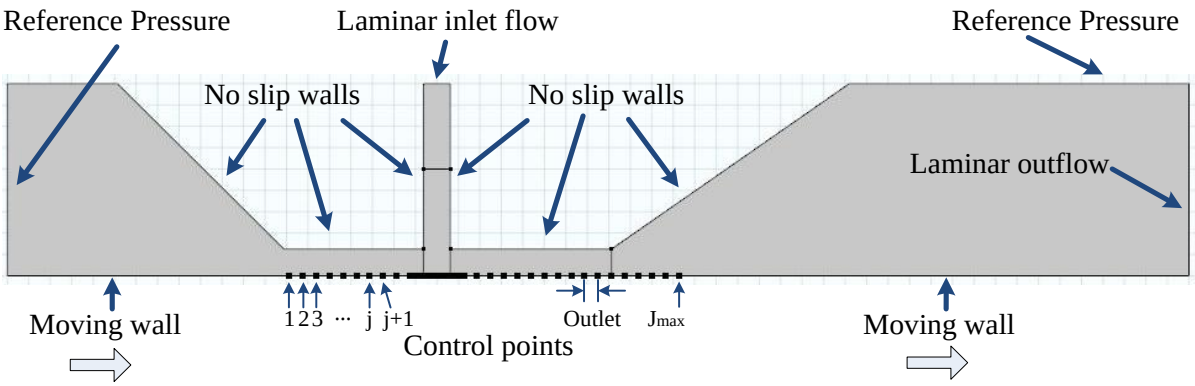

Figure 6.1 Geometry and boundary conditions of the COMSOL Model. [99]

6.3 CFD Model for coating Newtonian fluids

For a Newtonian fluid, 1-D Darcy's law is applied on every control point to satisfy the relationship between the pressure and penetration velocity at each corresponding point. This relationship is based on the 1-D assumption, which is valid when the wetting length (length of Region I) is much longer than the penetration depth. This assumption is reasonable for practical conditions because the length of Region I is normally on the order of millimeters whereas the penetration depth is on the order of microns. As shown in Figure 6.1, each control point is indexed by $j=1,2,3...J_{max}$; and three parameters, pressure (p_j), penetration depth (h_j) and vertical velocity (u_j), are defined on each point. Darcy's law is given by:

$$u_j = \frac{p_j + p_c}{h_j} \cdot \frac{k}{\mu} \tag{6.1}$$

where k is the permeability of the porous media, p_c is the capillary pressure in the porous media, and μ is the viscosity of the coated fluid. The penetration depth is a function of time, Δt, which is an interval time moving from point j-1 to point j. Thus h_j for any given point along the porous domain is given by:

$$h_j = h_{j-1} + \frac{u_{j-1}}{\varepsilon}\Delta t \tag{6.2}$$

where ε is the porosity of the porous media and $\frac{u_{j-1}}{\varepsilon}$ is the penetration velocity at control point *j-1*. Δt can be determined through the relation: $\Delta t = \Delta s/V$, where Δs is the distance between adjacent control points, and V is coating speed (speed of substrate). Equations (6.1) and (6.2) above ensure momentum conservation and mass conservation in the porous media, respectively.

In addition to control points, the substrate between two adjacent points is defined as a leaking wall with the horizontal moving speed, $u_x = V$, and leaking speed, $u_y = (u_j + u_{j+1})/2$ (average vertical fluid velocity between two adjacent points). The initial value of h_j, which is the initial penetration depth, should be zero; however, to avoid a singularity of u_j, the initial penetration depth is defined as 1 μm. Based on a mesh refinement study, it was shown that changing the initial penetration depth from 0.5 to 3 μm had a negligible effect on the final penetration depth, thus setting the initial penetration to 1 μm was determined to be sufficient. During each time step, the solution is iterated from point $j=1$ to point $j=J_{max}$ and the pressure (p_j), penetration velocity (u_j) and penetration depth (h_j) are calculated at each point.

The basic iteration procedure is the same for a positive or a negative capillary pressure. However, for a negative capillary pressure, the penetration only occurs when $p_j - p_c$ is higher than zero. Thus, during the iteration, the value of p_j must be compared with p_c, to determine whether penetration occurs at point j or not. When p_c is higher than p_j, u_j is assumed to be zero. This means that in this model the fluid can only penetrate into the porous media, but cannot be pushed out of the porous media.

The dynamic contact line (left beginning of Region I in Figure 5.1) is unknown initially and thus does not necessarily coincide with point *j=1*. However, to be conservative, control points are applied along the length of the lower meniscus boundary to ensure that the dynamic contact line is located in the region of the control points. Before each time step, each control point is assessed as air or liquid. If it is air (which is true for those control points in front of the dynamic contact line) the penetration depth remains 1 μm, i.e., the same as the initial condition.

6.4 CFD Model for coating non-Newtonian fluids

For a non-Newtonian fluid, the power law model is usually used to describe its rheological properties, by: $\mu_{app} = m\dot{\gamma}^{n-1}$, where μ_{app} is the apparent viscosity, and m is the consistency index and n is the flow behavior index, which are constants that depend on the specific material. Instead of 1-D Darcy's law, the modified Blake-Kozeny equation [97, 98] for 1-D flow of power-law fluids through porous media is applied on each control point. The modified Blake-Kozeny equation is given by:

$$u_j = \left(\frac{k}{\mu_{eff}} \frac{p_j + p_c}{h_j} \right)^{\frac{1}{n}} \tag{6.3}$$

where μ_{eff} is an effective viscosity defined by: $\mu_{eff} = \frac{m}{12}(9+\frac{3}{n})^n (150k\varepsilon)^{(1-n)/2}$. Thus, for a non-Newtonian fluid, Equation (6.3) replaces equation (6.1) as the momentum equation, while Equation (6.2) is still used to account for the mass conservation.

6.5 Case study and discussion

A Newtonian fluid is coated onto a porous medium using the developed CFD model. Calculations are conducted using the following conditions: $Q = 1\times10^{-6}$ m^2/s (2-D

flow rate), V = 3.5 mm/s, μ = 0.4 Pa-s, $k = 9.375 \times 10^{-13}$ m^2, ε = 0.75, p_c = 0. The geometry of the slot die coating configuration is shown in Figure 6.2. A predefined mesh by the software is used, in which the maximum element size is 0.05 mm. Δs directly below the slot is 0.0417 mm to capture the relatively high velocity gradient in this region, in the remaining section Δs is 0.125 mm. It has been shown that this element size and range of Δs are sufficiently small to ensure good convergence of the simulated results based on coating conditions and parameters used in this study.

The penetration depth and pressure distribution along the porous media calculated from the CFD model are shown in Figure 6.2(b) and (c), respectively, as an example to illustrate the characteristics of the penetration process during slot coating on porous media. For comparison, the pressure distribution on a solid substrate, while leaving other parameters unchanged, is also provided. From Figure 6.2(b), it can be seen that the penetration depth increases nearly linearly along the left channel. In contrast, along the right channel (in the x direction) the depth increases more slowly and approaches a constant value at the outlet of the slot die.

From Figure 6.2(c), it can be seen that the pressure increases gradually along the left channel and decreases gradually along the right channel (in the x direction). Based on Darcy's law, the penetration velocity increases as pressure increases but the velocity diminishes as penetration depth increases. In the left channel, the effects of pressure increase and penetration depth increase on penetration velocity will balance, resulting in an approximately constant penetration velocity (i.e., the penetration depth increases linearly). In the right channel, the effects of pressure decrease and penetration depth

increase on the penetration velocity results in a decreasing penetration velocity (i.e., the increase of penetration depth slows down gradually).

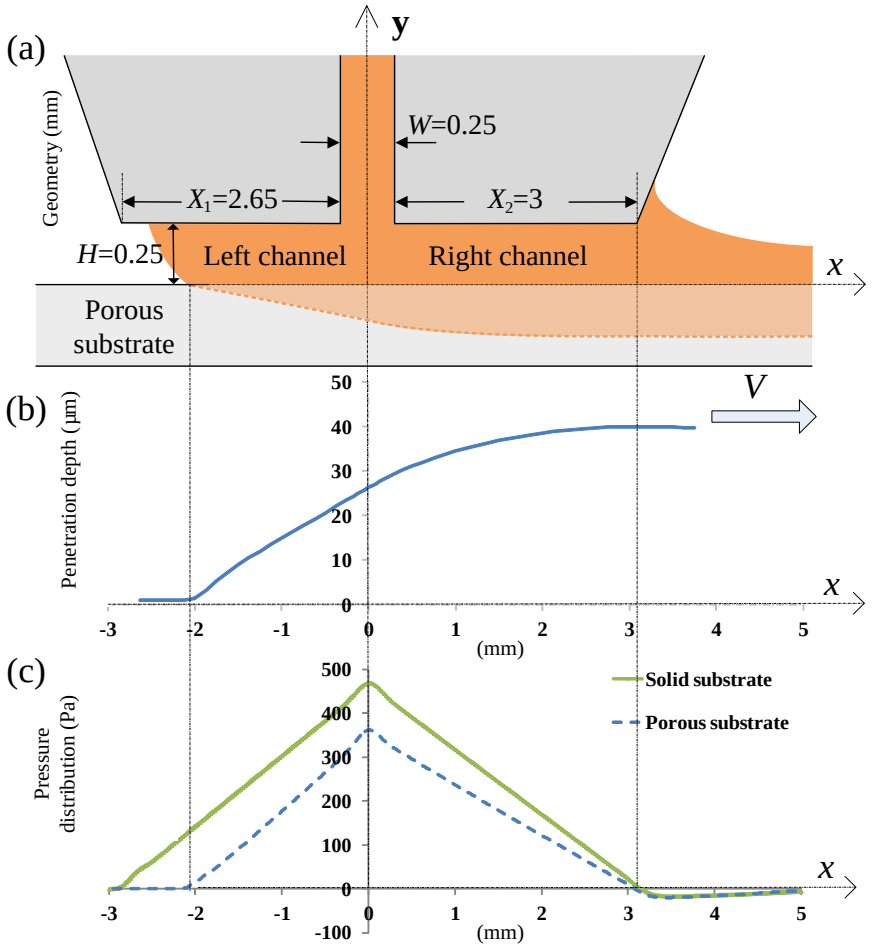

Figure 6.2 The a) geometry of the slot coating configuration, and b) simulated penetration depth and c) pressure distribution from the CFD model. (The vertical line with x = 0 coincides with the centerline of the slot). [99]

In addition, it can also be seen from Figure 6.2(c) that the magnitude of the pressure on the porous substrate is lower than that on the solid substrate. This difference demonstrates that estimating the pressure based on a solid substrate, as done in previous modeling work [15, 36, 42, 88, 89], will over predict the penetration depth. It is further noted that the pressure distribution on the porous media is still close to linear. Furthermore, the

pressure gradient in the left channel does not change significantly, while the pressure gradient in the right channel is apparently smaller on the porous media. The above phenomena will be used as the basis for making assumptions for the analytical models in the following chapter.

CHAPTER 7. ANALYTICAL MODELING OF PENETRATION DEPTH

7.1 Introduction

In this chapter, several analytical models for penetration depth during slot die coating on porous substrates are developed for both Newtonian and non-Newtonian fluids with/without considering capillary pressure. These models are derived based on the lubrication equations for Newtonian and non-Newtonian fluids [96], Darcy's law and the modified Blake-Kozeny equation [97, 98].

7.2 Modeling assumptions

The following assumptions are used during the derivation:

1) When coating a Newtonian fluid, penetration in the porous media satisfies 1-D Darcy's law; whereas when coating a non-Newtonian fluid it satisfies the 1-D modified Blake-Kozeny equation.

2) Flow in the coating bead is laminar and fully developed.

3) Capillary pressure in the porous media is assumed to be a constant value (zero, positive or negative); whereas the capillary effect on the upstream and downstream menisci of the coating bead is ignored.

4) Penetration velocity is relatively slow, and the total penetration flow rate is much slower than the total flow rate, Q.

5) The coating is assumed to be formed at a relatively high coating speed for the materials considered.

6) The right channel length, L_2, is much longer than either the slot width, W, or the stand-off height, H.

7.3 Analytical penetration depth for coating Newtonian fluids without capillary pressure

In this section, only the penetration driven by the pressure from the coating bead is considered, i.e., the capillary pressure in the porous media is assumed to be zero. Nomenclature found in Figure 5.1 and Figure 7.1 is used during the derivation.

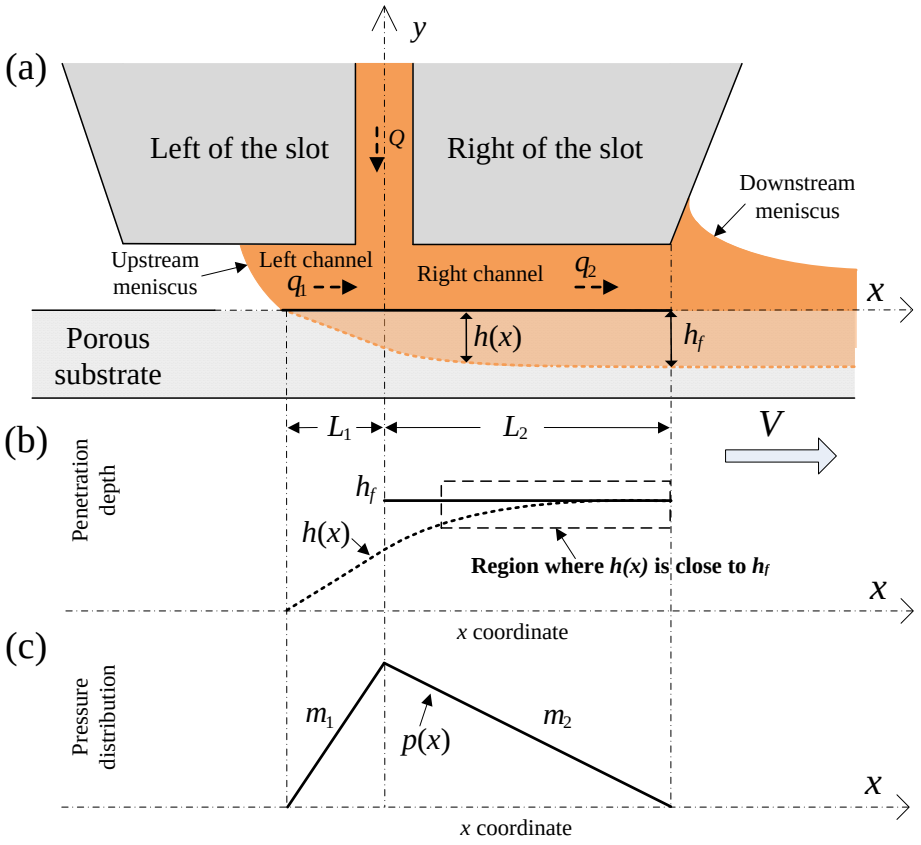

Figure 7.1 Schematic of a) the slot die configuration and b) analytical penetration depth and c) pressure distribution. [99]

For a Newtonian fluid, the penetration velocity (superficial velocity), v_p, at any point along the porous media is obtained by applying 1-D Darcy's law and is given by

$$v_p(x) = \frac{k}{\mu\varepsilon}\frac{dp}{dy} = \frac{k}{\mu\varepsilon}\frac{p(x)}{h(x)} \tag{7.3.1}$$

The pressure distribution in the coating bead, $p(x)$, and the penetration depth, $h(x)$, are functions of coordinate x, as shown in Figure 7.1. v_p is also given by

$$v_p(x) = \frac{d[h(x)]}{dt} = \frac{d[h(x)]}{dx}\frac{dx}{dt} = \frac{d[h(x)]}{dx}V \tag{7.3.2}$$

Substituting Equation (7.3.2) into Equation (7.3.1) yields:

$$h(x)\cdot d[h(x)] = \frac{k}{\mu V\varepsilon}\, p(x)\cdot dx \tag{7.3.3}$$

For slot-die coating, if the flow is laminar, capillary effects on the upstream and downstream menisci are ignored, and if the penetration flow rate is relatively small (Assumptions 2 to 4). A modified lubrication theory [87] can be applied to the left channel and right channel (Figure 7.1(a)), respectively, to determine the pressure gradients (absolute values), m_1 and m_2

$$m_1 = \frac{6\mu(VH - 2q_1)}{H^3} \text{ (left channel)} \tag{7.3.4}$$

$$m_2 = \frac{-6\mu(VH - 2q_2)}{H^3} \text{ (right channel)} \tag{7.3.5}$$

where q_1 and q_2, are the flow rates in the channel. When coating on a solid substrate, the flow rate in left channel, q_1, equals zero; the flow rate in the right channel, q_2, equals the inlet flow rate Q. When coating on a porous substrate, due to the effect of penetration, the flow rates in the channel and pressure gradients are functions of x. However, if the flow rate of penetration is much smaller than the total flow rate, Q (Assumption 4); q_1 and q_2 can be assumed to be constants resulting in m_1 and m_2 also being constants. In this case,

the pressure distribution will be linear along both the left channel and the right channel. The obtained expressions of pressure distribution, *p(x)*, are given by

$$p(x) = m_1(L_1 + x) \quad (x < 0, \text{ left channel}) \tag{7.3.6}$$

$$p(x) = m_2(L_2 - x) \quad (x > 0, \text{ right channel}) \tag{7.3.7}$$

Substituting Equation (7.3.6) into Equation (7.3.3) and integrating from $-L_1$ to x ($-L_1 \le x \le 0$) gives the expression of penetration depth, $h(x)$, in the left channel

$$h(x) = \sqrt{\frac{m_1 k}{\mu V \varepsilon}}(L_1 + x) \tag{7.3.8}$$

Substituting $x = 0$ into Equation (7.3.8) gives the expression of the penetration depth at $x = 0$, h_0

$$h_0 = \sqrt{\frac{m_1 k}{\mu V \varepsilon}} L_1 \tag{7.3.9}$$

Substituting Equation (7.3.7) into Equation (7.3.3), integrating from 0 to x ($L_2 \ge x \ge 0$), and using the relation, $L_1 = \frac{m_2 L_2}{m_1}$, and using the expression of h_0, gives the expression of penetration depth, $h(x)$, in the right channel

$$h(x) = \sqrt{\frac{m_2 k}{\mu V \varepsilon}\left[-x^2 + 2L_2 x + \frac{{L_2}^2 m_2}{m_1}\right]} \tag{7.3.10}$$

From Equations (7.3.8) and (7.3.10), it can be seen that along the left channel $h(x)$ is a linear function. In contrast, along the right channel the slope of $h(x)$ decreases with x. The relationship between $h(x)$ and x is depicted by the dashed curve in Figure 7.1(b). This relationship has been found using the CFD model in Section 6.5. The penetration depth described by Equations (7.3.8) and (7.3.10) does not depend on viscosity because the

explicit and implicit viscosity terms in m_1 and m_2 will cancel. Substituting $x = L_2$ into Equation (7.3.10) gives the final penetration depth at the outlet of slot die, h_f

$$h_f = \sqrt{\frac{m_2 k}{\mu V \varepsilon}(1+\frac{m_2}{m_1})L_2^{\,2}} \tag{7.3.11}$$

In order to calculate h_f in Equation (7.3.11), the pressure gradients of coating on a porous substrate, m_1 and m_2, must be determined. Determining m_1 and m_2 is not trivial due to the effect of penetration. Previous modeling work [15, 36, 42, 88, 89] used the pressure distribution on a solid substrate to approximate the pressure distribution on a porous substrate. Based on the result of CFD model in Section 6.5, it has been demonstrated that this approximation method will over predict the penetration depth. In this study, m_1 and m_2 are analytically approximated based on the assumptions previously discussed.

In practice, high coating velocities are always desired to increase the production rate (Assumption 5). If the coating velocity is relatively high, the upstream dynamic contact line will be close to the slot, i.e., L_1 will be relatively small. By assuming that the penetration velocity is relatively slow (Assumption 4), the total penetration in the left channel will be negligible. Thus, the flow rate in the left channel, q_1, can be approximated as zero, consistent with coating on a solid substrate. For the right channel, based on the assumption that L_2 is much longer than W and H (Assumption 6) and understanding that the slope of $h(x)$ decreases with x, the penetration depth in most of the right channel is expected to be close to the final penetration depth at the outlet, h_f, as depicted by the dashed box in Figure 7.1(b). Therefore, the flow rate along the right channel, q_2, can be approximated by the final flow rate at the outlet which is given by $Q - h_f V \varepsilon$.

Substituting , q_1 and q_2 into Equations (7.3.4) and (7.3.5) gives:

$$m_1 \approx \frac{6\mu V}{H^2} \text{ (left channel)} \tag{7.3.12}$$

$$m_2 \approx \frac{-6\mu[VH - 2(Q - h_f V\varepsilon)]}{H^3} \text{ (right channel)} \tag{7.3.13}$$

Equations (7.3.12) and (7.3.13) mean that the pressure distribution on the porous media is still close to linear based on the assumptions discussed above. Furthermore, the pressure gradient in the left channel for a porous substrate is close to that of a solid substrate; whereas in the right channel, the pressure gradient of the porous media is apparently smaller than that of a solid substrate. This phenomenon coincides with observations found by using CFD model in Section 6.5. Substituting Equation (7.3.12) into Equation (7.3.11) and solving Equations (7.3.11) and (7.3.13) gives an quadratic function of h_f

$$A \cdot h_f^{\,2} + B \cdot h_f + C = 0 \tag{7.3.14}$$

where A, B, and C are constants

$$A = \frac{24kL_2^{\,2}\varepsilon}{H^4} - 1,\ B = \frac{12kL_2^{\,2}(VH - 4Q)}{H^4 V}, \text{ and } C = \frac{12kL_2^{\,2}Q(2Q - VH)}{H^4 V^2 \varepsilon}$$

Mathematically, there might be two roots of h_f. However, as will be demonstrated in Section 7.4, only one of them is physically meaningful, which is given by

$$h_f = \frac{-B - \sqrt{B^2 - 4AC}}{2A} \tag{7.3.15}$$

Equation (7.3.15) is an explicit analytical expression that can be used to calculate the final penetration depth of a Newtonian fluid slot coated onto a porous media.

7.4 Determination of the physically correct penetration depth for the explicit model

The left side of Equation (7.3.14) can be written as a parabola

$$f(h_f) = A \cdot h_f{}^2 + B \cdot h_f + C \tag{7.4.1}$$

The roots of Equation (7.3.14) are intersection points between the parabola (7.4.1) and the horizontal line $f(h_f) = 0$. Two possible intersections are $(\frac{-B+\sqrt{B^2-4AC}}{2A}, 0)$ and $(\frac{-B-\sqrt{B^2-4AC}}{2A}, 0)$.

Substituting $h_f = \frac{Q}{V\varepsilon}$ into (7.4.1) obtains $f(\frac{Q}{V\varepsilon}) = -\frac{Q}{V\varepsilon}$. Therefore the parabola (7.4.1) passes through the point $(\frac{Q}{V\varepsilon}, -\frac{Q}{V\varepsilon})$. It is also apparent that parabola (7.4.1) always pass through the point (0, *C*). The sign of the *C* value can be discussed in the following way. Based on lubrication theory, the pressure gradient in the left channel for coating a solid substrate is approximately $\frac{6\mu V}{H^2}$ (Equation (7.3.12)), which is a positive value. Thus, the pressure in the left channel gradually increases with *x*, as shown in Figure 7.1(c). If the capillary effects on the upstream and downstream menisci of the coating bead are ignored (Assumption 3), the pressure at the outlet will be close to zero. Therefore the pressure gradient in the right channel must be negative, i.e., the pressure must gradually decrease with *x* in the right channel and gradually approaches to zero at the outlet. Based on lubrication theory, this means that $VH - 2Q$ in the pressure gradient terms is a negative value. This is the reason why there is a negative sign in the expression of the absolute pressure gradient in the right channel (Equations (7.3.5) and (7.3.13)). If $VH - 2Q$ is negative, it can be seen from the expression of *C* in Equation (7.3.14) that *C* must be positive.

It is also known that the opening direction of the parabola (7.4.1) is determined by the sign of the A value. The A value can either be positive or negative in the current study. If A is positive, the parabola opens up, and it can be seen that $\frac{-B-\sqrt{B^2-4AC}}{2A} < \frac{-B+\sqrt{B^2-4AC}}{2A}$. However, if A is negative, the parabola opens down, and it can be seen that $\frac{-B-\sqrt{B^2-4AC}}{2A} > \frac{-B+\sqrt{B^2-4AC}}{2A}$. Based on previous discussion, the schematic of the parabola (7.4.1) will look like Figure 7.2(a) for $A > 0$ and (b) for $A < 0$.

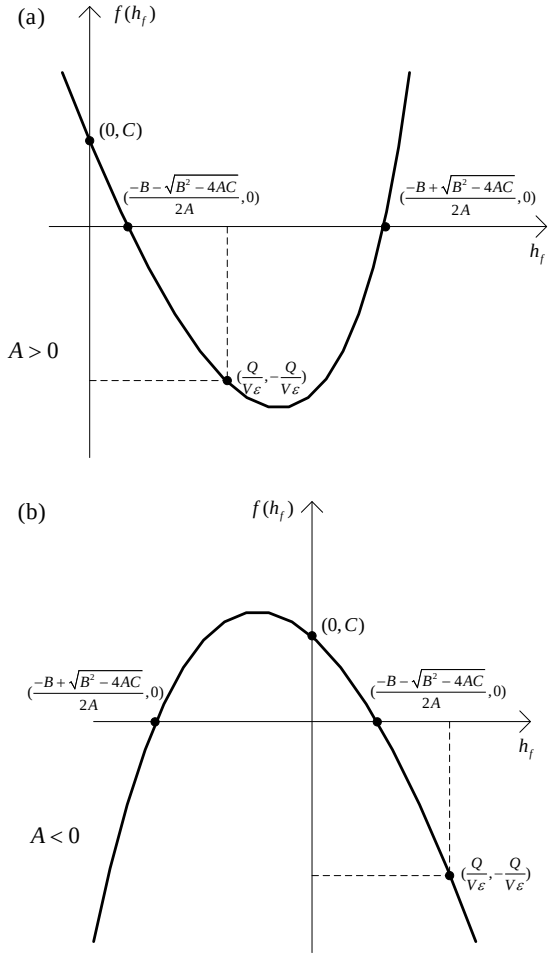

Figure 7.2 Schematic of the parabola equation (7.4.1). (a) $A > 0$, (b) $A < 0$.

For a reasonable physical meaning, h_f must be a positive value. In addition, the penetration flow rate, $h_f V\varepsilon$, must be smaller than the total flow rate, Q. Thus, h_f must be smaller than $\frac{Q}{V\varepsilon}$. Therefore, h_f is a value between 0 and $\frac{Q}{V\varepsilon}$. It can be seen from Figure 7.2 that $\frac{-B-\sqrt{B^2-4AC}}{2A}$ is the only possible root for both $A > 0$ and $A < 0$ cases. That is why expression (7.3.15) is the physically correct penetration depth.

7.5 Analytical penetration depth for coating non-Newtonian fluids without capillary pressure

In this section, an analytical expression for penetration depth of non-Newtonian fluids without considering capillary pressure is derived. Only the penetration driven by the pressure from the coating bead is considered. Nomenclature found in Figure 5.1 and Figure 7.1 is used during the derivation.

When coating a non-Newtonian fluid, the 1-D modified Blake-Kozeny equation is used [97, 98], which is given by

$$v_p = \left[\frac{k}{\mu_{eff}}\frac{p(x)}{h(x)}\right]^{1/n}\frac{1}{\varepsilon} \tag{7.5.1}$$

In addition, a generalized lubrication theory for non-Newtonian fluids derived by Dien and Elrod [96] is used to approximately calculate the absolute values of pressure gradients, which are given by

$$m_3 = \frac{6\bar{\mu}(VH-2q_1)}{H^3} \text{ (left channel)} \tag{7.5.2}$$

$$m_4 = \frac{-6\bar{\mu}(VH-2q_2)}{H^3} \text{ (right channel)} \tag{7.5.3}$$

where $\bar{\mu} \equiv mn\left(\frac{V}{H}\right)^{n-1}$.

Equations (7.5.2) and (7.5.3) can give a good approximation for pressure gradient when the flow behavior index of a non-Newtonian fluid, *n*, is higher than 0.5 and the flow rate in the channel is between 0.2*VH* to 0.8*VH* [96]. For current derivation, a similar approach to that used for a Newtonian fluid is taken. However, Equation (7.3.1) is replaced by Equation (7.5.1); Equations (7.3.4) and (7.3.5) are replaced by Equations (7.5.2) and (7.5.3). The remaining derivation procedure and assumptions are the same as those for coating a Newtonian fluid.

Specifically, substituting Equation (7.3.2) into Equation (7.5.1) yields

$$\left[h(x)\right]^{1/n} \cdot d\left[h(x)\right] = \left(\frac{k \cdot p(x)}{\mu_{eff}}\right)^{1/n} \frac{1}{V\varepsilon} \cdot dx \tag{7.5.4}$$

where $p(x)$ is given by

$$p(x) = m_3(L_1 + x) \text{ (left channel)} \tag{7.5.5}$$

$$p(x) = m_4(L_2 - x) \text{ (right channel)} \tag{7.5.6}$$

Substituting Equation (7.5.5) into Equation (7.5.4) and integrating from $-L_1$ to x ($-L_1 \le x \le 0$) gives the expression of penetration depth, $h(x)$, in the left channel

$$\left[h(x)\right]^{(n+1)/n} = \left(\frac{k}{\mu_{eff}}\right)^{1/n} \frac{1}{V\varepsilon m_3}\left[m_3 \cdot (L_1 + x)\right]^{(n+1)/n} \tag{7.5.7}$$

Substituting $x = 0$ into Equation (7.5.7) gives the expression of the penetration depth at $x = 0$, h_0

$$h_0{}^{(n+1)/n} = \left(\frac{k}{\mu_{eff}}\right)^{1/n} \frac{1}{V\varepsilon m_3}\left(m_3 L_1\right)^{(n+1)/n} \tag{7.5.8}$$

Substituting Equation (7.5.6) into Equation (7.5.4), integrating from 0 to x ($L_2 \geq x \geq 0$), and using the relation, $L_1 = \frac{m_4 L_2}{m_3}$, and using the expression of h_0, gives the expression of penetration depth, $h(x)$, in the right channel as

$$h(x)^{(n+1)/n} = \left(\frac{k}{\mu_{eff}}\right)^{1/n} \frac{1}{V\varepsilon}\left\{m_3^{1/n} \cdot L_1^{(n+1)/n} + m_4^{1/n} \cdot \left[L_2^{(n+1)/n} - (L_2 - x)^{(n+1)/n}\right]\right\} \quad (7.5.9)$$

where the absolute values of pressure gradients, m_3 and m_4, can be approximated using the same approximation of q_1 and q_2 as those for coating a Newtonian fluid. Substituting $q_1 \approx 0$ and $q_2 \approx Q - h_f V\varepsilon$ into Equations (7.5.2) and (7.5.3) yields

$$m_3 \approx \frac{6\bar{\mu}V}{H^2} \quad (7.5.10)$$

$$m_4 \approx \frac{-6\bar{\mu}\left[VH - 2(Q - h_f V\varepsilon)\right]}{H^3} \quad (7.5.11)$$

Substituting $x = L_2$ into Equation (7.5.9) gives the final penetration depth at the outlet of slot die, h_f

$$h_f^{(n+1)/n} = I(D + Eh_f)^{1/n} \cdot (F + Gh_f) \quad (7.5.12)$$

where

$D = -\frac{6\bar{\mu}V}{H^2} + \frac{12\bar{\mu}Q}{H^3}$, $E = -\frac{12\bar{\mu}V\varepsilon}{H^3}$, $F = 1 + \frac{D}{m_3}$, $G = \frac{E}{m_3}$, $I = \left(\frac{k}{\mu_{eff}}\right)^{1/n} \frac{1}{V\varepsilon} L_2^{(n+1)/n}$, and $m_3 \approx \frac{6\bar{\mu}V}{H^2}$.

Equation (7.5.12) is an implicit analytical expression that can be used to evaluate the final penetration depth for slot-die coating a non-Newtonian fluid on a porous media.

As expected, when n = 1, Equation (7.5.12) will generate the same result as Equation (7.3.15) for a Newtonian fluid.

7.6 Determination of the physically correct penetration depth for the implicit model

Equation (7.5.12) derived using macro-scale model (Darcy's law) is only an approximation for the overall penetration depth. It cannot provide precise information of the penetration depth distribution on the micro-scale level in the porous media. In addition, several approximations and simplifications have been introduced in the previous derivations. Equation (7.5.12) unavoidably includes errors. Therefore, it is unnecessary to find precise roots for Equation (7.5.12) but rather approximations. An easy way for solving Equation (7.5.12) is treating the left side and right side of the equation as two separate curves. Plotting these two curves and finding the intersection points, thus giving the roots of Equation (7.5.12). This procedure can be done using standard math tools, such as Matlab.

It has to be noticed that several mathematical roots exist for Equation (7.5.12), but only one of them will be physically correct. For this complex expression, it is very hard to use a procedure like Section 7.4 to analytically determine the physically correct root. All mathematical roots from Equation (7.5.12) must be checked separately to determine which one is physically correct. Following constraints are imposed to find the physically correct root in current study:

(1) h_f must be a positive real number, i.e., $h_f > 0$.

(2) The absolute value of pressure gradient m_4 (Equation (7.5.11)) calculated based on the value of h_f must be positive, i.e., $m_4 > 0$.

(3) Penetration flow rate $h_f V\varepsilon$ must be smaller than the total flow rate Q, i.e., $h_f V\varepsilon < Q$.

It is possible that none of mathematical roots of Equation (7.5.12) is physically correct. This result occurs when the coating conditions used for the calculation are physically unreasonable. For example, the coating speed V cannot be set to infinity or zero. In order to make sure a physically correct root always exist, the conditions used for calculation must be in the region of coating window. The coating window is another complex issue and will be discussed in Chapter 8.

7.7 Analytical penetration depth for Newtonian fluids with a positive capillary pressure

In this section, a positive capillary pressure (hydrophilic or contact angle < 90°) is assumed to exist for the two phase flow in the porous media. Analytical penetration depth for coating Newtonian fluids with a positive capillary pressure is derived. Nomenclature found in Fig 5-1 and Figure 7.3 is used during the derivation.

As shown in the Figure 7.3(c), the penetration process is governed by the pressure in the coating bead, $p(x)$, and the capillary pressure in the porous media, p_c. Capillary pressure is defined as $p_c = p_{non-wetting} - p_{wetting}$. In the current study, air is the non-wetting phase, penetrated liquid is the wetting phase. Thus, $p_c = p_{air} - p_{liquid}$, where p_{air} is the reference pressure which is defined as zero. Therefore, $p_{liquid} = -p_c$, where p_{liquid} is the pressure at the front of penetrated fluid (Figure 7.3(c)). $p(x) - p_{liquid} = p(x) + p_c$ is the overall driving pressure for penetration. When the capillary pressure is positive it increases the pressure difference between the coating bead and the penetrated fluid front,

i.e. $p(x)+p_c$ is higher than $p(x)$. Therefore, the positive capillary pressure is expected to increase the fluid penetration since the penetration velocity will increase.

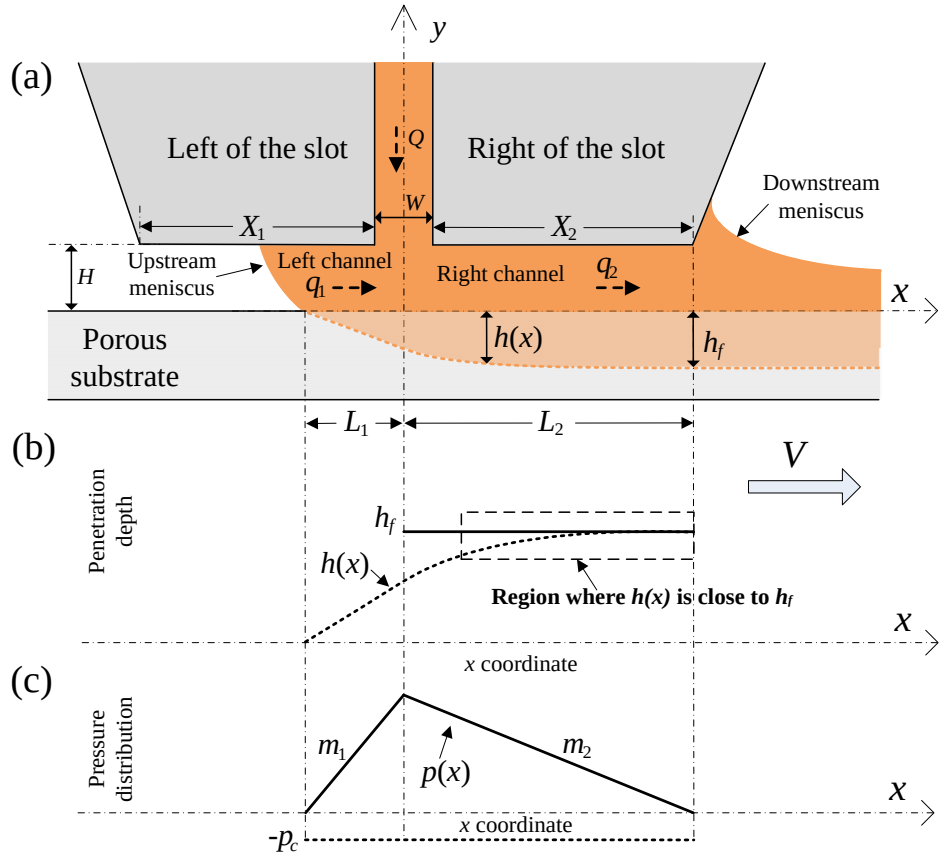

Figure 7.3 Schematic of a) the slot die configuration and b) analytical penetration depth and c) pressure distribution with a positive capillary pressure

Applying Darcy's law, the penetration velocity, $v_p(x)$, along the porous media is given by

$$v_p(x)=\frac{k}{\mu\varepsilon}\frac{dp}{dy}=\frac{k}{\mu\varepsilon}\frac{p(x)+p_c}{h(x)} \tag{7.7.1}$$

In this section, a similar approach to that used for Newtonian fluids without capillary pressure (Section 7.3) is taken. However, Equation (7.3.1) is replaced by

Equation (7.7.1). The remaining derivation procedure and assumptions are the same as those in Section 7.3.

As discussed in Section 7.3, $v_p(x)$ can also be given by the Equation (7.3.2). Substituting Equation (7.3.2) into Equation (7.7.1) yields

$$h(x)\cdot d\left[h(x)\right]=\frac{k}{\mu V\varepsilon}\left[p(x)+p_c\right]\cdot dx \tag{7.7.2}$$

As discussed in Section 7.3, the pressure distribution, $p(x)$, in the left channel and right channel for coating a Newtonian fluid can be, respectively, given by Equation (7.3.6) and (7.3.7). Substituting Equation (7.3.6) into Equation (7.7.2) and integrating from $x = -L_1$ to 0 gives the expression of penetration depth at $x = 0$, h_0 as

$$h_o=\sqrt{\frac{kL_1}{\mu V\varepsilon}\left[m_1L_1+2p_c\right]} \tag{7.7.3}$$

Substituting Equation (7.3.7) into Equation (7.7.2), integrating from $x = 0$ to L_2, and using the relation, $L_1=\frac{m_2L_2}{m_1}$, gives the expression of final penetration depth at $x = L_2$, h_f as

$$h_f=\sqrt{\frac{k}{\mu V\varepsilon}\left[m_2{L_2}^2+\frac{{m_2}^2{L_2}^2}{m_1}+2p_cL_2+2p_c\frac{m_2L_2}{m_1}\right]} \tag{7.7.4}$$

m_1 and m_2 in Equation (7.7.4) are still unknown. As discussed in Section 7.3, m_1 and m_2 can be approximated by Equations (7.3.12) and (7.3.13). Substituting Equation (7.3.12) into Equation (7.7.4) and solving Equations (7.7.4) and (7.3.13) gives an quadratic function for h_f

$$A\cdot{h_f}^2+B_c\cdot h_f+C_c=0 \tag{7.7.5}$$

Mathematically, there are two roots of h_f. However, it can be demonstrated using the procedure introduced in Section 7.4 that only one of them is physically correct, which is given by

$$h_f = \frac{-B_c - \sqrt{B_c^{\,2} - 4AC_c}}{2A} \tag{7.7.6}$$

where

$A = \frac{24kL_2^{\,2}\varepsilon}{H^4} - 1$, $B_c = \frac{12kL_2^{\,2}}{H^4 V}\left(VH - 4Q - \frac{p_c H^3}{3\mu L_2}\right)$, and

$C_c = \frac{6k(2Q - VH)}{H^4 V^2 \varepsilon}\left(2QL_2^{\,2} + \frac{P_c L_2 H^3}{3\mu}\right) + \frac{2kp_c L_2}{\mu V \varepsilon}$

Equation (7.7.6) is an explicit expression that can be used to calculate the final penetration depth of a Newtonian fluid slot-die coated onto a porous substrate, taking into account the effect of a capillary force that absorbs the fluid into the porous substrate. As expected, when $p_c = 0$, Equation (7.7.6) will generate the same result as Equation (7.3.15).

7.8 Analytical penetration depth for coating Newtonian fluids with a negative capillary pressure

In this section, a negative capillary pressure (hydrophobic or contact angle > 90°) is assumed to exist for the two phase flow in the porous media. Analytical penetration depth for coating Newtonian fluids with a negative capillary pressure is derived. Nomenclature found in Fig. 5-1 and Figure 7.4 is used during the derivation.

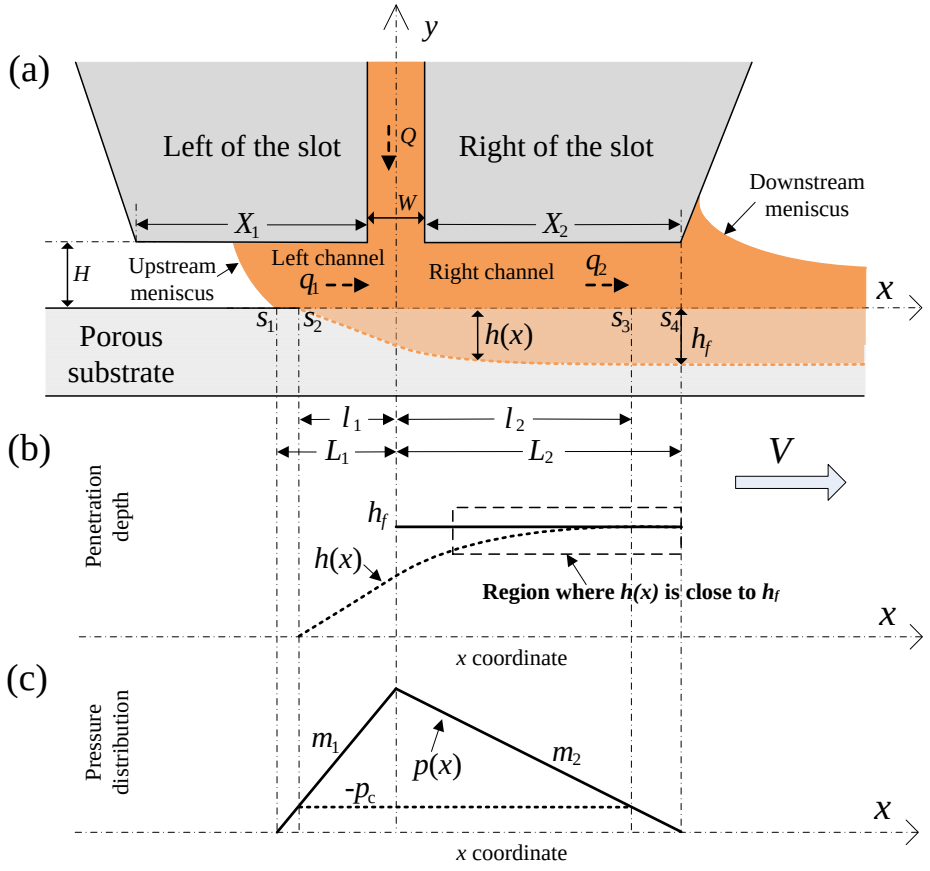

Figure 7.4 Schematic of a) the slot die configuration and b) analytical penetration depth and c) pressure distribution with a negative capillary pressure

As shown in the Figure 7.4(c), the penetration process is governed by the pressure in the coating bead, $p(x)$, and the capillary pressure in the porous media, p_c. As discussed in Section 7.7, $p_{liquid} = -p_c$ is the pressure at the front of the penetrated fluid (Figure 7.4(c)), and $p(x) - p_{liquid} = p(x) + p_c$ is the overall driving pressure for penetration. When the capillary pressure is negative it decreases the pressure difference between the coating bead and the penetrated fluid front, i.e. $p(x) + p_c$ is lower than $p(x)$. Therefore, the negative capillary pressure is expected to decrease the fluid penetration since penetration velocity will decrease.

As shown in Figure 7.4, from the position of dynamic contact line, s_1, to the position, s_2, the pressure in the coating bead, $p(x)$, is smaller than the capillary pressure (absolute value), $-p_c$. Thus, there is no penetration from s_1 to s_2, i.e., the penetration starts from s_2. The penetration depth gradually increases from s_2 to s_3. From s_3 to the outlet, s_4, the pressure in the coating bead is smaller than the capillary pressure (absolute value), $-p_c$. In this case, the penetration depth is expected to decrease from s_3 to s_4, i.e., the penetrated fluid will want to draw upward in y, and out of the porous media. However, the real dynamics is much more complex. The penetrated fluid does not necessarily decrease due to the effects of the receding contact angle and pinning behavior, which will be discussed in detail in Section 9.5. In this study, the penetration depth from s_3 to s_4 is approximately assumed to be constant. The derivation for the final penetration depth, h_f, with a negative capillary pressure will be limited in the region, s_2 to s_3. For this derivation, a similar approach used for the positive capillary pressure is taken.

Substituting Equation (7.3.6) into Equation (7.7.2) and integrating from $x = -l_1$ to 0 and using the relation, $l_1 = L_1 + \frac{p_c}{m_1}$, gives the expression of penetration depth at $x = 0$, h_o as

$$h_o = \sqrt{\frac{kL_1}{\mu V \varepsilon}\left[m_1 L_1^{\,2} + 2 p_c L_1 + \frac{p_c^{\,2}}{m_1} \right]} \tag{7.8.1}$$

Substituting Equation (7.3.7) into Equation (7.7.2), integrating from $x = 0$ to l_2, and using the relations, $L_1 = \frac{m_2 L_2}{m_1}$ and $l_2 = L_2 + \frac{p_c}{m_2}$, gives the expression of final penetration depth at $x = l_2$, h_f as

$$h_f = \sqrt{\frac{k}{\mu V \varepsilon}\left[\frac{m_2^{\,2} L_2^{\,2}}{m_1} + m_2 L_2^{\,2} + 2p_c\left(\frac{m_2}{m_1}+1\right)L_2 + \left(\frac{1}{m_1}+\frac{1}{m_2}\right)p_c^{\,2}\right]} \tag{7.8.2}$$

where m_1 and m_2 are given by Equations (7.3.12) and (7.3.13).

Equation (7.8.2) is an implicit analytical expression of the final penetration depth because m_2 is a function of h_f. As expected, when $p_c = 0$, Equation (7.8.2) will generate the same result as Equation (7.3.15). Several roots may exist for Equation (7.8.2). The physically correct root of Equation (7.8.2) can be determined using the method introduced in Section 7.6. However, it has to be mentioned that when the coating speed is too high the overall pressure in the coating bead, $p(x)$, might be smaller than the capillary pressure (absolute value), $-p_c$. In this case, the physical penetration depth will be zero, i.e., no penetration occurs. This phenomenon will be explained in detail, in Section 8.5.

7.9 Analytical penetration depth for coating non-Newtonian fluids with a positive capillary pressure

In this section, analytical penetration depth for coating non-Newtonian fluids with a positive capillary pressure is derived. For this derivation, a similar approach used for Newtonian fluids is taken (Section 7.7). Nomenclature found in Fig. 5-1 and Figure 7.3 is used during the derivation.

When coating a non-Newtonian fluid, the 1-D modified Blake-Kozeny equation is used, which is given by

$$v_p = \left[\frac{k}{\mu_{eff}}\frac{p(x)+p_c}{h(x)}\right]^{1/n}\frac{1}{\varepsilon} \tag{7.9.1}$$

Equation (7.7.1) is replaced by Equation (7.9.1). The remaining derivation procedure and assumptions are the same as those in Section 7.7. Substituting Equation (7.3.2) into Equation (7.9.1) yields

$$\left[h(x)\right]^{1/n} \cdot d\left[h(x)\right] = \left[\frac{k \cdot \left(p(x) + p_c\right)}{\mu_{eff}}\right]^{1/n} \frac{1}{V\varepsilon} \cdot dx \tag{7.9.2}$$

As discussed in Section 7.5, the pressure distribution, $p(x)$, in the left channel and right channel for coating a non-Newtonian fluid can be, respectively, given by Equation (7.5.5) and (7.5.6). Substituting Equation (7.5.5) into Equation (7.9.2) and integrating from $x = -L_1$ to 0 gives the expression of penetration depth at $x = 0$, h_0 as

$$h_0^{(n+1)/n} = \left(\frac{k}{\mu_{eff}}\right)^{1/n} \frac{1}{V\varepsilon m_3}\left[\left(m_3 L_1 + p_c\right)^{(n+1)/n} - p_c^{(n+1)/n}\right] \tag{7.9.3}$$

Substituting Equation (7.5.6) into Equation (7.9.2), integrating from $x = 0$ to L_2, and using the relation, $L_1 = \frac{m_4 L_2}{m_3}$, gives the expression of final penetration depth at $x = L_2$, h_f as

$$h_f^{(n+1)/n} = \left(\frac{k}{\mu_{eff}}\right)^{1/n} \frac{1}{V\varepsilon}\left(\frac{1}{m_3} + \frac{1}{m_4}\right)\left[\left(m_4 L_2 + p_c\right)^{(n+1)/n} - p_c^{(n+1)/n}\right] \tag{7.9.4}$$

where m_3 and m_4 are given by Equations (7.5.10) and (7.5.11).

Equation (7.9.4) is an implicit analytical expression of the final penetration depth because m_4 is a function of h_f. As expected, when $p_c = 0$, Equation (7.9.4) will generate the same result as Equation (7.5.12). Several roots may exist for Equation (7.9.4). The physically correct root of Equation (7.9.4) can be determined using the method introduced in Section 7.6.

7.10 Analytical penetration depth for coating non-Newtonian fluids with a negative capillary pressure

In this section, an analytical expression for the penetration depth of coating non-Newtonian fluids with a negative capillary pressure is derived. For this derivation, a similar approach used for Newtonian fluids is taken (Section 7.8). Nomenclature found in Figure 5.1 and Figure 7.4 is used during the derivation.

Substituting Equation (7.5.5) into Equation (7.9.2) and integrating from $x = -l_1$ to 0 and using the relation, $l_1 = L_1 + \frac{p_c}{m_3}$, gives the expression of penetration depth at $x = 0$, h_o as

$$h_0^{(n+1)/n} = \left(\frac{k}{\mu_{eff}}\right)^{1/n} \frac{1}{V\varepsilon m_3}\left[\left(m_3 L_1 + p_c\right)^{(n+1)/n}\right] \tag{7.10.1}$$

Substituting Equation (7.5.6) into Equation (7.9.2), integrating from $x = 0$ to l_2, and using the relations, $L_1 = \frac{m_4 L_2}{m_3}$ and $l_2 = L_2 + \frac{p_c}{m_4}$, gives the expression of final penetration depth at $x = l_2$, h_f as

$$h_f^{(n+1)/n} = \left(\frac{k}{\mu_{eff}}\right)^{1/n} \frac{1}{V\varepsilon}\left(\frac{1}{m_3} + \frac{1}{m_4}\right)\left(m_4 L_2 + p_c\right)^{(n+1)/n} \tag{7.10.2}$$

where m_3 and m_4 are given by Equations (7.5.10) and (7.5.11).

Equation (7.10.2) is an implicit analytical expression of the final penetration depth because m_4 is a function of h_f. As expected, when $p_c = 0$, Equation (7.10.2) will generate the same result as Equation (7.5.12). Several roots may exist for Equation (7.10.2). The physically correct root of Equation (7.10.2) can be determined using the method introduced in Section 7.6. However, it has to be mentioned that when the coating

speed is too high the overall pressure in the coating bead, $p(x)$, might be smaller than the capillary pressure (absolute value), $-p_c$. In this case, the physical penetration depth is zero, i.e., no penetration occurs. This phenomenon will be explained in detail in Section 8.5.

CHAPTER 8. MODELING OF COATING WINDOW

8.1 Introduction

As discussed in Section 7.6, in order to get the physically reasonable penetration depth, the calculation of penetration depth using analytical models developed in Chapter 7 have to be conducted using physically reasonable coating conditions that ideally lie within the coating window. Therefore, it is necessary to know the position of the coating window boundaries before calculating the penetration depth. In this chapter, several models of coating window boundaries are developed based on analytical derivation and CFD simulation.

8.1.1 Coating window and coating defects

Based on Chu et al.'s work [104], a typical coating window for slot die coating on a solid substrate is schematically shown in Figure 8.1, which includes three boundaries: dripping boundary, air entrainment boundary and break line boundary. The coating has to be conducted in the region surrounded by these three boundaries. Otherwise, coating defects will occur. For example, as shown in Figure 8.1, when the flow rate is fixed at Q_1, the coating speed, V, must be between V_l and V_h to get a defect-free coating. The schematic of a defect-free coating is shown in Figure 8.2. For a defect-free coating, the width of the coated film is approximately the same as the width of the slot die, and the thickness of the coated film is uniform, as shown in Figure 8.2(c). Based on Chu et al.'s work [104], if the coating speed is lower than V_l, dripping will occur. If coating speed is higher than V_h, air entrainment will occur. V_b is the maximum possible speed of the

coating process. If coating speed is higher than V_b, break lines will occur and a defect-free coating cannot be obtained.

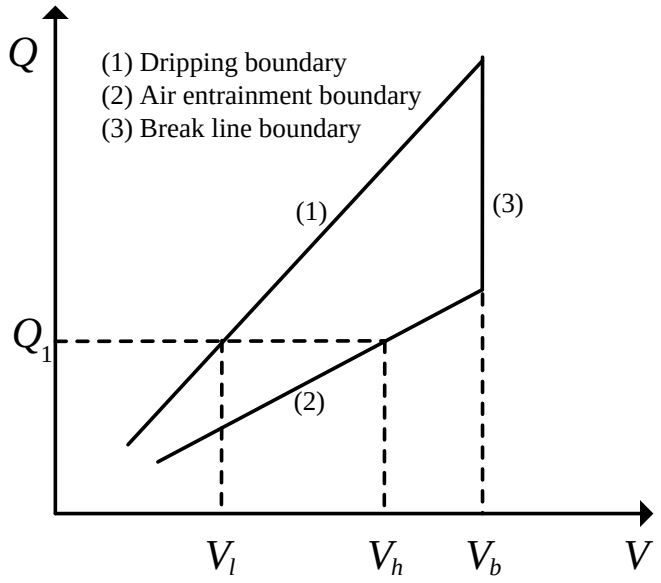

Figure 8.1 Schematic of a typical coating window (re-plotted based on reference [104])

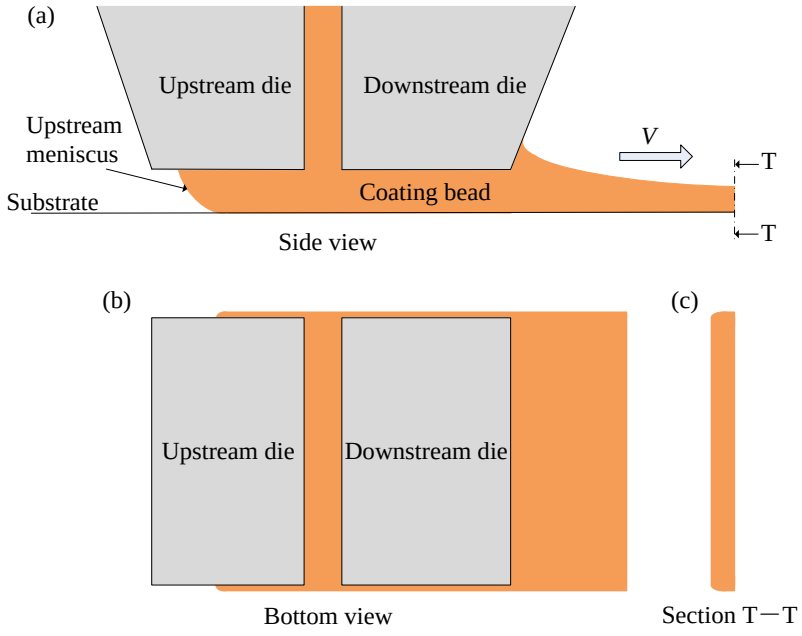

Figure 8.2 Schematic of a defect-free coating. a) side view, b) bottom view, c) cross-section view of the coated film

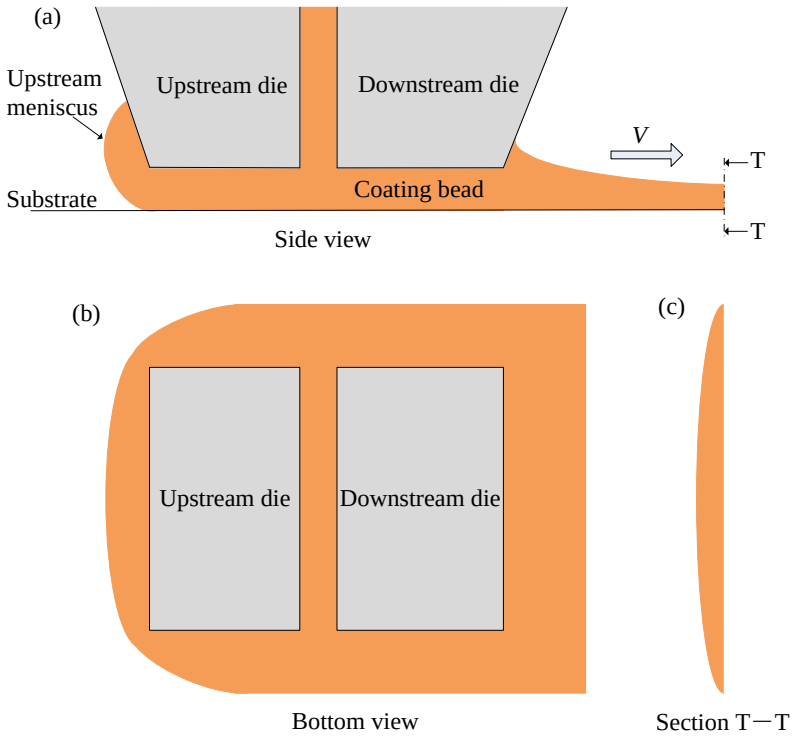

Figure 8.3 Schematic of coating with dripping. a) side view, b) bottom view, c) cross-section view of the coated film

Dripping: Dripping occurs when the coating speed is too low or the flow rate is too high and the upstream meniscus of the coating bead moves out of the slot die. In this case, the cast solution collects behind the upstream die, as shown in Figure 8.3(a). In Chu et al's work [104], a circular roller was used as the substrate, therefore the accumulated solution behind the upstream die drips down along the roller. However, the substrate below the slot die is a long and flat PET film, in this work. Therefore, real dripping does not occur; instead, the accumulated solution usually spreads bilaterally out of the slot die, as shown in Figure 8.3(b). This condition may also be called a spreading defect. However, the names of dripping and dripping boundary are used in this study for convenience. In the case of dripping, the width and thickness of the film can no longer be controlled, as shown in Figure 8.3(c).

Air Entrainment: For a fixed flow rate, air entrainment occurs when the coating speed is so high that surrounding air gets sucked into the liquid film [104]. Chu et al. [104] observed that the upstream dynamic contact angle (Figure 8.4 (a)) approaches 180° and air bubbles get entrained into the film when the coating speed reaches a critical maximum value. Air bubbles are usually referred as air entrainment when discussing coating defects [62].

As shown in Figure 8.1, V_h on the air entrainment boundary represents the maximum coating speed for the fixed flow rate Q_1. Since the wet thickness of a coated film, t, is calculated by $t = \frac{Q}{V}$, the coating speed V_h corresponds to the minimum wet thickness for the flow rate Q_1. Therefore, the air entrainment boundary shown in Figure 8.1 can also be referred as the minimum wet thickness boundary. Another coating defect related to the air entrainment boundary is ribbing, which looks like regular waves on the film surface [62]. Chang et al. [105] found that either air bubbles or ribbing could occur at the air entrainment boundary, depending on the magnitude of the upstream dynamic contact angle. Specifically, when the upstream dynamic contact angle is smaller than 90°, ribbing will occur; whereas when the upstream dynamic contact angle is close to 180°, air bubbles will occur. In this study, air entrainment and the air entrainment boundary are used for convenience, no matter whether the real defect is air bubbles or ribbing. It has been found that the air entrainment usually occurs when the upstream dynamic contact line shifts to the centerline of the slot gap [64, 105, 106]. A schematic illustration of air entrainment during slot coating is given in Figure 8.4. It should be mentioned that the air entrainment boundary shown in Figure 8.1 is a straight line, whereas the actual form might be more complex as discussed in the following Section 8.1.3.

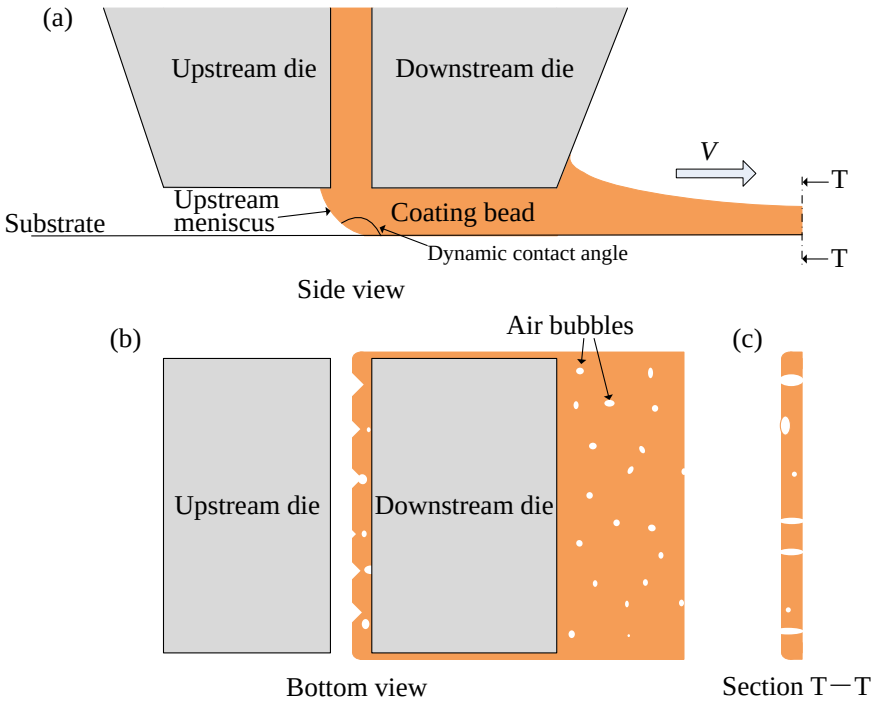

Figure 8.4 Schematic of coating with air entrainment. a) side view, b) bottom view, c) cross-section view of the coated film

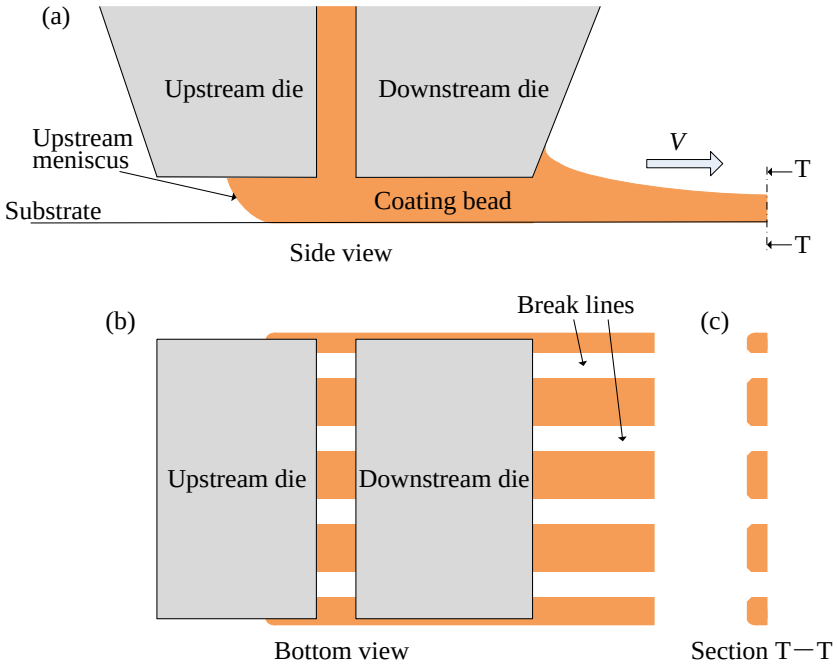

Figure 8.5 Schematic of coating with break lines. a) side view, b) bottom view, c) cross-section view of the coated film

Break line boundary: Generally, both V_l and V_h in Figure 8.1 increase with Q. However, the coating speed cannot increase to infinity. There is an upper boundary of the coating speed, V_b, which corresponds to the break line boundary in Figure 8.1. When the coating speed is higher than V_b, break lines usually occur and a complete film can no longer be obtained [104]. Schematic illustrating break lines during slot coating are shown in Figure 8.5(b) and (c). In addition, experimental results have shown that the break line boundary is usually a vertical line [62, 104, 107], as shown in Figure 8.1.

8.1.2 Previous study of coating window

A lot of work has been done to understand the characteristics of a coating window for slot die coating. Ning et al. [62], Yang et al. [108] and Chu et al. [104, 107] experimentally studied the effect of polymer and inorganic additives on the coating window and the minimum wet thickness. Yu and Liu [109], and Lu et al. [45] measured the coating window for a double layer slot die coating. Lin et al. [44] measured the minimum wet thickness for a slide-slot coating. Chang et al. [106] compared the coating window of vertical and horizontal slot die coatings. Bhamidipati et al. [64] numerically and experimentally studied the coating window for a relatively high-viscosity, shear thinning solution. Lee et al. [110] used a viscocapillary model to find the coating window and frequency response for slot die coating. Nam and Carvalho [111] numerically studied the coating window for a two-layer tensioned-web-over-slot die coating. Romero et al. [43, 112] numerically and experimentally examined the low-flow limit of slot coating of various liquids.

Most of previous work was based on experiments or simulation, only very limited analytical work has been conducted to study the coating window. Ruschak [113] first proposed an analytical model to find a coating window using Landau-Levich [114] film

coating theory. In Ruschak's model the viscous effect is ignored, thus the capillary pressure alone sets the bounds on coating bead operability. Later, Higgins and Scriven [115] extended Ruschak's work and included viscous effect in their models to determine the coating bounds. The accuracy of Ruschak [113], Higgins and Scriven's [115] models has been experimentally demonstrated by Lee et al [63]. However, Ruschak [113], Higgins and Scriven's [115] work is only limited to Newtonian fluids and cannot explicitly explain the break line boundary in Figure 8.1. In addition, all of previous work is limited to solid substrates. To the best knowledge of the author, the coating window on porous substrates has not been studied.

In this study, a series of analytical models for the dripping boundary and air entrainment boundary are developed for both Newtonian and non-Newtonian fluids and for both solid and porous substrates. In addition, the position of the break line boundary is studied using a CFD model built in commercial software, ANSYS-Fluent 14.5. Based on the simulation results and dimensional analysis, a model of the break line boundary is developed.

8.1.3 Three regions of slot die coating

Before developing analytical models, different regions regarding the coating window have to be discussed. Lee et al. [63] experimentally studied the effect of capillary number on the minimum coating thickness. Based on their experimental results, there exist two coating regions depending on the magnitude of the capillary number. In the first region where the capillary number is relatively small, the minimum coating thickness increases with capillary number. When the capillary number is high enough, the coating gets into the second region, in which the minimum coating thickness does not change

with capillary number. Later, Chang et al. [105] extended Lee et al.'s [63] work and found that there exists a third region for even higher capillary number, in which the minimum coating thickness decreases with the capillary number. Based on Lee et al. [63] and Chang et al.'s [105] work, the three regions of slot die coating are schematically shown in Figure 8.6(a). Figure 8.6(a) shows the relationship between the minimum wet thickness, t_{min}, and the capillary number, *Ca*, for three coating regions. Since the wet thickness of a coated film, *t*, is calculated by $t = \frac{Q}{V}$, the curve in Figure 8.6(a) could be translated into the a relationship between *Q* and *V*, as shown in Figure 8.6(b) where the slope of the curve equals the wet thickness. It can be seen that the slope of the curve in Figure 8.6(b) increases in the Region **1** and be a constant in the Region **2** and decreases in the Region **3**. This is equivalent to the trend observed in Figure 8.6(a). In addition, the curve in Figure 8.6(b) is the air entrainment boundary of a coating window because it corresponds to the minimum wet thickness.

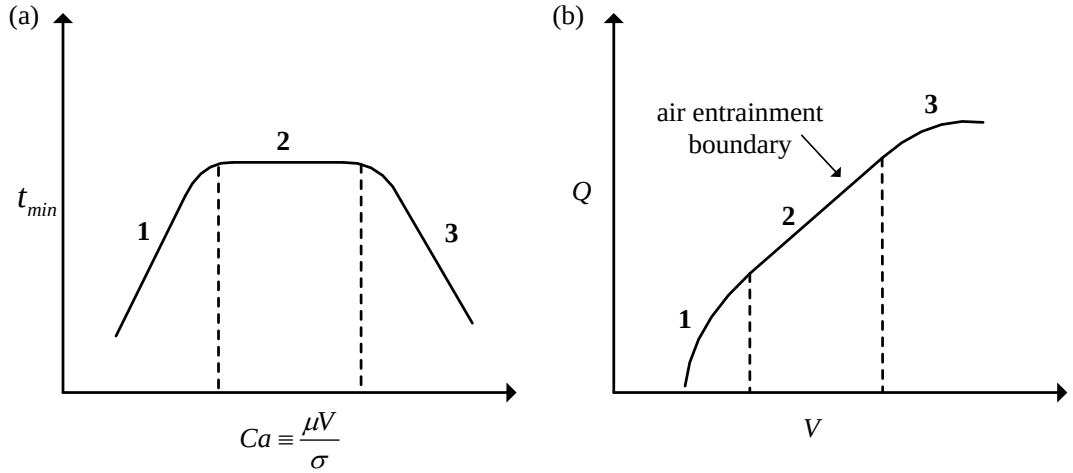

Figure 8.6 Three coating regions of slot die coating. a) relationship between t_{min} and *Ca* (re-plotted from reference [105]), b) air entrainment boundary

Based on previous work [63, 105, 115], the difference among these three coating regions is summarized as follows. In Region **1** of the air entrainment boundary, the capillary force of upstream and downstream menisci is significant, and the height of the downstream meniscus is relatively high, as shown in Figure 8.7(a). In Region **2** of the air entrainment boundary, the capillary force of upstream and downstream menisci is insignificant, thus the viscous force in the coating bead dominate. In this case, the height of the downstream meniscus is relatively low, as shown in Figure 8.7(b). From previous experimental results [105, 106], it was found that the upstream meniscus for both Region **1** and **2**, on the air entrainment boundary, is usually just below the center slot of the die, as shown in Figure 8.7(a) and (b). In Region **3** of the air entrainment boundary, the downstream meniscus is withdrawn into the downstream die lip region, and the upstream meniscus is at a certain point of the upstream die lip region, as shown in Figure 8.7(c). It has to be mentioned that an air entrainment boundary does not necessarily include all three regions, i.e., three coating regions do not necessarily exist together. For example, Lee et al. [63] reported the existence of Region **1** and **2**. Chang et al. [105] reported the existence of different regions for different conditions. The conditions causing the Region **3** are still not clear. However, from previous experimental results [105], it seems that Region **3** is only considerable for very low viscosity fluids. For example, lower than 5 mPa s, based on Chang et al.'s [105] experimental results.

8.1.4 Modeling assumption

During the derivation of analytical penetration depth models, it has been assumed that the capillary effect on the upstream and downstream menisci can be ignored (Assumption (3), Section 7.2). In this case, Region **1** of the air entrainment boundary will

be relatively insignificant. In addition, since this assumption is generally valid for relatively high viscosity liquids, Region **3** of the air entrainment boundary will be relatively insignificant too. Therefore, it is anticipated that Region **2** will dominate the entire air entrainment boundary. In this case, the air entrainment boundary is close to a straight line as shown in Figure 8.1. This is the basic assumption used for the following derivation of analytical coating window.

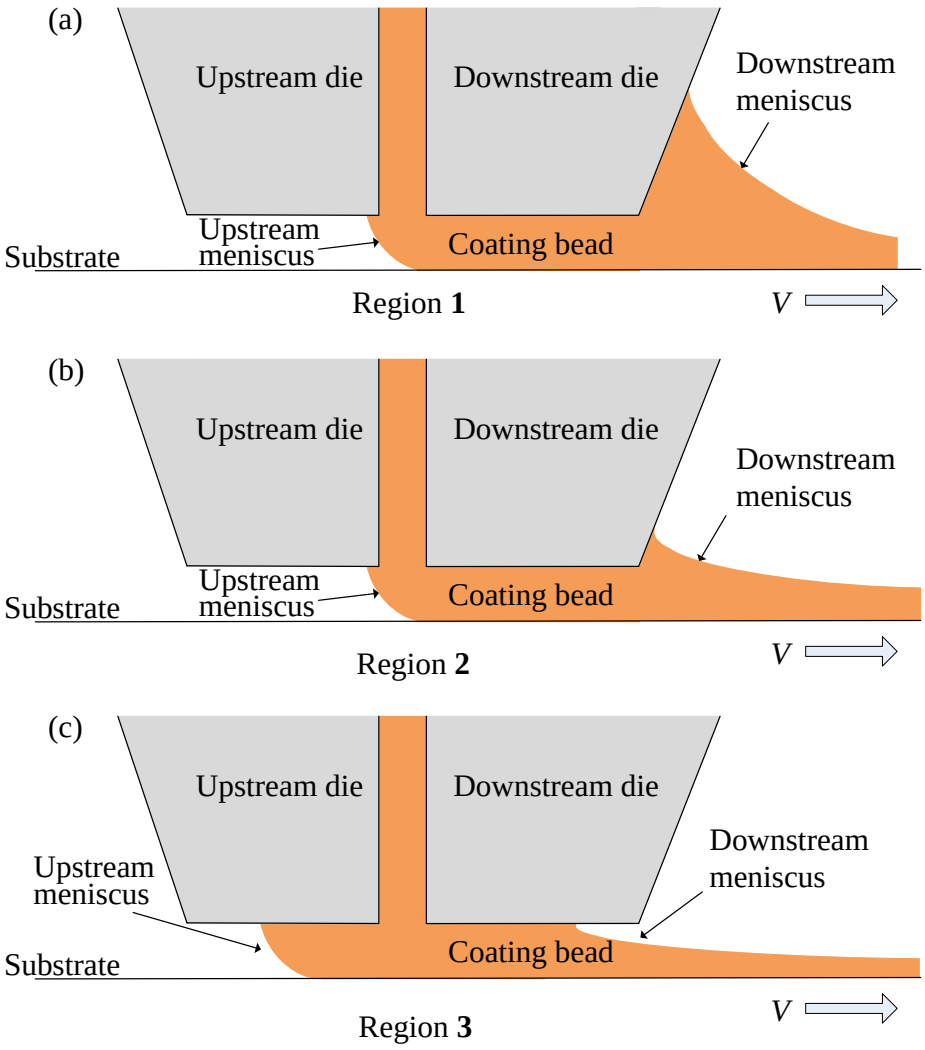

Figure 8.7 Difference of menisci of three coating regions.

8.2 Analytical models for dripping and air entrainment boundaries on a solid substrate

8.2.1 Models for coating Newtonian fluids on a solid substrate

Based on previous discussion, the dripping boundary and air entrainment boundary could be explained in the following way. Comparing Figure 8.3(a) with Figure 8.4(a), it can be seen that the position of the upstream meniscus moves from the left most edge of the upstream die to right most edge of the upstream die between the dripping boundary and air entrainment boundary. When the upstream meniscus moves to the right most edge of the upstream die, as shown in Figure 8.8, the top boundary of the upstream meniscus is pinned at the corner of the die and cannot move any further to the right. In this case, any further increase in the coating speed will cause an instability of the coating bead and lead to defects. As mentioned previously, the defects can either be air bubbles or ribbing depending on the magnitude of the dynamic contact angle on the substrate. Therefore, the upstream meniscus can approximately move between the left most of the upstream die and the center slot. The moving range of the upstream meniscus is shown in Figure 8.8. The corresponding coating speeds for these two limits are V_l and V_h, between which a defect-free coating is obtained.

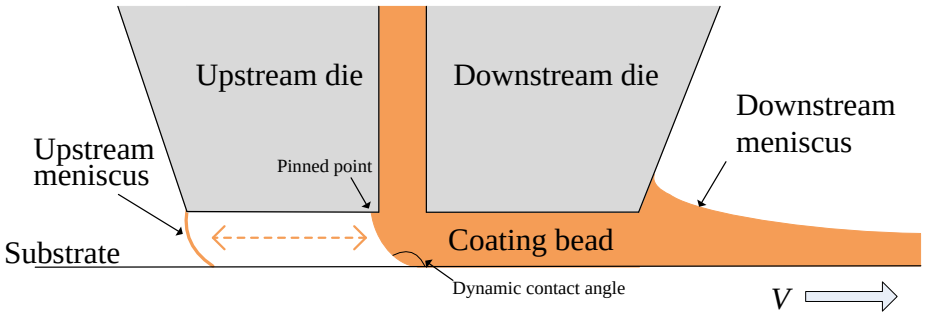

Figure 8.8 Moving range of the upstream meniscus

As discussed in Chapter 7, for slot-die coating, if the flow is laminar and the capillary effects on the upstream and downstream menisci are ignored, lubrication theory can be applied to the left channel and right channel, respectively, to determine the pressure distribution in the coating bead, as shown in Figure 8.9. The pressure gradients (absolute values) in these two channels, m_1 and m_2, are given by

$$m_1 = \frac{6\mu V}{H^2} \text{ (left channel)} \tag{8.2.1}$$

$$m_2 = \frac{-6\mu(VH - 2Q)}{H^3} \text{ (right channel)} \tag{8.2.2}$$

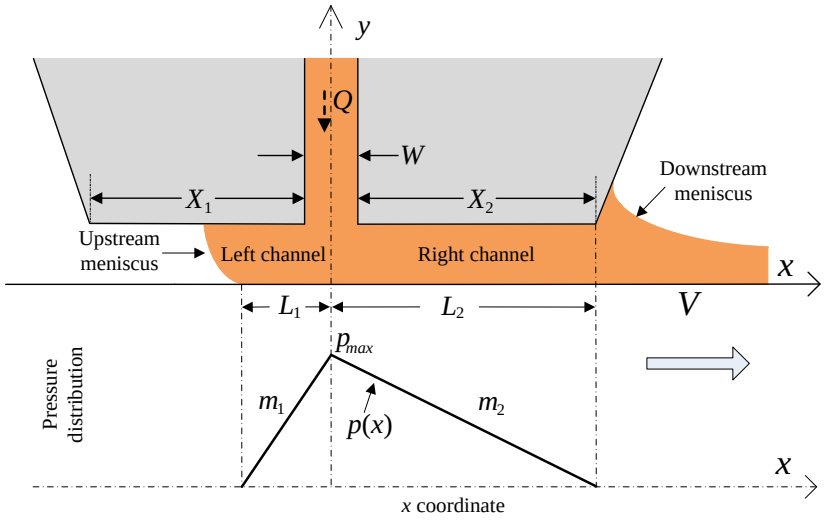

Figure 8.9 Pressure distribution for coating a solid substrate.

The maximum pressure at the center slot is

$$p_{max} = m_1 L_1 = m_2 L_2 \tag{8.2.3}$$

The position of the upstream meniscus L_1 (absolute value) is given by

$$L_1 = \frac{m_2 L_2}{m_1} \tag{8.2.4}$$

Since upstream meniscus can only move between the left most and right most of the upstream die, L_1 must be in the range

$$\frac{W}{2} \le L_1 \le X_1 + \frac{W}{2} \tag{8.2.5}$$

Substituting Equations (8.2.1), (8.2.2) and (8.2.4) into Equation (8.2.5) yields

$$\frac{2QL_2}{H\left(\frac{W}{2} + X_1 + L_2\right)} \le V \le \frac{2QL_2}{H\left(\frac{W}{2} + L_2\right)} \tag{8.2.6}$$

Equation (8.2.6) is the range of the coating speed between the dripping boundary and air entrainment boundary. Specifically, the left side of Equation (8.2.6) is the expression of the coating speed on the dripping boundary, V_l, given as

$$V_l = \frac{2QL_2}{H\left(\frac{W}{2} + X_1 + L_2\right)} \tag{8.2.7}$$

The right side of Equation (8.2.6) is the expression of the coating speed on the air entrainment boundary, V_h, given as

$$V_h = \frac{2QL_2}{H\left(\frac{W}{2} + L_2\right)} \tag{8.2.8}$$

It can be seen from Equations (8.2.7) and (8.2.8) that the dripping boundary and air entrainment boundary are only determined by the flow rate and geometry of the die. Viscosity or other fluid properties do not affect these two boundaries. The coating speed range bounded by Equation (8.2.6) has been derived previously by Higgins and Scriven [115]. However, Higgins and Scriven's work is limited to Newtonian fluids. In the following section, this discussion is extended to non-Newtonian fluids.

8.2.2 Models for coating non-Newtonian fluids on a solid substrate

As discussed in Chapter 7, when coating a non-Newtonian fluid, a generalized lubrication theory derived by Dien and Elrod [96] can be used to approximately calculate the absolute values of pressure gradients, which are given by

$$m_3 = \frac{6\bar{\mu}V}{H^2} \text{ (left channel)} \tag{8.2.9}$$

$$m_4 = \frac{-6\bar{\mu}(VH - 2Q)}{H^3} \text{ (right channel)} \tag{8.2.10}$$

where $\bar{\mu} \equiv mn\left(\frac{V}{H}\right)^{n-1}$.

Replacing Equations (8.2.1) and (8.2.2) by Equations (8.2.9) and (8.2.10), and following the same derivation procedure as those for a Newtonian fluid (Section 8.2.1), the same coating speed range indicated by Equation (8.2.6) can be obtained for a non-Newtonian fluid. Therefore, non-Newtonian fluids and Newtonian fluids have the same dripping boundary and air entrainment boundary, which are determined by the flow rate and geometry of the die. Viscosity or other fluid properties do not affect these two coating boundaries.

8.2.3 Analytical minimum wet thickness

The minimum wet thickness, t_{min}, which occurs on the air entrainment boundary, can be solved from Equation (8.2.8), after rearranging as shown by

$$t_{min} = \frac{Q}{V_h} = \frac{H\left(\frac{W}{2} + L_2\right)}{2L_2} \tag{8.2.11}$$

Usually L_2 is much larger than 0.5W [62-64, 104, 105, 108], thus $t_{\min}$ approximately equals to 0.5H. Due to the assumption of above modeling work (Section 8.1.4), Equation (8.2.11) is actually the minimum wet thickness of the Region **2** in Figure 8.6(a). From

Equation (8.2.11) it is evident that the minimum wet thickness in Region **2** is only determined by the geometry of the slot die, and is not affected by the viscosity or other fluid properties. Equation (8.2.11) is valid for both Newtonian and non-Newtonian fluids.

8.3 Experimental validation of analytical dripping and air entrainment boundaries

A direct demonstration of analytical air entrainment boundary is the value of minimum wet thickness in Region **2** which has been experimentally measured by many researchers. Based on previous work [62-64, 104, 105, 108], it has been experimentally found that the minimum wet thickness in Region **2** is generally between 0.5H to 0.7H for both Newtonian and non-Newtonian fluids, which is close to 0.5H given by Equation (8.2.11).

In order to further demonstrate the effectiveness of above analytical models, the analytically calculated dripping and air entrainment boundaries are directly compared with experimental and numerical results obtained by Bhamidipati et al. [64, 116]. In Bhamidipati et al.'s [64, 116] work, the dripping boundary and air entrainment boundary for slot die coating two kinds of Black strap molasses (pure and dilute), which are non-Newtonian onto a solid substrate, were experimentally measured and numerically calculated using a CFD model. Analytical, experimental and numerical results are compared with each other in Figure 8.10 and Figure 8.11 where the derived analytical boundaries for a non-Newtonian fluid, Equations (8.2.7) and (8.2.8), are used.

It can be seen from Figure 8.10 and Figure 8.11 that the analytically calculated dripping and air entrainment boundaries match well with the experimental and simulation results. The relative error between analytical and experimental results is generally lower than 5%. This can serve as evidence that the analytical models of dripping and air

entrainment boundaries for slot die coating on solid substrates derived in previous sections are accurate.

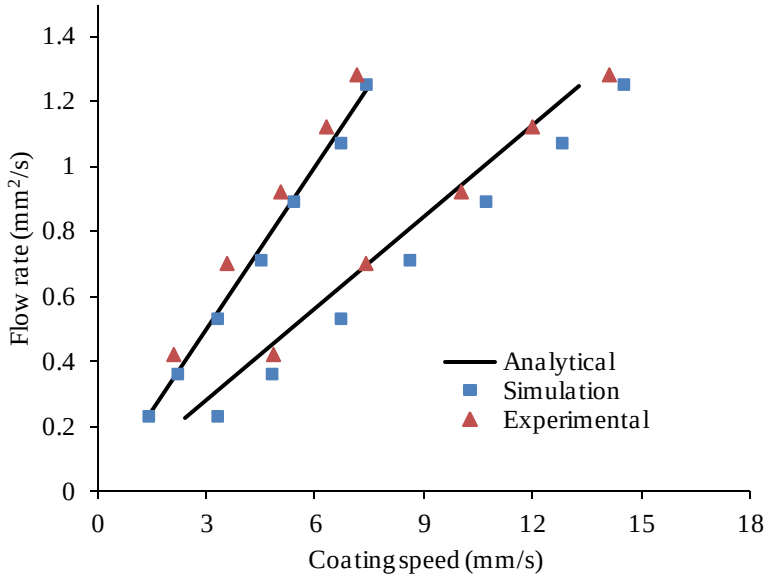

Figure 8.10 Comparison of analytical dripping and air entrainment boundaries with experimentally and numerically obtained coating boundaries for a kind of dilute black strap molasses [64, 116]. Geometrical conditions are W = 0.178 mm, H = 0.178 mm, X_1 = 1.3 mm, X_2 = 1.5 mm.

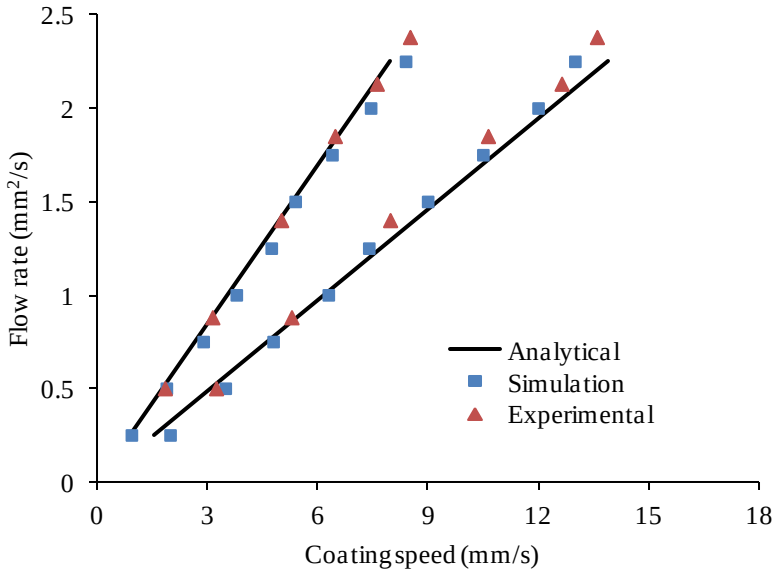

Figure 8.11 Comparison of analytical dripping and air entrainment boundaries with experimentally and numerically obtained coating boundaries for pure black strap molasses [64, 116]. Geometrical conditions are W = 0.25 mm, H = 0.3 mm, X_1 = 1.3 mm, X_2 = 1.5 mm.

8.4 Analytical models for dripping and air entrainment boundaries on a porous substrate

When coating on a porous substrate, the penetration will affect the pressure distribution in the coating bead. As discussed in Chapter 7, the pressure gradients (absolute values) in the left and right channels can be approximated by Equations (7.2.12) and (7.2.13), or Equations (7.4.10) and (7.4.11) for Newtonian and non-Newtonian fluids, respectively. Replacing Equations (8.2.1) and (8.2.2) by Equations (7.2.4) and (7.2.5), or Equations (7.4.10) and (7.4.11), and following the same derivation procedure in Section 8.2.1, the coating speed range can be obtained as

$$\frac{2QL_2}{H\left(\frac{W}{2}+X_1+L_2\right)+2h_fL_2\varepsilon} \le V \le \frac{2QL_2}{H\left(\frac{W}{2}+L_2\right)+2h_fL_2\varepsilon} \tag{8.4.1}$$

Specifically, the dripping boundary is

$$V_l = \frac{2QL_2}{H\left(\frac{W}{2}+X_1+L_2\right)+2h_fL_2\varepsilon} \tag{8.4.2}$$

The air entrainment boundary is

$$V_h = \frac{2QL_2}{H\left(\frac{W}{2}+L_2\right)+2h_fL_2\varepsilon} \tag{8.4.3}$$

In Equation (8.4.1), (8.4.2) and (8.4.3), h_f is the final penetration depth which can be calculated using models derived in Chapter 7. It has to be noticed that h_f is a function of coating speed V, so Equations (8.4.2) and (8.4.3) are implicit expressions of V_l and V_h. V_l and V_h can be determined using the following procedure:

(1) Calculate the coating speed boundaries using Equation (8.2.6) for a solid substrate. The dripping boundary, $V_{l\text{-}s}$, and air entrainment boundary, $V_{h\text{-}s}$, obtained from

Equation (8.2.6) for a solid substrate can be used as the first approximation for coating speed boundaries on a porous substrate.

(2) For a fixed flow rate Q, assume an initial value of dripping coating speed, $V_{l\text{-}p}$, on a porous substrate, and calculate the penetration depth h_f using the models in Chapter 7 based on the assumed $V_{l\text{-}p}$. Then substitute h_f into Equation (8.4.2) and calculate another value of $V_{l\text{-}p}$. If the calculated $V_{l\text{-}p}$ from Equation (8.4.2) is the same as (or close enough to) the initially assumed $V_{l\text{-}p}$, then that $V_{l\text{-}p}$ is the dripping boundary. Otherwise, assume another $V_{l\text{-}p}$ and repeat the above procedure until the calculated $V_{l\text{-}p}$ from Equation (8.4.2) is the same as (or close enough to) the assumed $V_{l\text{-}p}$. When assuming a dripping coating speed $V_{l\text{-}p}$, the value of $V_{l\text{-}s}$ can be used as the first approximation. It has to be mentioned that when calculating h_f using an assumed coating speed $V_{l\text{-}p}$, a physically correct h_f might not be able to solved. In that case, the assumed $V_{l\text{-}p}$ is out of the physically reasonable coating window, thus the assumption of $V_{l\text{-}p}$ must be adjusted.

(3) Follow the same procedure in step (2) to determine the air entrainment boundary.

It has to be declared that the dripping and air entrainment boundaries for coating porous media derived above are based on the assumption that the upstream meniscus can only move in the range of upstream die lip, as shown in Figure 8.8. This assumption is a direct analogy of coating a solid substrate. To the best of author's knowledge, the coating boundaries for coating a porous substrate has not been studied; thus no experimental data exist to directly demonstrate Equations (8.4.1), (8.4.2) and (8.4.3). However, these equations are believed to be able to give a first approximation for the coating boundaries of coating a porous substrate. Later in Chapter 10, these equations will be used to

determine the approximate coating boundaries in the experiments of measuring penetration depth when coating on porous carbon paper. L_1

8.5 Effect of penetration on coating window

Comparing Equation (8.4.1) with Equation (8.2.6), it can be seen that the coating speed on both dripping and air entrainment boundaries on a porous substrate is smaller than that on a solid substrate. This reduction is due to the effect of penetration. For comparison, the dripping and air entrainment boundaries on two kinds of substrates were calculated. Geometrical conditions and porous media properties in Section 6.5 were used for calculation. Specifically, geometry is shown in Figure 6.2, V = 3.5 mm/s, μ = 0.4 Pa-s, k = 9.375×10^{-13} m^2, ε = 0.75. The capillary pressure is assumed to be zero. The result is shown in Figure 8.12. It can be clearly seen that both dripping boundary and air entrainment boundary on the porous substrate shifts to lower coating speeds, compared with that on the solid substrate.

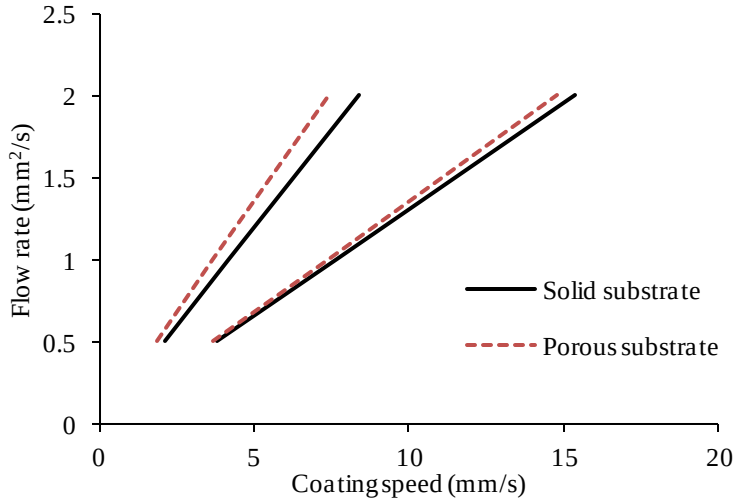

Figure 8.12 Effect of penetration on dripping and air entrainment boundaries

The reason of the shifting of coating boundaries could be explained by Figure 8.13. In Figure 8.13 the flow field of coating a porous substrate is compared with that of coating a solid substrate while keeping all other coating conditions the same. This calculation was conducted using the CFD model developed in Chapter 6. The following conditions were used in the calculation: $Q = 1\times10^{-6}$ m^2/s (2-D flow rate), $V = 13$ mm/s, $H = 100$ μm, $W = 100$ μm, $X_1 = 1.3$ mm, $X_2 = 1.5$ mm, $\mu = 0.4$ Pa s, $k = 8.99\times10^{-12}$ m^2, $\varepsilon = 0.75$, $p_c = 0$. From Figure 8.13, it can be seen that the upstream meniscus on the porous substrate is closer to the center slot compared with that on the solid substrate. The distance between these two upstream menisci is around 0.7~0.8 mm. This means a smaller coating speed must be used for the porous substrate to get the same position of the upstream meniscus as the solid substrate. This can explain why the coating boundaries on a porous substrate shift to lower coating speeds in Figure 8.12.

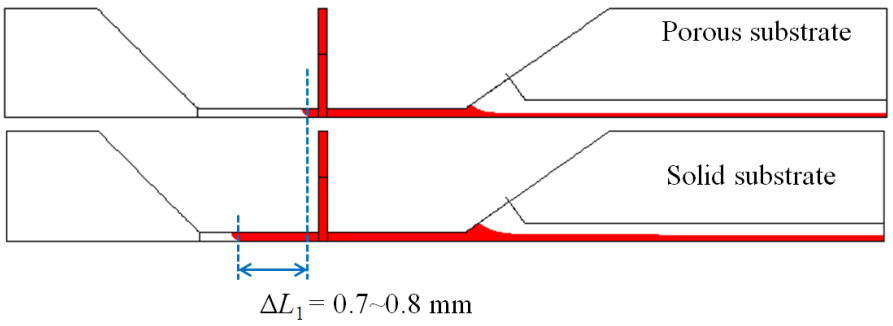

Figure 8.13 Effect of penetration on the position of upstream meniscus

In order to study the effect of penetration depth on coating boundaries, the dripping and air entrainment boundaries were calculated for different capillary pressure values. Specifically, the capillary pressure, p_c, was assumed to be –100 Pa, 0 Pa, and 100 Pa, respectively, to account for hydrophilic, hydrophobic and neutral wetting conditions. The flow rate, Q, was fixed at 1×10^{-6} m^2/s (2-D flow rate). Geometrical conditions and

porous media properties in Section 6.5 were used for calculation. Specifically, geometry is shown in Figure 6.2, V = 3.5 mm/s, μ = 0.4 Pa-s, k = 9.375×10^{-13} m^2, ε = 0.75. The results are summarized in Table 8-1. Using the analytical penetration depth models developed in Chapter 7, the change of penetration depth with coating speed within the coating boundary was also calculated. The results are shown in Figure 8.14.

Table 8-1 Coating boundaries for a solid substrate and a porous substrate with different capillary pressure values based on the analytical models

	Coating speed of dripping boundary (mm/s)	**Coating speed of air entrainment boundary (mm/s)**
Solid substrate	4.2	7.7
p_c = 0 Pa	3.7	7.4
p_c = -100 Pa	3.9	7.7
p_c = 100 Pa	3.6	6.5

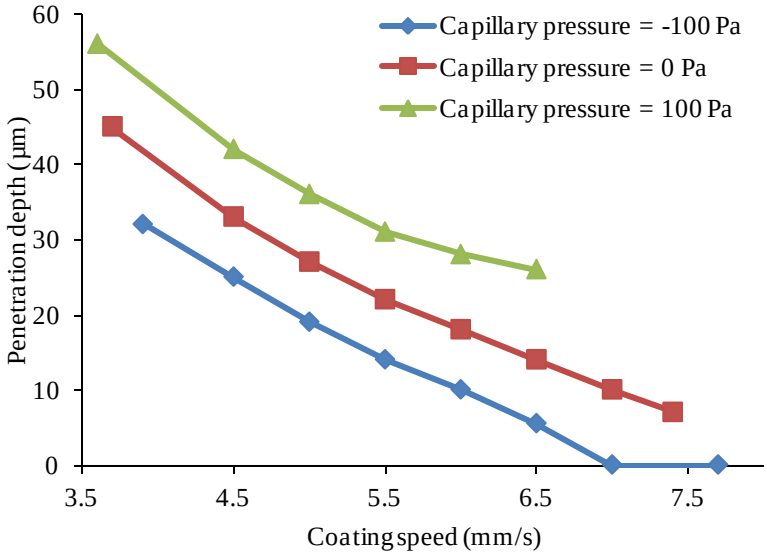

Figure 8.14 Change of penetration depth in the coating boundaries for different capillary pressure.

As discussed in Chapter 7, a positive capillary pressure (hydrophilic or contact angle < 90°) should increase the penetration depth; while a negative capillary pressure (hydrophobic or contact angle > 90°) should decrease the penetration depth. This effect can be clearly seen in Figure 8.14. It can also be seen from Table 8-1 and Figure 8.14 that higher penetration depth causes lower coating speed of both dripping boundary and air entrainment boundary. For example, the P_c = 100 Pa case has the lowest dripping boundary and air entrainment boundary compared with other two cases. The importance of this finding for the coating industry is that the production rate of coating a porous substrate might decrease with an increase in penetration depth.

Another interesting phenomenon can be found in Table 8-1 and Figure 8.14, namely that the air entrainment boundary for a porous substrate with a negative capillary pressure does not change compared with a solid substrate. Specifically, the air entrainment boundary for both the solid substrate and the negative capillary pressure cases is the same, 7.7 mm/s. From Figure 8.14, it can be seen that the penetration depth is zero, i.e., there is no penetration, for P_c = –100 Pa and coating speed is higher than 7 mm/s. This is because when the coating speed is higher than 7 mm/s, the pressure in the coating bead is smaller than the 100 Pa. In this case, the fluid cannot be pushed into the porous media, and no penetration can occur. Therefore, when the coating speed is high enough for a negative capillary pressure case, a porous substrate has similar characteristics to a solid substrate, and the air entrainment boundary does not change. This phenomenon has been mentioned previously in Section 7.10.

8.6 Modeling of break line boundary

As mentioned previous in Section 8.1.1, many experimental data have shown that the break line boundary is usually a vertical line [62, 104, 107], as shown in Figure 8.1. This means that the break line boundary corresponds to the maximum possible coating speed of the entire coating window, thus it directly determines the productivity of the coating process. However, in spite of its importance, the mechanisms that affect the break line boundary are not well understood. In this section, a model of the break line velocity, V_b, will be developed based on dimensional analysis and numerical study.

8.6.1 Break line boundary

As shown in Figure 8.15, Q_{bl} corresponds to the lowest flow rate on the break line boundary. Q_{bh} corresponds to the highest flow rate on the break line boundary. (V_b, Q_{bl}) is the intersection point between the air entrainment boundary and the break line boundary. (V_b, Q_{bh}) is the intersection point between the dripping boundary and break line boundary. Since the break line boundary is just between the air entrainment boundary and dripping boundary, the upstream meniscus will move from the center slot, i.e., the right most area of the upstream die, to the left most area of the upstream die, when the flow rate increases from Q_{bl} to Q_{bh} along the break line boundary. This is exactly the moving range of upstream meniscus indicated in Figure 8.8. Therefore, if a solution is coated along the break line boundary, the upstream meniscus can be at any position below the upstream die (Figure 8.8) depending on the magnitude of the flow rate. This is different with the dripping boundary for which the upstream meniscus is always at the left most of the upstream die, and the air entrainment boundary for which the upstream meniscus is always at the right most of the upstream die. The defect accompanying with the break line boundary is usually break lines [104], which is a collection of streaks on the substrate.

It has to be noticed that all defects on both break line boundary and air entrainment boundary, including break lines, air bubbles and ribbing, are indicators of an unstable coating bead [62, 104, 107].

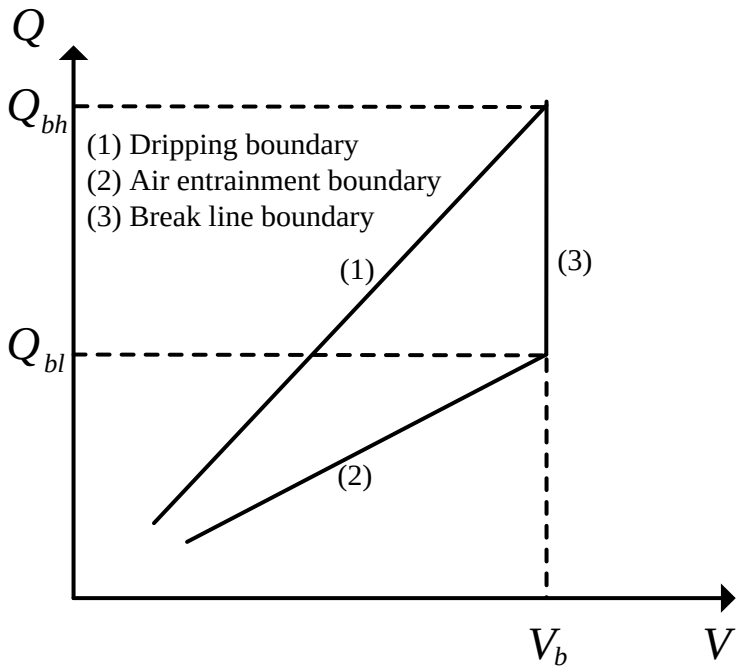

Figure 8.15 Flow rate range of break line boundary

8.6.2 Dimensional analysis

Dimensional analysis is conducted to determine all possible dimensionless combinations of variables that affect the break line velocity, V_b. Important parameters that may affect V_b include: fluid viscosity (μ), fluid surface tension (σ), fluid density (ρ), contact angle on the substrate (α), contact angle on the die (β), stand-off height (H), length of the right channel (L_2), and acceleration of gravity (g). In this study the break line is assumed to be vertical, thus V_b is not affected by Q. Using Buckingham pi

theorem, six dimensionless pi-terms are obtained: $\pi_1 = \frac{\mu V_b}{\sigma}$, $\pi_2 = \alpha$, $\pi_3 = \beta$, $\pi_4 = \frac{\rho \sigma H}{\mu^2}$, $\pi_5 = \frac{L_2}{H}$, $\pi_6 = \frac{g \mu^2 H}{\sigma^2}$. π_1 is the capillary number. It takes on the form

$$\frac{\mu V_b}{\sigma} = \phi\left(\pi_2, \pi_3, \pi_4, \pi_5, \pi_6\right) \tag{8.6.1}$$

where ϕ is an unknown function that will be determined numerically.

8.6.3 Numerical study

A 2-D CFD model using commercial software, ANSYS-FLUENT 14.5, was built to study the break line of slot die coating on a solid substrate. The geometry and boundary conditions of the FLUENT model are similar as those of the COMSOL model shown in Fig. 6-1. However the bottom substrate in the FLUENT model is a non-porous moving wall without control points. The following die dimensions were fixed in this study: X_1 = 1.3 mm, X_2 = 1.5 mm, W = 250 μm. In the 2-D FLUENT model, the defect of break lines as shown in Figure 8.5 cannot be directly observed. Instead, as indicated in Figure 8.16, the air phase will get entrained between the liquid phase and the substrate when the coating speed exceeds a certain limit. In this study the air phase and liquid phase are approximately divided using a critical volume fraction, 0.5. It is believed that the entrained air phase is an indicator of the instability of a coating bead, which corresponds to physical coating defects observed in experiments. This simulation method has been used and experimentally validated by Bhamidipati et al. [64, 116] in their study of dripping and air entrainment boundaries. Therefore, in this study the appearance of the entrapped air phase is used as the indicator to approximately determine the break line boundary. One example is shown in Figure 8.16. With the coating conditions in Figure

8.16, the break line velocity was found to be around 195 mm/s. For all cases in this study, the precision of break line velocity is either ±2.5 mm/s or ±5 mm/s. Taking the case in Figure 8.16 as an example, keeping all other coating conditions the same, the entrapped air phase does not occur at V = 190 mm/s; but rather 200 mm/s. An average velocity, 195 mm/s, is approximately determined to be the break line velocity. In this example, the precision is ±5 mm/s.

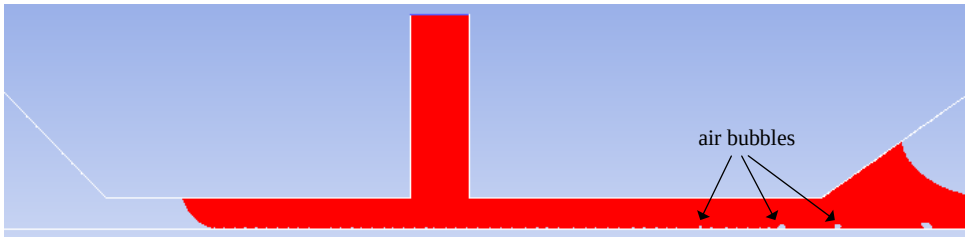

Figure 8.16 Example picture of the air phase entrapped between the liquid and substrate when the coating speed is higher than V_b. Coating conditions are: Q = 21 mm^2/s, V = 200 mm/s, μ = 40 mPa s, σ = 24 mN/s, ρ = 1000 kg/m^3, α = 62 °, β = 69 °, H = 130 μm.

Mesh refinement study

A mesh refinement study was conducted to determine the sufficient element size that can give consistent results of break line velocity. The following parameters are used in the mesh refinement study: μ = 80 mPa s, σ = 24 mN/s, ρ = 1000 kg/m^3, α = 62 °, β = 69 °, and H = 130 μm. Results are shown in Figure 8.17. It can be seen that as the element size decreases from 10 μm to 5.2 μm the break line velocity decreases from around 145 mm/s to around 97.5 mm/s. However, further decreasing the element size does not significantly affect the break line velocity. Based on this result, all calculations in the following study were conducted using the element size around 5.2 μm.

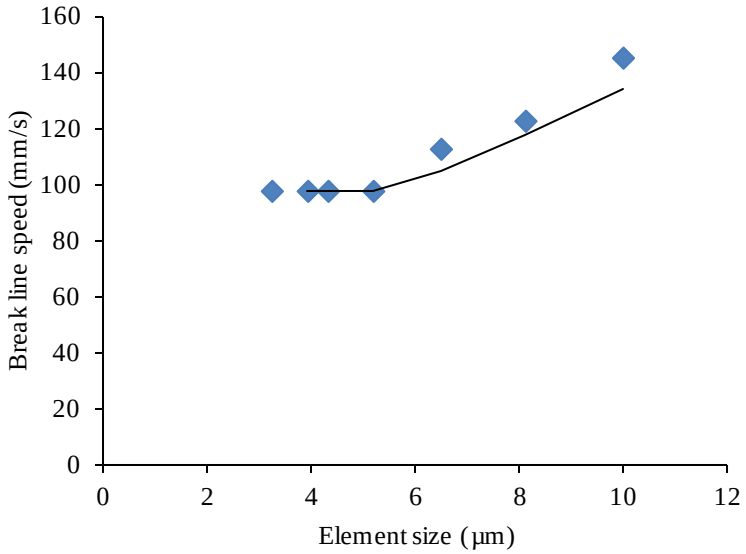

Figure 8.17 Results of mesh refinement study

Effect of viscosity and surface tension on the break line velocity

In Equation (8.6.1), viscosity, μ, and surface tension, σ, appear in π_1, π_4 and π_6. Using the CFD model, the effects of viscosity and surface tension on the break line velocity were studied. Specifically, three viscosity values (20 mPa s, 40 mPa s and 80 mPa s) and two surface tension values (24 mN/s and 48 mN/s) were used. Other fixed parameters were: ρ = 1000 kg/m^3, α = 62 °, β = 69 ° and H = 130 μm. Coating parameters in the current study were chosen to be in the typical range based on existing experimental studies [44, 62, 63, 104-109]. The velocity of the break line boundary was calculated at different flow rate values, and the dripping boundary and air entrainment boundary were calculated using analytical models proposed in the Section 8.2. Results are shown in Figure 8.18.

It can be seen from Figure 8.18 that the break line boundary is almost a vertical line for the different cases. It can also be seen that with a fixed surface tension, 24 mN/s, the break line velocity is inversely proportional to the viscosity. Specifically, the break

line velocity is around 97.5 mm/s, 195 mm/s and 380 mm/s for viscosity values 80 mPa s, 40 mPa s and 20 mPa s, respectively. Checking the expressions of π_1, π_4 and π_6, it can be seen that only π_1 follows this inverse relationship between the break line velocity and viscosity; while π_4 and π_6 do not. This means that the effects of π_4 and π_6 are negligible. Further study found that when the surface tension is doubled from 24 mN/s to 48 mN/s as the viscosity is constant, or the viscosity is doubled from 20 mPa s to 40 mPa s as the surface tension is constant, the coating speed does not significantly change. Thus, the break line velocity is affected by the ratio of surface tension and viscosity. This relation is exactly expressed by the term π_1 in Equation (8.6.1).

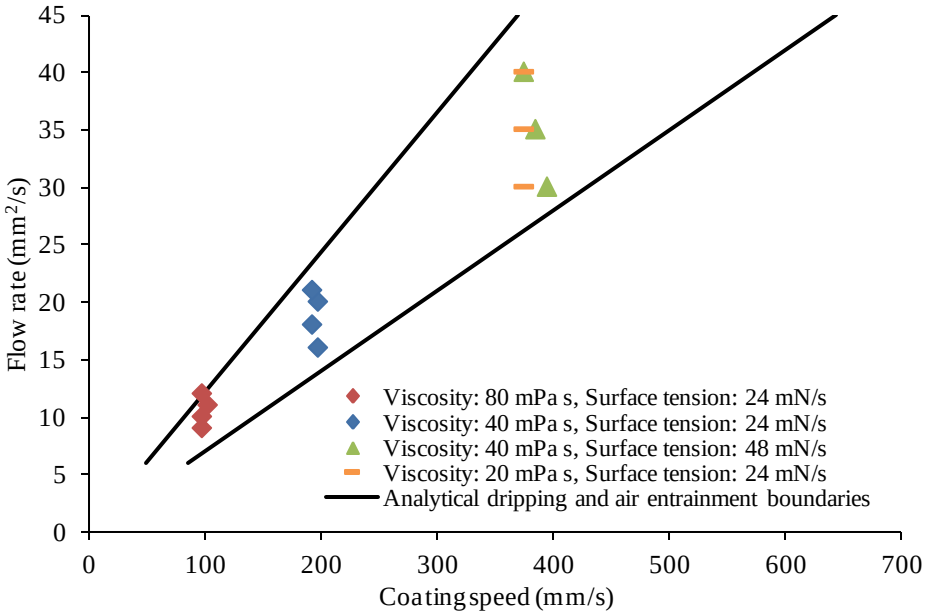

Figure 8.18 Effects of viscosity and surface tension on the break line velocity

Effect of stand-off height on the break line velocity

In Equation (8.6.1), stand-off height, *H*, appears in π_4, π_5 and π_6. The following coating conditions were fixed when studying the effect of stand-off height on break line

velocity: μ = 80 mPa s, σ = 24 mN/s, ρ = 1000 kg/m^3, α = 62 °and β = 69 °. Three stand-off height values were used: 130, 180 and 230 μm. The results are shown in Figure 8.19. It can be seen from Figure 8.19 that increasing stand-off height from 130 μm to 230 μm only shifts the dripping boundary and the air entrainment boundary but does not apparently change the break line boundary. The break line velocity is around 100 mm/s for both cases. Based on this result, the effects of π_4, π_5 and π_6 are negligible.

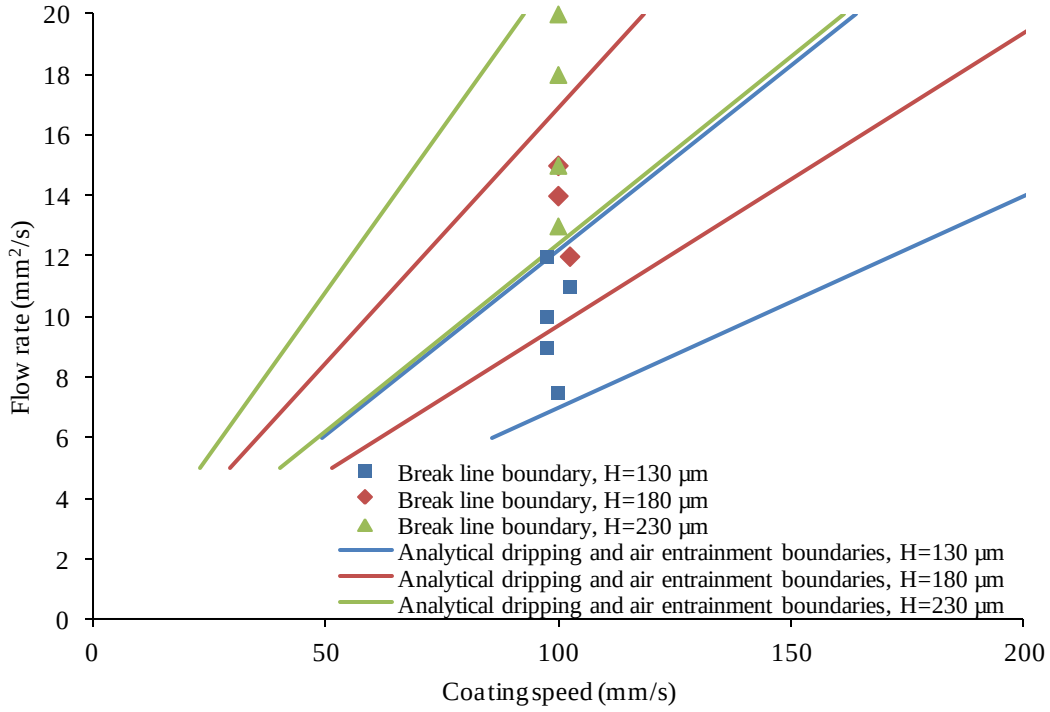

Figure 8.19 Effect of stand-off height on the break line velocity

Effects of contact angles on the break line velocity

In Equation (8.6.1), π_2 and π_3 are the substrate contact angle (α) and the die contact angle (β), respectively. The following coating conditions were fixed when studying the effect of contact angles on the break line velocity: μ = 80 mPa s, σ = 24 mN/s, ρ = 1000 kg/m^3, and H = 130 μm. Several values between 0° to 180° were selected

for α and β. α was fixed at 62° when studying the effect of β; while β was fixed at 69° when studying the effect of α. It has to be mentioned that α and β are static contact angles as inputs for FLUENT. The results are shown in Figure 8.20. It can be seen that the break line velocity seems to be proportional to $\cos(\alpha)+1$, but is not apparently affected by the value of β. Thus, the effect of π_3 is negligible.

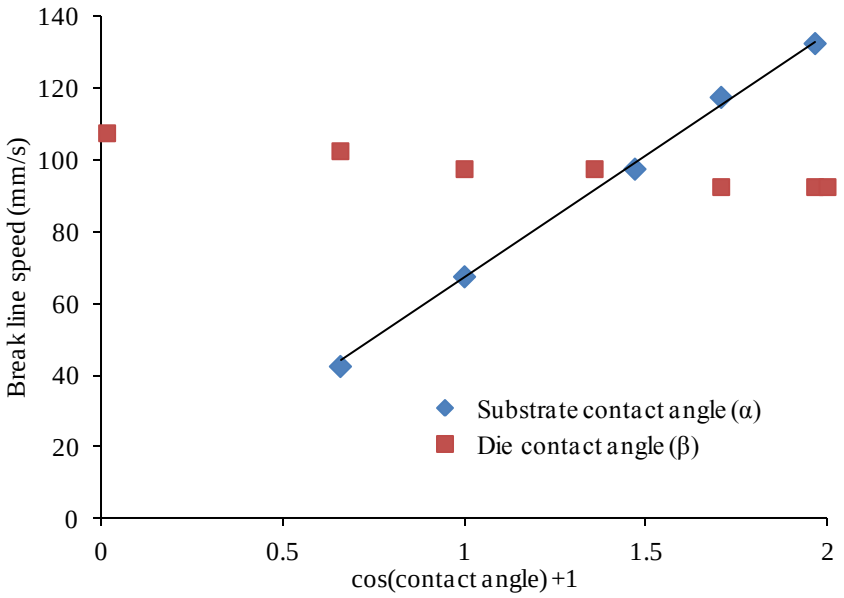

Figure 8.20 Effects of contact angles on the break line velocity

8.6.4 The model of break line boundary for coating Newtonian fluids on a solid substrate

Based on previous numerical study, Equation (8.6.1) is reduced to

$$\frac{\mu V_b}{\sigma} = c \cdot \left[\cos(\alpha)+1\right] \tag{8.6.2}$$

where c is a constant value. Based on all numerical results of V_b in current study, c is found to be around 0.22.

The left side of Equation (8.6.2) is the actually the capillary number. Equation (8.6.2) basically means that there exists a critical capillary number that corresponds to the

break line boundary. If the capillary number is higher than the critical value, good coating will not be obtained. The critical capillary number, based on current study, is mostly determined by the contact angle of fluid on the substrate, i.e., the right side of Equation (8.6.2). Another important conclusion could be obtained from Equation (8.6.2) is that slot die geometry does not affect the break line velocity.

8.6.5 Experimental validation of the developed model of break line boundary

Experimental validation of Equation (8.6.2) is not trivial. Existing experimental studies are either only limited to the air entrainment boundary or minimum wet thickness [44, 63, 105, 106, 108, 109], or use non-Newtonian fluids with added particles [62, 104, 107]. In addition, existing experimental studies usually do not report the contact angles. Gutoff and Kendrick [117] measured the break line velocity for slide coating using several kinds of Newtonian liquids. Slide coating is another premetered coating process [117]. It forms a coating bead between the die and the substrate similar to slot die coating, and it also has a similar form of coating window. Though slide coating uses different die geometry, it is expected to have a similar break line velocity with the slot die coating. This is because, as previously discussed, the break line velocity is mostly determined by fluid properties, instead of die geometry. Gutoff and Kendrick [117] reported the break line velocity, viscosity and surface tension for different fluids. Their results are re-plotted in Figure 8.21. From Figure 8.21 it can be seen that the break line velocity increases almost proportionally with the ratio of surface tension and viscosity. This is exactly the relationship described by Equation (8.6.2). Therefore Gutoff and Kendrick's [117] experimental results provide strong evidence that Equation (8.6.2) can capture the break line boundary reasonably well.

Gutoff and Kendrick [117] did not report the contact angle on the substrate, but based on their experimental results in Figure 8.21, the contact angle values for different liquids in their experiments are expected to be close to each other. Half of the liquids in their experiments are different concentrations of glycerin, which should have similar contact angles because it has been found that glycerin and water usually have similar contact angles on many solids [118, 119]. Using Equation (8.6.2) and the data in Figure 8.21, a contact angle, 71 °, is back calculated.

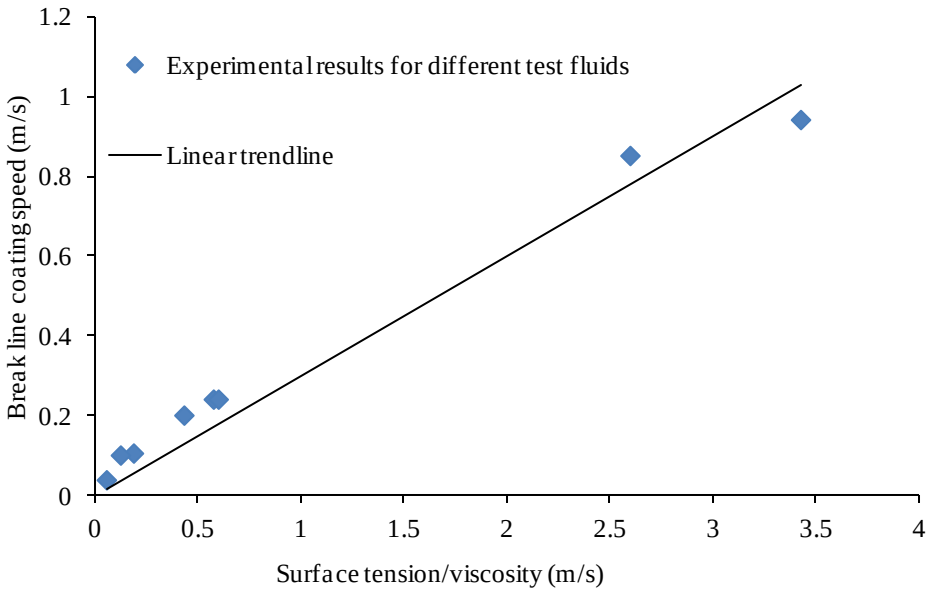

Figure 8.21 Experimentally measured break line velocity changing with the ratio of surface tension and viscosity for Newtonian fluids [117].

8.6.6 The model of break line boundary for coating non-Newtonian fluids on a solid substrate

Though Equation (8.6.2) is developed based on Newtonian fluids, as a first approximation, its utility for non-Newtonian solutions can be examined. Specifically, the

viscosity term is substituted with that for a power law fluid.

$$\frac{\bar{\mu} V_b}{\sigma} \approx c \cdot \left[\cos(\alpha)+1\right] \tag{8.6.3}$$

where $\bar{\mu} = mn\left(\frac{V}{H}\right)^{n-1}$. $\bar{\mu}$ is the approximate viscosity of a non-Newtonian fluid between two parallel plates [96].

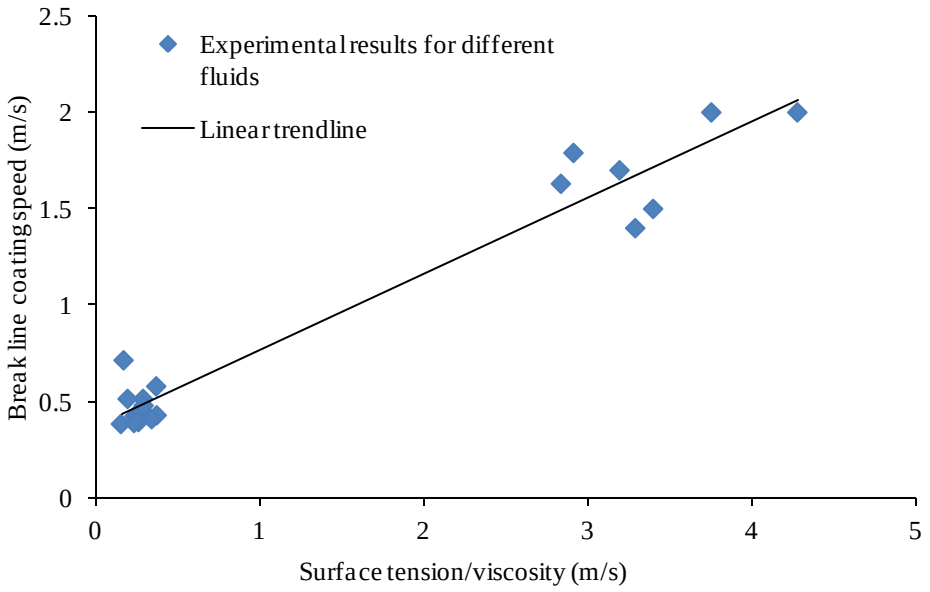

Figure 8.22 Experimentally measured break line velocity changing with the ratio of surface tension and viscosity for non-Newtonian fluids [62].

Ning et al. [62] reported the break line velocity for slot die coating several non-Newtonian polymer liquids. Their results are summarized and re-plotted in Figure 8.22. It can be seen from Figure 8.22 that the break line velocity for non-Newtonian fluids still generally increases with the ratio of surface tension and viscosity. However, data points in Figure 8.22 have a significant deviation. This is probably because the liquids used in Nine et al.'s [62] experiments were mixed with solid particles, which may affect the flow

behavior of the liquids. Another reason is that the contact angle for different liquids in their experiments may significantly differ from each other. Considering these uncertain effects, it is believed that experimental data in Figure 8.22 can serve as evidence for the validation of Equation (8.6.3).

8.6.7 Discussion

In this section, models of the break line boundary for coating Newtonian and non-Newtonian fluids on a solid substrate were developed based on dimensional analysis and numerical study. It has been shown that

1) There exists a critical capillary number that corresponds to the break line boundary. If the capillary number is higher than the critical value, good coating will not be obtained;

2) The critical capillary number is primarily determined by the contact angle of fluid on the substrate, and

3) Slot die geometry affects the dripping and air entrainment boundary but does not affect the break line boundary.

Though models of the break line boundary (Equations (8.6.2) and (8.6.3)) are developed for coating on a solid substrate, they are expected to be able to provide a first approximation for the maximum coating speed on porous substrates. However this study is beyond the scope of current research.

CHAPTER 9. VALIDATION OF ANALYTICAL MODELS OF PENETRATION DEPTH

9.1 Introduction

In this chapter, analytical models of penetration depth derived in Chapter 7 will be validated via comparing with both numerical and experimental results. Numerical results were obtained using the CFD model developed in Chapter 6. Experimental results were obtained for different fluids and different substrate within the coating bounds determined by the model developed in Chapter 8. Finally, the effects of different parameters on penetration depth are discussed using the proposed models.

9.2 Numerical validation

A parametric study was conducted to study coating Newtonian fluids onto porous media using the developed CFD and analytical models. Calculations and simulations were conducted under different processing parameters including coating speed, flow rate, permeability, porosity and viscosity, as shown in Table 9-1. The capillary pressure was assumed to be zero. Thus, Equation (7.3.15) was used to calculate the analytical penetration depth. The geometry of the slot die coating configuration is shown in Figure 6.1 and Figure 6.2. A uniform mesh is used in the CFD model, in which the maximum element size is 0.05 mm. Δs directly below the slot is 0.0417 mm to capture the relatively high velocity gradient in this region, in the remaining section Δs is 0.125 mm. It has been shown that this element size and range of Δs are small enough to ensure good convergence of the simulated results based on coating conditions and parameters used in this study.

Table 9-1 Comparison of numerical and analytical results. [99]

Case	Coating speed (m/s)	2-D Flow rate (m^2/s)	Viscosity (Pa s)	Permeability (m^2)	Porosity	CFD h_f (μm)	Analytical h_f (μm)	Relative error*
1	3.5×10^{-3}	1×10^{-6}	0.4	9.375×10^{-13}	0.75	48.54	48.27	0.56%
2	4×10^{-3}	1×10^{-6}	0.4	9.375×10^{-13}	0.75	39.82	39.67	0.39%
3	4.5×10^{-3}	1×10^{-6}	0.4	9.375×10^{-13}	0.75	32.27	32.81	-1.66%
4	5×10^{-3}	1×10^{-6}	0.4	9.375×10^{-13}	0.75	25.95	27.14	-4.57%
5	4×10^{-3}	0.75×10^{-6}	0.4	9.375×10^{-13}	0.75	22.72	23.83	-4.88%
6	4×10^{-3}	0.8×10^{-6}	0.4	9.375×10^{-13}	0.75	25.69	27.14	-5.63%
7	4×10^{-3}	1.25×10^{-6}	0.4	9.375×10^{-13}	0.75	54.86	54.63	0.43%
8	4×10^{-3}	1×10^{-6}	0.8	9.375×10^{-13}	0.75	40.65	39.67	2.42%
9	4×10^{-3}	1×10^{-6}	1.6	9.375×10^{-13}	0.75	41.45	39.67	4.30%
10	4×10^{-3}	1×10^{-6}	100	9.375×10^{-13}	0.75	41.88	39.67	5.29%
11	4×10^{-3}	1×10^{-6}	0.4	9.375×10^{-14}	0.75	14.14	14.32	-1.27%
12	4×10^{-3}	1×10^{-6}	0.4	4.69×10^{-13}	0.75	29.41	29.63	-0.75%
13	4×10^{-3}	1×10^{-6}	0.4	9.375×10^{-12}	0.75	92.49	89.27	3.48%
14	4×10^{-3}	1×10^{-6}	0.4	9.375×10^{-13}	0.7	40.66	41.31	-1.61%
15	4×10^{-3}	1×10^{-6}	0.4	9.375×10^{-13}	0.6	45.07	45.22	-0.33%
16	4×10^{-3}	1×10^{-6}	0.4	9.375×10^{-13}	0.5	49.64	50.26	-1.26%

* Relative error = (CFD value - analytical value) / (CFD value) ×100%

The final penetration depths calculated from the analytical and CFD models for coating Newtonian fluids have been compared with each other to check their consistency. From Table 9-1, it can be seen that the results from both models are in good agreement. The overall relative error is less than 6%. As discussed in Chapter 6 and 7, these models were developed based on different methodologies (i.e., CFD and analytical formulation), different derivation procedures, with different governing equations for the coating bead (i.e., Navier-Stokes equations and lubrication theory). Thus, the consistency of results in Table 9-1 can serve as preliminary evidence that both analytical and CFD models for the final penetration depth are valid. However, additional validation experiments were also conducted.

9.3 Experimental validation

9.3.1 Material

Experiments have been conducted to validate the proposed analytical models of final penetration depth. Glycerin, a Newtonian fluid with 99.91 wt%, and black strap molasses, a non-Newtonian fluid, purchased of the shelf were used as test fluids. Glycerin has the following viscosity, density and surface tension: 0.91 Pa s [120], 1260 kg/m^3 and 0.063 N/m [121], respectively. Molasses has the following power law properties, density and surface tension [64]: m = 8.07 Pa s^n, n = 0.83, 1452 kg/m^3 and 0.047 N/m, respectively. Therefore, glycerin is relatively low viscous, while molasses is relatively high viscous. The following die dimensions were fixed in experiments: X_1 = 5.207 mm, X_2 = 4.648 mm, W = 250 μm. The experiments were conducted at ambient temperature, 25°C. Three kinds of Toray 090, carbon paper, were chosen as the porous substrates. Specifically, the carbon paper used in the experiments includes Toray 090 purchased in 2011, Toray 090 purchased in 2013 and Toray 090 treated with 20% Polytetrafluoroethylene (PTFE) purchased in 2013. They were classified as Toray 090 (2011), Toray 090 (2013) and Toray 090 (PTFE), respectively. Porous media properties including permeability, porosity and average pore radius could be found from literature, and are shown in Table 9-2. Contact angle of two kinds of test fluids on the surface of the each carbon paper was measured in house by using a Rame-Hart goniometer. The droplets were stable on the porous media during the measurements. Measurements were conducted at least 10 times for each case and average values were calculated, as shown in Table 9-2. Due to the effect of penetration and the micro pores structure on the surface of carbon paper, the measured contact angle has relatively large deviation. Different batches of Toray 090

were initially supposed to have the same property. However, it was found that the 2011 batch and 2013 batch have apparent different contact angle values. Therefore they are treated as two kinds of substrates in the experiments. The discrepancy of the surface contact angle is believed to be related with surface treatment in the production. The microstructure of Toray series carbon paper has been measured and studied by a lot of researchers [122-126], thus it is believed to be consistent for different batches. Therefore other properties related with microstructure including permeability, porosity and average pore radius were assumed to be consistent for different batches.

Table 9-2 Properties of different porous media with respect to molasses and glycerin as applicable

Substrate	Permeability k (m^2)	Porosity ε	Average pore radius r (μm)	Contact angle θ (°)		Capillary pressure p_c (Pa)	
				Molasses	Glycerin	Molasses	Glycerin
Toray 090 (2011)	8.99 e-12 [124]	0.79 [124]	9.5 [126]	98.9 ± 7.5	99.5 ± 6.5	-1500	-2200
Toray 090 (2013)	8.99 e-12 [124]	0.79 [124]	9.5 [126]	122.9 ± 10.2	115.9 ± 5.0	-5400	-5800
Toray 090 (PTFE)	6.36 e-12 [123]	0.69 [123]	8.5 [122]	146.6 ± 4.2	-	-9200	-

In this study, the capillary pressure in the porous media was approximately evaluated by

$$p_c = \frac{2\sigma\cos\theta}{r} \tag{9.1}$$

where σ is surface tension, θ is contact angle of coating liquid on the surface of carbon paper, r is the average pore radius. The approximate capillary pressure values for all

cases are shown in Table 9-2. It can be seen that since all contact angles are higher than 90° the capillary pressure values are all negative. It has to be declared that Equation (9.1) is only an approximate evaluation of the capillary effect in the porous media. The real capillary pressure is related with dynamic advancing contact angle and the microstructure inside the porous media [100-102, 127], which are far more complex and beyond the scope of the current study. In this study, for simplification, the capillary pressure is assumed to be approximately constant to evaluate the overall capillary effect during the penetration process.

Table 9-3 Processing parameters for experiments

Test #	Substrate	Fluid	Flow rate, Q (mm^2/s)	Stand-off height, H (μm)	Analytical coating speed range (mm/s)	Experimental coating speed range (mm/s)
1	Toray 090 (2011)	Molasses	0.520	140	1.3~7.2	2.3~5.8
2	Toray 090 (2011)	Molasses	0.288	140	0.8~4.0	1.5-3.6
3	Toray 090 (2011)	Molasses	0.715	250	1.9~5.6	2.2-4.7
4	Toray 090 (2013)	Molasses	0.848	170	2.6~9.7	4.0-5.6
5	Toray 090 (PTFE)	Molasses	0.848	170	3.3~9.7	3.6-5.3
6	Toray 090 (PTFE)	Molasses	1.143	210	4.3~10.6	4.8-5.2
7	Toray 090 (PTFE)	Molasses	0.730	170	3.0~8.4	3.2-4.0
8	Toray 090 (2011)	Glycerin	0.603	115	1.9~10.2	2.6-4.7
9	Toray 090 (2013)	Glycerin	0.706	130	3.9~10.6	3.6-5.2*

* The used minimum coating speed, 3.6 mm/s for Test #9, was a little bit smaller than the analytical value, 3.9 mm/s. However, when 3.6 mm/s was used, dripping was not observed. This is because the measured penetration depth was higher than the predicted value for that case and the real dripping boundary was smaller than the predicted value, also.

9.3.2 Experimental design

Experiments were conducted under different processing parameters including flow rate, coating speed, permeability, porosity, viscosity, fluid and substrate, as shown in Table 9-3. The experimental coating speed was controlled in the analytical coating bounds calculated using Equation 8.4.1. No defects were observed for any case. This provides preliminary evidence that the developed analytical coating speed range on the porous substrate is accurate.

9.3.3 Penetration depth measurement method

The penetration depth was determined by measuring the weight of the penetrated fluid. After coating the carbon paper, the top fluid on the coated sample was immediately removed with a blade. A schematic of the initial coated porous substrate is shown in Figure 9.1(a) and Figure 9.1(b) shows the sample after the top fluid is removed. The weight, M_t, and the area, A_t, of the sample without top fluid (Figure 9.1(b)), are measured first. Then weight of the carbon paper, M_p, is calculated by $M_p = \rho_a \cdot A_t$, where ρ_a is the area density of the carbon paper. ρ_a has been measured to be around 1.186×10^{-4}, 1.264×10^{-4} and 1.462×10^{-4} g/mm^2 for Toray 090 (2011), Toray 090 (2013) and Toray 090 (PTFE), respectively. Then, the weight of the penetrated fluid, M_f, is calculated by $M_f = M_t - M_p$. Using M_f, the penetration depth is calculated by

$$h_f = \frac{M_f}{\rho A_t \varepsilon} \tag{9.2}$$

in which ρ is the density of the coated liquid. In this study, three samples were made and measured for each set of coating conditions; and the average penetration depth and standard deviation were calculated based on three samples.

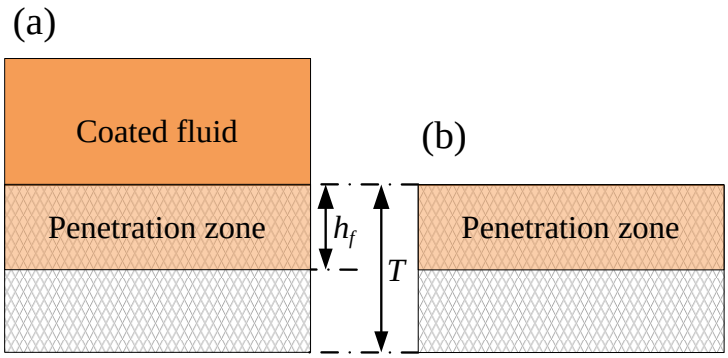

Figure 9.1 Schematic of coated porous substrate (a) with and (b) without the top fluid. In this study, the test and measurement was repeated at least three times for each data point, and the standard error was calculated for each data point.

9.3.4 Experimental results

The experimental results of Test #1 are shown and compared with analytical results in Figure 9.2. For comparison, analytical penetration depth is calculated with and without capillary pressure. Specifically, Equations 7.5.12 and 7.10.2 are used for calculation. It can be seen from Figure 9.2 that the analytical models agree with experimental results well. However the error between predicted and measured penetration depth seems relatively higher when either the coating speed is higher than 5 mm/s or lower than 3 mm/s. This phenomenon can be explained in the following way. As coating speed increases, the penetration depth decreases. However, the physical penetration depth cannot decrease below a critical limit. This critical limit is imposed by the assumption that the penetration depth must be larger than the pore size, to ensure the permeability is the same as what is based on the overall transport property of the porous media. The porous flow in a very thin top layer of the carbon paper cannot be explained by the Darcy's law which describes an overall transport characteristic. It has been found that regardless of how fast the coating speed is, some pores on the surface of the carbon paper will be filled. Based on all the experimental results from Tests #1-#9, it was found that

the penetration depth does not significantly decrease beyond 40 μm which is equivalent to two pores. This can explain the relatively higher error when the coating speed is higher than 5 mm/s. Analytical models developed in Chapter 7 are based on an assumption that the coating speed is relatively high (assumption 5 in Section 7.2). Thus, if the coating speed is too low the error might increase. This can explain the increased error when the coating speed is lower than 3 mm/s.

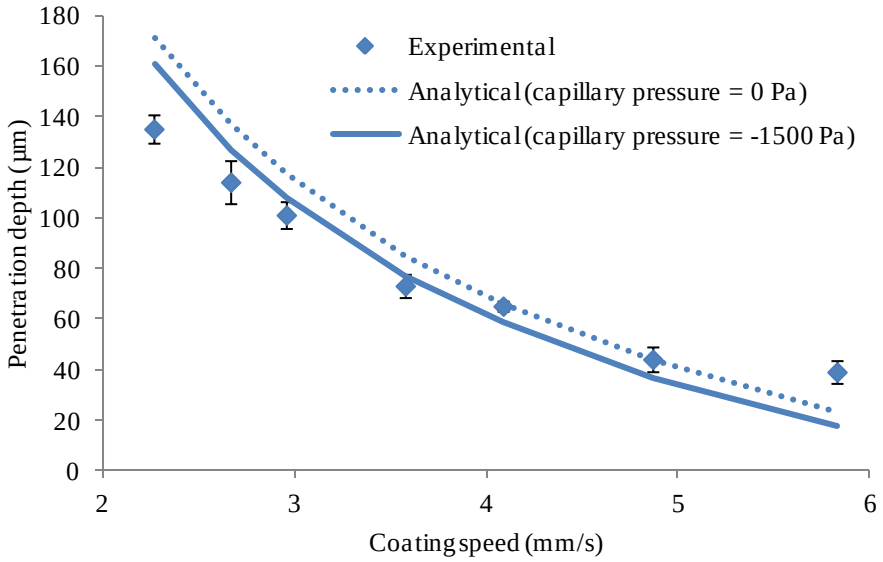

Figure 9.2 Experimental and predicted results of Test #1.

It can also be seen from Figure 9.2 that the capillary pressure does not significantly affect the calculated penetration depth. The capillary pressure only shifts the curve of predicted penetration depth down by 5~10 μm. This is because the maximum pressure in the coating bead, using Equation 8.2.3, is generally between 3000 ~ 6300 Pa under the coating conditions of Test #1. This is much higher than the absolute value of capillary pressure, 1500 Pa. Therefore, the pressure in the coating bead dominates the penetration process. Based on lubrication theory, the high pressure in the coating bead is

caused by relatively high viscosity of molasses and relatively smaller stand-off height, 140 μm, used in Test #1. This phenomenon is important because it suggests that the capillary effect on penetration depth might be ignored when coating a relatively high viscosity fluid.

Tests #2 and #3 were conducted using either higher stand-off height or lower flow rate than Test #1. Under the coating conditions of Test # 2 and #3, the pressure in the coating bead is smaller, thus the effect of capillary pressure is expected to be more significant. Results of these two tests are shown in Figure 9.3 and Figure 9.4, respectively. Comparing Figure 9.3 and Figure 9.4, it is clearly shown that the effect of capillary pressure is more significant in Tests #2 and #3 than that in Test #1. Specifically, the capillary pressure shifts the curve of predicted penetration depth down by 9~15 μm and 23~34 μm for Tests #2 and #3, respectively. Under the coating conditions of Tests #2 and #3, the analytical model with capillary pressure apparently gives a better prediction than that without capillary pressure, as expected. In addition, as in Test #1, the measured penetration depth in Tests #2 and #3 does not decrease below 40 μm.

Tests #4 and #5 were conducted using the same flow rate, stand-off height and similar coating speed range but different substrates. One is Toray (2013) the other is Toray (PTFE). These two substrates have different permeability and porosity, and more importantly, cause different capillary pressure. Experimental results in Figure 9.5 clearly show the difference of penetration depth on these two substrates. Specifically, Toray (PTFE) has a low penetration depth level because the PTFE treated carbon paper is more hydrophobic. This follows the expected trend. Compared with Tests #1, #2 and #3, the results in Figure 9.5 show an even more significant effect of capillary pressure on

penetration depth. Specifically, the capillary pressure decreases the penetration depth by 29~38 μm and 47~60 μm in Tests #4 and #5, respectively. Although the capillary pressure is higher, the developed models still give reasonable predictions for the penetration depth. The predicted values generally follow the same trend as the measured penetration depth. However, the error between the predicted and measured penetration depth is relatively larger for coating Toray (PTFE).

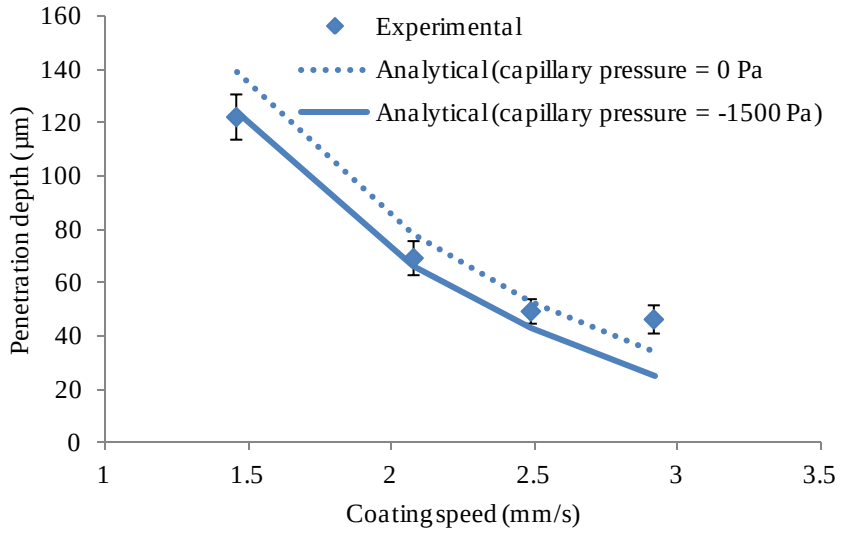

Figure 9.3 Experimental and predicted results of Test #2.

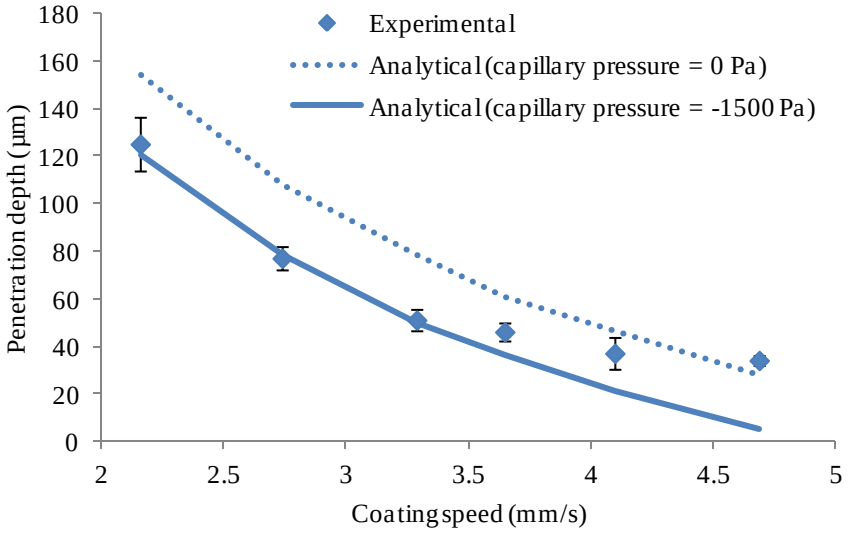

Figure 9.4 Experimental and predicted results of Test #3.

To double check the accuracy of proposed models for relatively higher capillary pressure conditions, Tests #6 and #7 were conducted, using Toray (PTFE). Different flow rates and coating speeds were used in these two tests. Results are shown in Figure 9.6 and Figure 9.7. Based on the results, the model considering capillary pressure is much closer to the experimental results than the model without considering capillary pressure. The predicted penetration depth is reasonable and generally matches the experimental results well. However, the error for a relatively higher capillary pressure condition, i.e., -9200 Pa in Tests # 5, #6 and #7, seems larger than the error for a relatively lower capillary condition, i.e., -1500 Pa in Tests #1 and #2 and -5400 Pa in Test #3. The error between predicted and measured penetration depth will be analyzed in detail in the following Section 9.3.5.

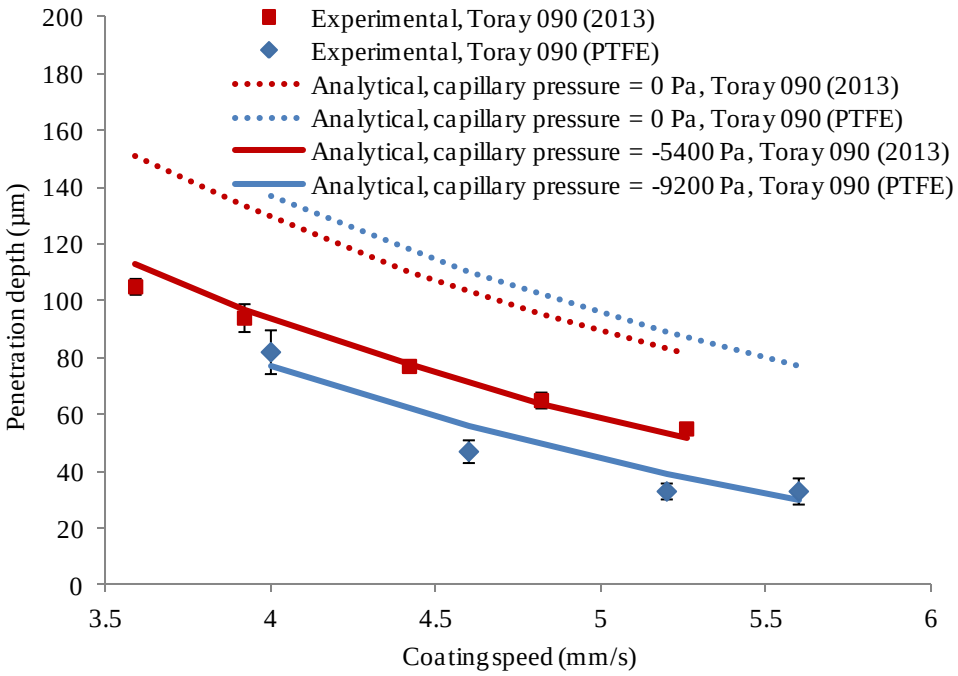

Figure 9.5 Experimental and predicted results of Tests #4 and #5.

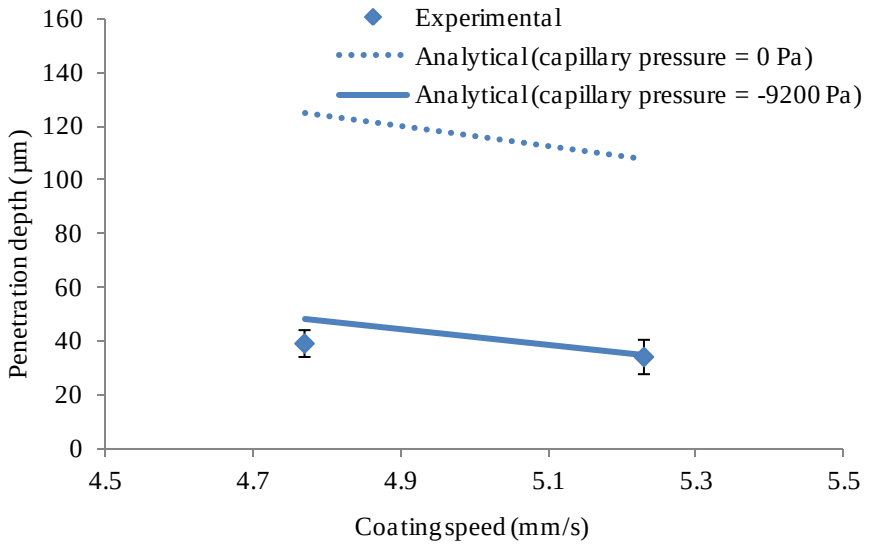

Figure 9.6 Experimental and predicted results of Test #6.

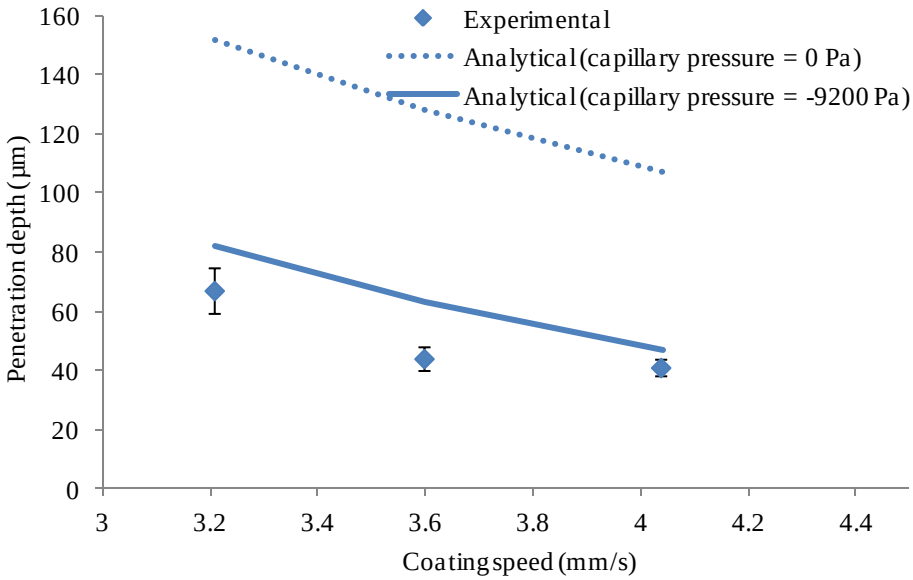

Figure 9.7 Experimental and predicted results of Test #7.

The power law model developed by Bhamidipati et al.'s [64] for non-Newtonian molasses is generally valid for shear rates between 1 to 100 1/s. In current study, the shear rate of porous flow can be approximately evaluated by $v_{p\text{-}ave}/r$ in which $v_{p\text{-}ave}$ is the average penetration velocity and r is the average pore radius. $v_{p\text{-}ave}$ can be approximated

by $h_f/(L_2/V)$ in which the denominator is the approximate penetration time. The shear rate in the coating bead can be approximately evaluated by V/H. Using the data from Tests #1 to #7, the shear rate is around 3 ~ 9 and 10 ~ 40 1/s for the porous flow and the flow in the coating bead, respectively. Therefore, the power law model of molasses measured by Bhamidipati et al. [64] is valid for the coating conditions in this study.

As discussed in Section 7.5, the generalized lubrication theory, Equations (7.5.2) and (7.5.3), used in the analytical models for penetration depth of non-Newtonian fluids can a give good approximation for pressure gradient when the flow behavior index, n, is higher than 0.5 and the 2-D flow rate in the channel is between $0.2VH$ to $0.8VH$ [96]. In current study, the flow behavior index, n, of molasses is 0.83. The approximate flow rate in the right channel, Q-$h_f V\varepsilon$, is around $0.3VH$ to $1.0VH$ which is pretty close to the range required for a good approximation. Therefore, the developed analytical penetration depth models for non-Newtonian fluids can be generally used for the coating conditions in current study.

Tests #8 and #9 were conducted by coating glycerin under different coating conditions. Two kinds of substrates were used: Toray (2011) for Test #8 and Toray (2013) for Test #9, respectively. Base on the results in Figure 9.8 and Figure 9.9, it can be seen that the predicted penetration depth matches the experimental results well. The general trend and error is similar to those for coating molasses. This means that the developed models give a reasonable prediction of penetration for both Newtonian and non-Newtonian fluids. However, the error between predicted and measured values in Test #9 seems larger than that in Test #8. This difference is believed to be related with the

relatively higher capillary pressure in Test #9, which will be discussed in the following section.

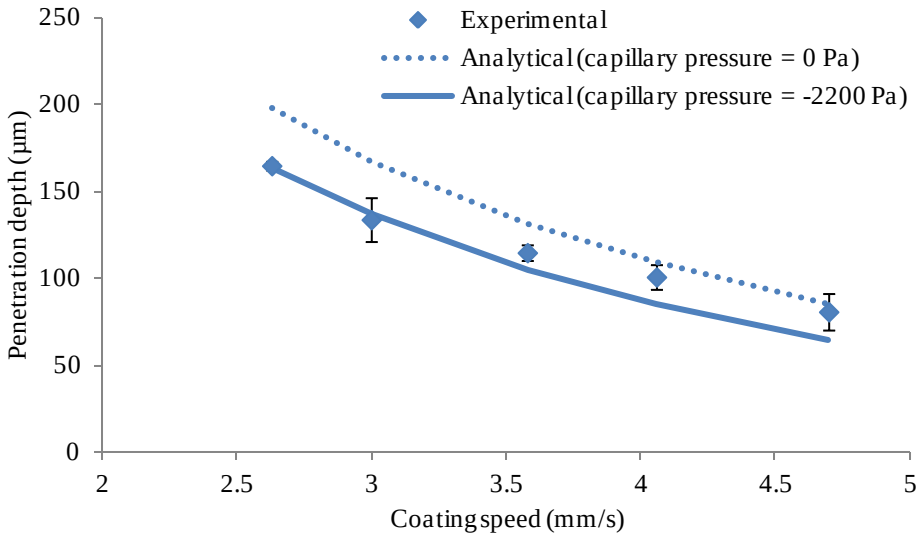

Figure 9.8 Experimental and predicted results of Test #8.

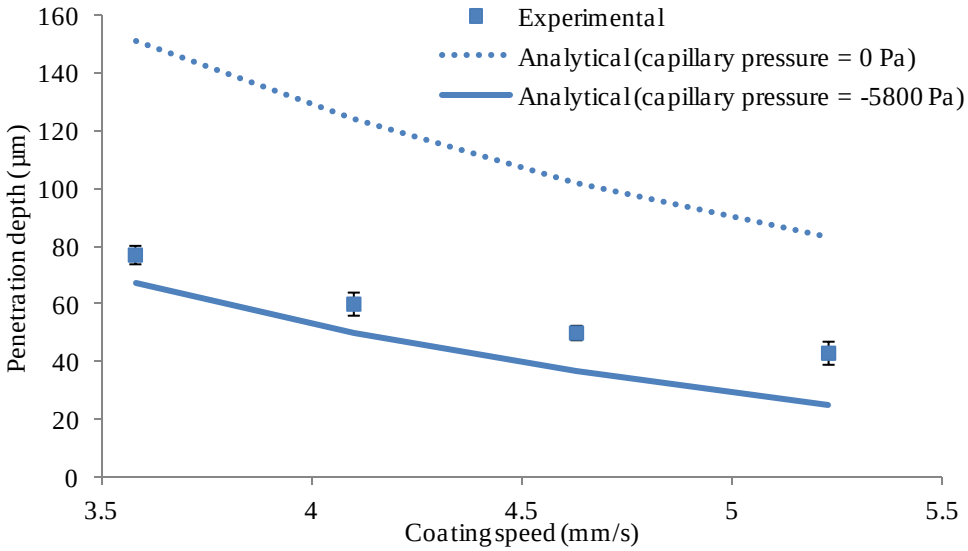

Figure 9.9 Experimental and predicted results of Test #9.

9.4 Error analysis

Based on previous experimental results, it seems that the error between the predicted and measured penetration directly depends on the magnitude of capillary pressure. Higher capillary pressure seems to generate larger error. This is because of several uncertainties in the capillary pressure calculation. One uncertainty is caused by the average pore radius used in Equation (9.1). The pore radius of Toray series carbon paper has been extensively studied by many researchers using different methods. The most common method used is mercury intrusion porosimetry (MIP) [122, 123, 128, 129], in which the carbon paper is approximately assumed to be composed by a bundle of capillary tubes, and the pore radius is the radius of the capillary tubes. Other methods that have been used to study the pore radius of Toray series carbon paper include the method of standard porosimety (MSP) [125], confocal microscopy [130], pore network model [126] and breakthrough pressure of water [131]. There is inconsistency in the results of different investigations, but the typical value of the average pore radius in Toray series carbon paper has been found to be around 10 μm [132]. The values shown in Table 9-2 were selected to be close to the typical value. Therefore, the bundle of capillary tubes is only a simplification of the real geometry in porous media, and there exists inconsistency of the measured average pore radius, introducing error into the capillary pressure calculation.

Another uncertainty related to the capillary pressure calculation comes from the measurement of contact angle. There are several contact angle concepts related to porous media. The contact angle observed on the surface of a porous medium is usually referred as an apparent contact angle; while the contact on the chemically heterogeneous fibers is usually referred as an effective contact angle [125]. Cassie-Baxter equation can be used to

evaluate the effective contact angle based on the apparent contact [133], however Cassie-Baxter equation is derived based on a grid formed of cylindrical fibers which is not the case for carbon paper in current study. The contact angle measured in current study is a static contact angle; while the contact angle during the penetration process is dynamic [100, 102] and expected to be advancing. Therefore the capillary pressure in the porous media should be governed by a real-advancing contact angle, versus an apparent-static contact angle. Since an effective contact angle is usually smaller than an apparent contact angle [125, 133], but an advancing contact angle is larger than a static contact angle, it is very difficult to compare the relative magnitude between a real-advancing contact angle and an apparent-static contact angle. In addition, due to the effect of penetration and the micro-porous structure on the surface of carbon paper, the measured contact angle in current study has a relatively large deviation, as shown in Table 9-2. Thus, the uncertainty of contact angle is expected to introduce error into the capillary pressure calculation.

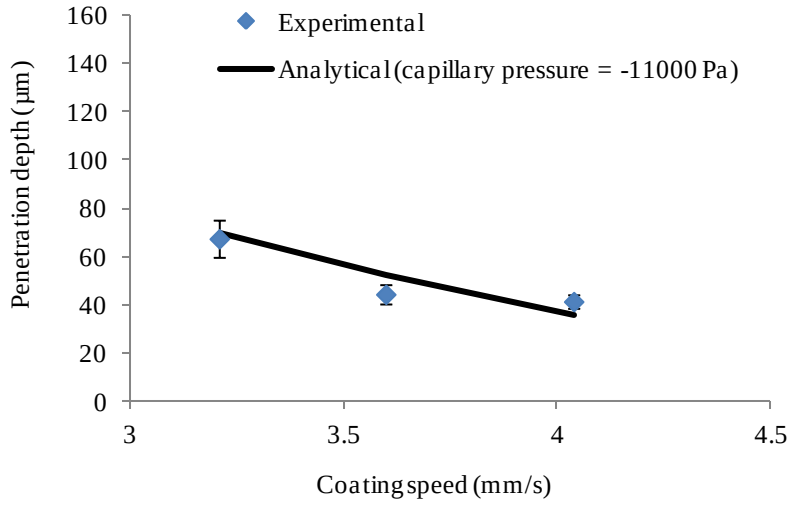

Figure 9.10 Experimental and predicted penetration using back calculated capillary pressure for Test #7.

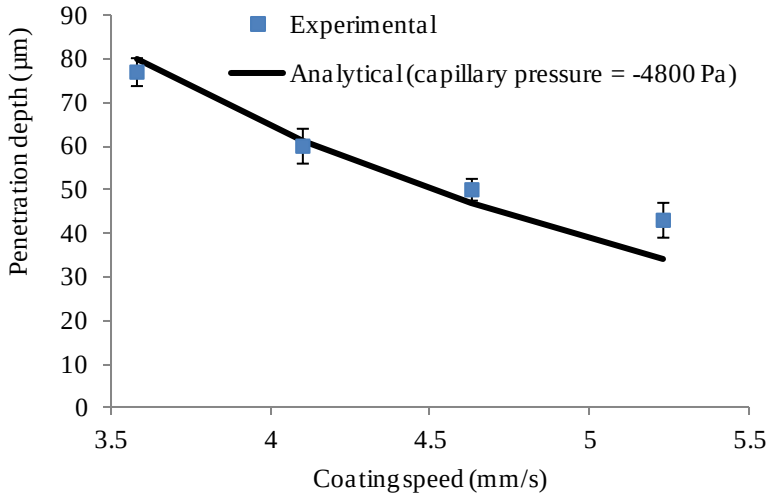

Figure 9.11 Experimental and predicted penetration using back calculated capillary pressure for Test #9.

In order to check the accuracy of the predicted capillary pressures used for Test #7 and #9 (which have larger relative errors than other tests), the analytical curves were shifted to fit experimental data. The input capillary pressure value was adjusted until the predicted penetration depth fit the experimental data; as shown in Figure 9.10 and Figure 9.11. It was found that the capillary pressures are close to -11000 and -4800 Pa, for Tests #7 and #9, respectively. Therefore, for Test #7, the predicted capillary pressure, -9200 Pa, is smaller than the capillary pressure found after shifting the data; while for Test #9, the predicted capillary pressure, -5800 Pa, is larger. However, generally the predicted values are close to those that align with the experimental data. Therefore, the predicted capillary pressure is assumed to be reasonable.

The error is expected to be affected by the relative magnitude between the capillary pressure and the pressure in the coating bead. A higher capillary pressure or lower coating bead pressure is expected to introduce a larger error into the developed models. The relative error between the predicted and measured values for all data points

in previous experiments have been calculated and plotted with respect to p_{max}/p_c, which is the ratio of the maximum coating bead pressure and the capillary pressure. The results are shown in Figure 9.12. It can be seen from Figure 9.12 that the overall relative error is lower than 20% for all tests. This demonstrates that the developed models are relatively accurate. It can also be seen that all data points with a relative error higher than 20% occur when p_{max}/p_c is small (less than 1.7). This demonstrates that a higher capillary pressure or lower coating bead pressure tends to cause a larger error to the model, which is consistent with the results discussed previously.

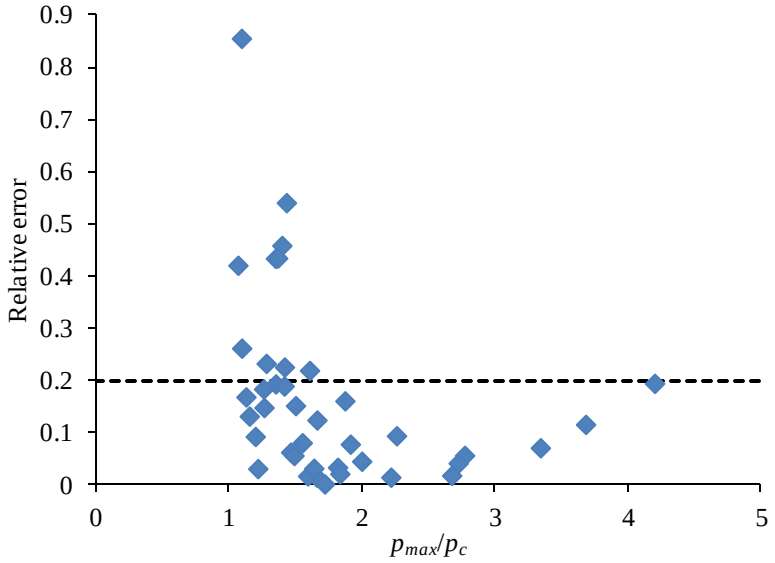

Figure 9.12 Effect of the p_{max}/p_c on the magnitude of relative error. p_{max} is calculated by multiplying the pressure gradient in the right channel (Equation 7.3.13 or 7.5.11) with the right channel length, L_2. Relative error = (predicted value – measured value)/measured value.

Except the error introduced by approximating the capillary pressure, other error sources include the approximation and simplification used when developing the models, the instability or uncertainty of the coating speed, flow rate, stand-off height and porous media properties used in the experiments. Considering all of these effects, it is believed

that the experimental results shown in Figure 9.2 to Figure 9.9 are reasonable, and can serve as evidence that the analytical models developed in this study are accurate.

9.5 Effects of coating parameters on penetration depth

The effects of all coating parameters, including coating speed, flow rate, permeability, porosity, viscosity and capillary pressure, on the final penetration depth can be studied conveniently with the developed analytical models. The effect of coating speed has already been shown from Figure 9.2 to Figure 9.9. Decreasing the coating speed will increase the penetration depth. The larger penetration depth is because of the pressure increase in the coating bead which increases the penetration velocity (Equations 7.2.4 and 7.2.5). The effects of flow rate, permeability and porosity can be summarized based on the data in Table 9-1. The data are shown graphically in Figure 9.13(a)-(b). It can be seen that increasing the flow rate will increase the penetration depth. This is because of the pressure increase in the coating bead which increases the penetration velocity (Equations 7.2.4 and 7.2.5). It can also be seen that increasing the permeability without changing porosity or decreasing the porosity without changing permeability will increase the penetration depth. This relationship is also due to the increase of penetration velocity (Equation 7.2.1).

The effects of viscosity and capillary pressure on penetration depth during slot die coating are investigated. Specifically, the capillary pressure is fixed as 100 and -100 Pa, viscosity changes from 0.1 to 10 Pa-s, while all other coating conditions are the same as those used for case 1 in Table 9-1. The penetration depths calculated using different capillary pressure and viscosity values are shown in Figure 9.14.

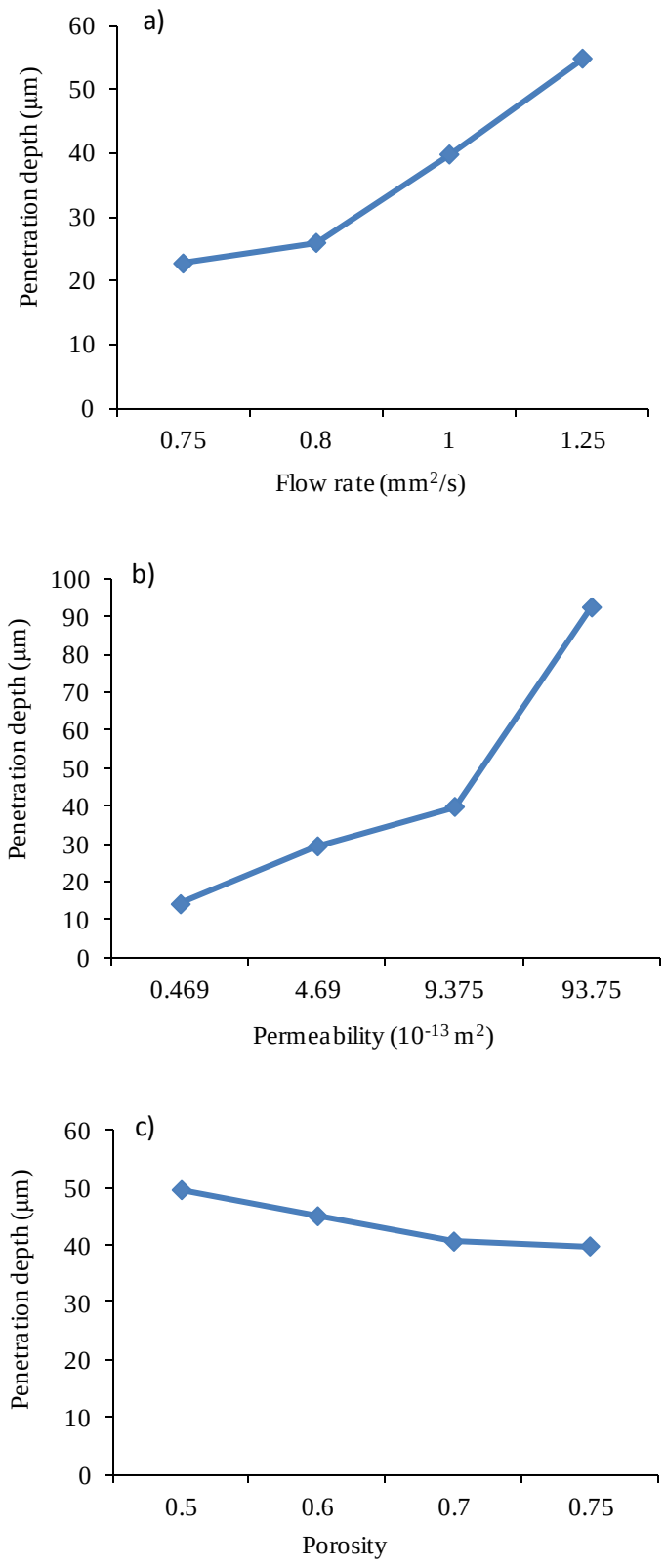

Figure 9.13 Effects of (a) flow rate, (b) permeability and (c) on the final penetration depth. [99]

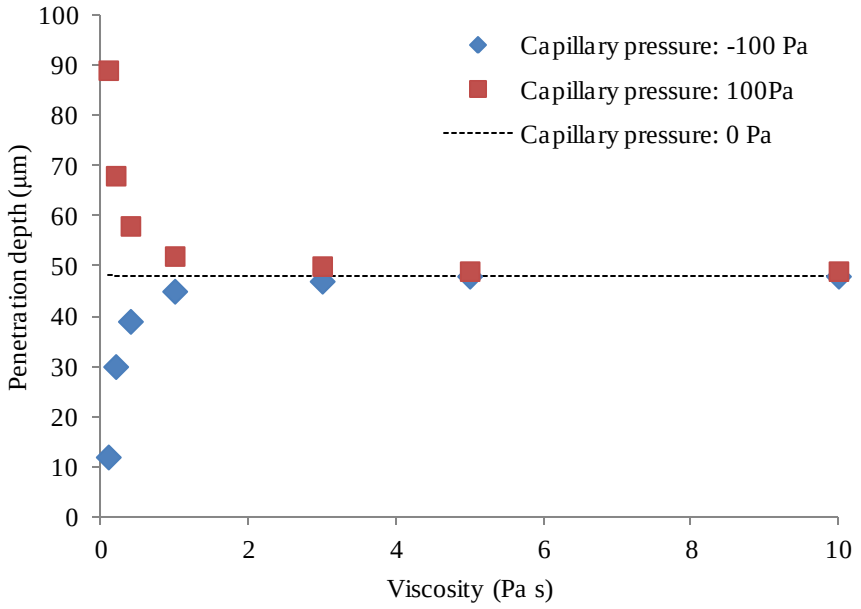

Figure 9.14 Effect of viscosity and capillary pressure on the penetration depth.

As seen from the Figure 9.14, when capillary pressure is negative the penetration depth increases as viscosity increases; whereas when capillary pressure is positive the penetration depth decreases as viscosity increases. With increasing viscosity, the penetration depth, regardless of the capillary pressure, approaches 48 μm, which is obtained with zero capillary pressure. This result suggests that at a lower viscosity the capillary pressure has a more significant effect on the penetration depth; and vice versa. This is reasonable because the penetration depth is governed by both the pressure in the coating bead and the capillary pressure in the porous media. If the viscosity is low, the capillary pressure will dominate the penetration; while if the viscosity is sufficiently high, the pressure in the coating bead will dominate the penetration and the penetration depth approaches a constant value. In order to evaluate the relative importance of the coating bead pressure and the capillary pressure, the dimensionless value p_{max}/p_c is used, in which

p_{max} is the maximum coating bead pressure of coating a solid substrate. Using Equations 8.2.2 and 8.2.3, the expression of p_{max}/p_c can be given as

$$\frac{p_{max}}{p_c} = \frac{6\mu(2Q - VH)L_2}{H^3 p_c} \tag{9.3}$$

The effect of capillary pressure on penetration depth in Figure 9.14 can also be evaluated by the absolute percentage difference between the penetration depth calculated with capillary pressure and that calculated without capillary pressure. The relationship between $p_{max}/|p_c|$ and the effect of capillary pressure on penetration depth is shown in Figure 9.15. It can be seen that the effect of capillary pressure on penetration depth is smaller than 10% when $p_{max}/|p_c|$ is higher than 10. Therefore, $p_{max}/|p_c| = 10$ can be approximately used as a criterion to determine whether the effect of capillary pressure on penetration depth is significant or not. It has to be mentioned that p_{max} in Equation (9.3) is calculated for coating a solid substrate; whereas p_{max} in Figure 9.12 is calculated for coating a porous substrate.

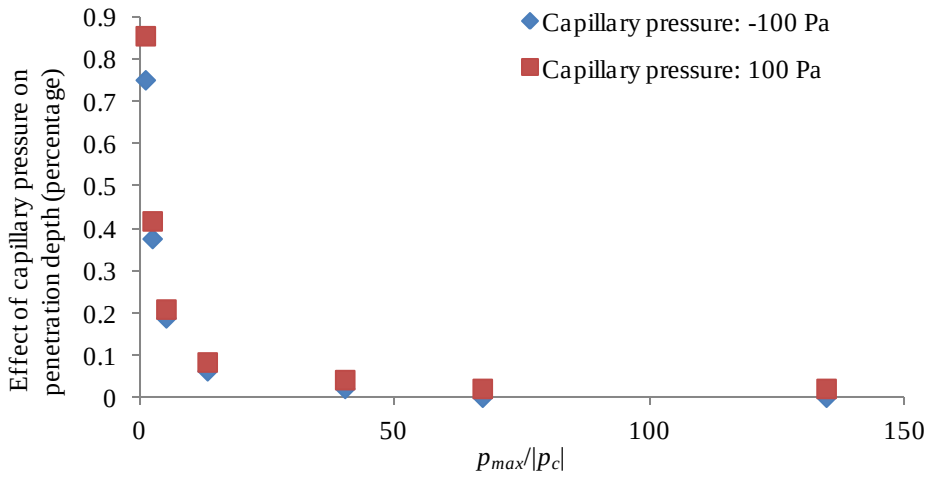

Figure 9.15 Relationship between $p_{max}/|p_c|$ and the effect of capillary pressure on penetration depth

9.6 Penetration in Region II of slot die coating onto porous media

The results in Section 9.5 suggest that the capillary effect on the penetration depth can be ignored if the fluid viscosity is sufficiently high. This conclusion has been demonstrated experimentally in Section 9.3.4. This conclusion is not only valid for the penetration below the slot die where h_f is defined in this study, but also for fluid penetration that occurs beyond the slot die lip, in the downstream meniscus prior to solidification, i.e. in Region II of slot die coating on porous media, as shown in Fig. 5-1. Therefore, the change of penetration depth in Region II can be ignored for a high viscous fluid. Yesilalan et al. [15] showed that viscosity had no effect on penetration depth. Based on the results in this thesis, it can be suggested that this is due to the high viscosity (36.7, 98.8 and 158 Pa-s) of the fluids used in their experiments.

Another factor that prevents the change of penetration depth in Region II is called the pinning effect, which is related to two phase flow in random fiber porous media [127]. Wiklund and Uesaka used a free-energy lattice Boltzman approach to perform simulations of liquid penetration into random porous media [127]. Their results showed discontinuities in the solid-surface curvature, including sharp edge, high-curvature point, widening pores and branching channels, prevent liquid flow through their pinning effects and interaction with local geometry. They found that penetration driven by capillary pressure cannot consistently continue due to pinning. The penetration in Region II in current study is mostly driven by capillary pressure. Therefore it is expected that pinning effects will prevent the change of penetration depth in Region II.

Though the change of penetration depth in the phase transition region (Region II) is very complex to model due to the uncertainty of material properties, we still can expect

that the penetration depth may not change much in Region II due to high viscous effect and pinning. The significance of this conclusion is that it suggests that the developed models of the final penetration depth in Region I in current study can be directly used to evaluate the overall penetration depth of both Region I and II under following assumptions:

(1) Viscosity of coating fluids is sufficiently high, thus capillary effect could be ignored, and

(2) Porous medium has a random microstructure, thus there are pinning effects in the porous media.

SUMMARY OF PART II

Part II of this dissertation focuses on fluid penetration when coating porous media. Specifically, in Chapter 6, CFD models using commercial software, COMSOL 4.2a, were developed to study fluid penetration into a porous medium during slot die coating. Models for Newtonian and non-Newtonian fluids were developed separately. The penetration depth and pressure distribution along the porous media were calculated using the CFD model for Newtonian fluids to illustrate the characteristics of the penetration process. In Chapter 7, a series of analytical models for penetration depth during slot die coating on porous substrates were developed for both Newtonian and non-Newtonian fluids with and without considering the capillary effect. In Chapter 8, several models of coating window boundaries on both solid and porous substrates were developed based on analytical derivations and CFD simulations. In Chapter 9, analytical models of penetration depth were validated numerically and experimentally. The effects of different parameters on penetration depth were discussed using the developed models.

Based on the numerical and experimental results in Chapters 6, 7, 8 and 9, the most important conclusions of Part II are summarized as follows:

- The magnitude of the pressure on the porous substrate is lower than that on the solid substrate. Therefore estimating the pressure based on a solid substrate, as done in existing modeling work [15, 36, 42, 88, 89], will over predict the penetration depth.
- A positive capillary pressure (hydrophilic or contact angle < 90°) will increase the penetration depth; while a negative capillary pressure (hydrophobic or contact angle > 90°) will decrease the penetration depth.

- Non-Newtonian fluids and Newtonian fluids have the same dripping boundary and air entrainment boundary, which are determined by the flow rate and geometry of the die. Viscosity or other fluid properties do not affect these two coating boundaries.
- Both the dripping boundary and air entrainment boundary on the porous substrate shifts to lower coating speeds compared with that on the solid substrate.
- There exists a critical capillary number which corresponds to the break line boundary. If the capillary number is higher than the critical value, good coating will not be obtained. The critical capillary number is mostly determined by the contact angle of fluid on the substrate. Slot die geometry does not affect the break line velocity.
- Analytical models of penetration depth have been experimentally validated. The overall relative error between the predicted and measured penetration depth is generally lower than 20% for most tests. This demonstrates that the developed models are accurate. In addition, a higher capillary pressure or lower coating bead pressure will introduce increased error to the analytical models.
- Either increasing the flow rate or decreasing the coating speed will increase the penetration depth. In addition, increasing the permeability without changing porosity or decreasing the porosity without changing permeability will also increase the penetration depth.
- When capillary pressure is negative the penetration depth increases as the viscosity increases; whereas when capillary pressure is positive the penetration depth decreases as viscosity increases. At a lower viscosity the capillary pressure

has a more significant effect on the penetration depth; and vice versa. If the viscosity is high enough, the effect of capillary pressure will be negligible and the penetration depth approaches a constant value. $p_{max}/|p_c| = 10$ calculated using Equation (9.3) can be approximately used as a criterion to determine whether the effect of capillary pressure on penetration depth is significant or not.

- The penetration depth may not change much during the Region II due to high viscous effect and pinning effects.

The objective of Part II is to fundamentally understand fluid penetration and predict the penetration depth during direct coating on porous media using a holistic methodology. Effective and efficient analytical tools have been developed to facilitate predicting and controlling the penetration depth for coating porous media.

CHAPTER 10. CONTRIBUTIONS AND FUTURE WORK

10.1 Key contributions

A two-part study of slot die coating onto porous substrates has been conducted. Key contributions of this study are:

Fundamental contributions:

- Provides a series of analytical models for quickly evaluating the penetration depth. These models are derived based on the lubrication equations for Newtonian and non-Newtonian fluids [96], Darcy's law and the modified Blake-Kozeny equation [97, 98]. The derivation is also based on the assumptions given in Section 7.2. These models are developed for the Region I of coating porous media but can also be directly used to evaluate the overall penetration depth of both Region I and II if the viscosity of coating fluids is sufficiently high and the porous medium has a random microstructure. Experiments have validated the accuracy of proposed models.
- Provides analytical models of dripping and air entrainment boundaries for both solid and porous substrates, and models of the break line boundary for a solid substrate. The analytical models of dripping and air entrainment boundaries are derived based on the assumptions given in Section 8.1.4. The models for coating a solid substrate have been validated by comparing with previous researchers' experimental results [62-64, 104, 105, 108]. However, the models for coating a porous substrate have not been experimentally studied, and are believed to be able to give a first approximation for the coating boundaries. The model of the break line

boundary is developed for coating Newtonian fluids onto a solid substrate and has been partially validated by comparing with a previous researcher's experimental results [117].

Engineering contributions:

- Experimentally elucidates the feasibility, effectiveness and efficiency of the new MEA manufacturing techniques based on direct coating of the membrane solution onto the catalyzed GDLs.
- Provides a CFD model for simulating the coating process on porous media based on slot die coating. The modeling method can also be used for other coating techniques, such as roll coating and blade coating.
- Original and detailed experimental data and discussion of the new MEA manufacturing technique provided in this research will help manufacturers in the fuel-cell industry choose proper techniques to reduce waste, cost and time.
- Original and detailed experimental data of penetration depth of slot die coating on porous media provided in this research can help manufacturers in the coating industry to increase products durability, and reduce the production cost.

10.2 Future Work

Manufacturing of MEA

In Part I of study, the feasibility of fabricating MEAs for PEM fuel cells using direct coating polymer electrolyte membrane solution onto the catalyzed GDLs was demonstrated. However, the penetration of membrane solution decreases the porosity of the catalyst layer and alters the balance of its ionic conductivity and electronic

conductivity, thus negatively affects the performance of fuel cells. In the current study Nafion® solution has a strong wettability in the catalyst layer, which generates a positive (hydrophilic) capillary pressure. Therefore the penetration is excessive. In part II of this study, it was demonstrated that a high viscosity fluid will reduce the effect of capillary pressure. It was also demonstrated that a negative capillary pressure will reduce the penetration depth. Therefore, it is possible to decrease the penetration of membrane solution by either increasing its viscosity or decreasing its wettability. If the penetration depth can be controlled to less than 10 μm which is a normal thickness of the catalyst layer, the performance of the MEA is expected to be improved and the bond strength between the membrane and the catalyst layer is expected to be enhanced.

Coating window

The dripping and air entrainment boundaries for coating porous media derived in this study are based on the assumption that the upstream meniscus can only move in the range of upstream die lip. This assumption is a direct analogy of coating a solid substrate. To the best of author's knowledge, the coating boundaries for coating a porous substrate has not been studied; thus no experimental data could be found to directly demonstrate dripping and air entrainment boundaries for coating porous media. In addition, modeling work of the break line boundary is only limited to the solid substrate. To date, the mechanism of defects generation of coating porous media is not well understood, the existence of the break line boundary for coating porous media is still unknown. Therefore, more experimental work should be done to further understand the operational boundaries of coating porous media.

Modeling of penetration depth

Models of penetration depth in current study are macro-scale models. They are derived based on Darcy's law which only describes the overall transport property of a porous medium. Therefore, the developed models in the current study can only give an evaluation of the overall penetration depth, but cannot provide any information of penetration depth distribution in the porous media. In order to glean more insights on the penetration depth distribution, micro-scale approaches can be used, such as pore-network model [36, 42], Lattice-Boltzmann method, [91, 92] or solving the Navier-Stokes equations [93]. However, as discussed in Section 5.2, micro-scale models require detailed morphology information of the porous media, the geometrical details, and even an extremely fine mesh of the microstructure of the porous media to simulate the flow behavior. Thus, they are computationally time consuming and are typically applied only to small domains. In addition, it will be very challenging to directly couple a two-phase porous flow in a micro-scale model with a two-phase free flow in a coating bead. In order to overcome the limitations of a micro-scale model, the pressure distribution in the coating bead on a porous substrate can be initially calculated using a macro-scale model developed in the thesis. Then, the pressure distribution can be transferred to the time domain as a dynamic pressure boundary condition and be applied onto a micro-scale model of a porous substrate to calculate the penetration distribution in the substrate.

REFERENCES

1. H. L. Lee, J. D. Kim, K. H. Lee, C. H. Kim and H. J. Youn, "Effect of Coating Formulations and Drying Methods on the Coverage and Smoothness of Brown Grade Base Papers", *Nordic Pulp and Paper Research Journal*, **27**, 79 (2012).

2. Y. Li and B. He, "Investigation into the Coating Surface Topography and Properties of Paper Related to Drying Condition." in International Conference on Chemical Engineering and Advanced Materials (CEAM 2011) Advanced Materials Research, Changsha, 2011.

3. H. Z. Wang, C. S. Zhao and S. H. Yu, "The Study of a Kind of New Synthetic Paper Coating Thickness Agent." in 2011 International Conference on Chemical Engineering and Advanced Materials (CEAM 2011)Advanced Materials Research, Changsha, 2011.

4. J. Du, "The Interfacial Chemistry of Paper and Paper Coatings", in *2011 PaperCon Conference*, p. 618, TAPPI Press, Covington (2011).

5. J. S. Preston, C. Nutbeem and R. Chapman, "Impact of Pigment Blend and Binder Level on the Structure and Printability of Coated Papers." in 2011 PaperCon ConferencePaper Conference and Trade Show 2011, PaperCon 2011, Covington, 2011.

6. Y. Tang, M. Chen, Y. Li, Y. Zhao and X. Zhang, "Comparative Effect of Hydrophilic and Lipophilic Nanosized Titanium Dioxide on the Properties of Coated Paper." in 2011 International Conference on Eco-Dyeing, Finishing and Green Chemistry (EDFGC 2011)Advanced Materials Research, Hangzhou, 2011.

7. M. Afsharpour, F. T. Rad and H. Malekian, "New Cellulosic Titanium Dioxide Nanocomposite as a Protective Coating for Preserving Paper-Art-Works", *Journal of Cultural Heritage*, **12**, 380 (2011).

8. C. Challener, "Paper Coatings-Opportunities Abound", *Chemistry and Industry*, **8**, 16 (2011).

9. E. Triki, C. Arrieta, H. Boukehili and T. Vu-Khanh, "Tear Behavior of Polyester-Based Coated Textiles after Thermo-Oxidative Aging", *Polymer Composites*, **33**, 1007 (2012).

10. M. Glowania, T. Gries, J. Schoene, M. Schleser and U. Reisgen, "Innovative Coating Technology for Textile Reinforcements of Concrete Applications", *Key Engineering Materials*, **466**, 167 (2011).

11. Y. Park and E. Kim, "Wearing Comfort of Temperature-Adaptable Textiles by Dual-Phase Coatings between Phase-Change Materials and Silicon Carbide Particles", *Journal of Applied Polymer Science*, **126**, E151 (2012).

12. Q. B. Meng, S.-I. Lee, C. Nah and Y.-S. Lee, "Preparation of Waterborne Polyurethanes Using an Amphiphilic Diol for Breathable Waterproof Textile Coatings", *Progress in Organic Coatings*, **66**, 382 (2009).

13. N. Didane, S. Giraud and E. Devaux, "Fire Performances Comparison of Back Coating and Melt Spinning Approaches for Pet Covering Textiles", *Polymer Degradation and Stability*, **97**, 1083 (2012).

14. T. Bashir, M. Skrifvars and N. K. Persson, "Surface Modification of Conductive Pedot Coated Textile Yarns with Silicone Resin", *Materials Technology*, **26**, 135 (2011).

15. H. E. Yesilalan, S. B. Warner and R. Laoulache, "Penetration of Blade-Applied Viscous Coatings into Yarns in a Woven Fabric", *Textile Research Journal*, **80**, 1930 (2010).

16. B. Yue, C. Wang, X. Ding and G. G. Wallace, "Polypyrrole Coated Nylon Lycra Fabric as Stretchable Electrode for Supercapacitor Applications", *Electrochimica Acta*, **68**, 18 (2012).

17. M. Zhang, C. Wang, S. Wang, Y. Shi and J. Li, "Fabrication of Coral-Like Superhydrophobic Coating on Filter Paper for Water–Oil Separation", *Applied Surface Science*, **261**, 764 (2012).

18. R. P. Lydon, "New Composite Filter Media", *Filtration and Separation*, **37**, 26 (2000).

19. L. Cindrella, A. M. Kannan, J. F. Lin, K. Saminathan, Y. Ho, C. W. Lin and J. Wertz, "Gas Diffusion Layer for Proton Exchange Membrane Fuel Cells-a Review", *Journal of Power Sources*, **194**, 146 (2009).

20. S. Litster and G. Mclean, "Review Pem Fuel Cell Electodes", *Journal of Power Sources*, **130**, 61 (2004).

21. R. H. Puffer and S. J. Rock, "Recent Advances in High Temperature Proton Exchange Membrane Fuel Cell Manufacturing", *Journal of Fuel Cell Science and Technology*, **6**, 041013 (2009).

22. V. Mehta and J. S. Cooper, "Review and Analysis of Pem Fuel Cell Design and Manufacturing", *Journal of Power Sources*, **114**, 32 (2003).

23. Y. S. Kim, S. H. Jung and C. Lim, Effect of Cathode Compression During Hot-Pressing on Cell Performance and Its Optimization, in *1st Symposium on the Manufacturing of MEAs for Hydrogen Applications*, Dayton, OH (2005).

24. T. A. L. Harris and D. F. Walczyk, "Development of a Casting Technique for Membrane Material Used in High-Temperature Pem Fuel Cells", *Journal of Manufacturing Processes*, **8**, 8 (2006).

25. T. A. L. Harris, D. F. Walczyk and M. M. Weber, "Manufacturing of High-Temperature Polymer Electrolyte Membranes-Part II: Implementation and System Model Validation", *Journal of Fuel Cell Science and Technology*, **7**, 011008 (2010).

26. H. P. Dhar, "Near Ambient, Unhumidified Solid Polymer Fuel Cell", US Patent No. 5,318,863 (1994).

27. H. P. Dhar, "Method for Catalyzing a Gas Diffusion Electrode", US Patent No. 5,521,020 (1996).

28. S. A. Grot, "Preparation of Fuel Cell Electrode Assemblies", US Patent No. 6,641,862 B1 (2003).

29. S. A. Grot, "Fuel Cell Electrode Assemblies", US Patent No. 2004/0191601 A1 (2004).

30. M. Uchida, J. Niikura, H. Gyoten, Y. Takebe, K. Hatoh, M. Hosaka, A. Mukoyama, H. Shimoda and S. Kinoshita, "Method for Producing Film Electrode Jointed Product and Method for Producing Solid Polymer Type Fuel Cell", US Patent No. 6,855,178 B2 (2005).

31. W. G. O'Brien, "Continuous Production of Catalyst Coated Membranes", US Patent No. 7,316,794 B2 (2008).

32. Y. Li and B. He, "Characterization of Ink Pigment Penetration and Distribution Related to Surface Topography of Paper Using Confocal Laser Scanning Microscopy", *BioResources*, **6**, 2690 (2011).

33. P. Resch, W. Bauer and U. Hirn, "Calendering Effects on Coating Pore Structure and Ink Setting Behavior", *Tappi Journal*, **9**, 27 (2010).

34. Y. O'Takehiro, M. Kawasaki, D. Sakakibara and F. Nonomura, "Research on Ink Peeling-Off of High Gloss Coated Paper", *Japan Tappi Journal*, **63**, 70 (2009).

35. K. Matilainen, T. Hamalainen, A. Savolainen, T. Sipilainen-Malm, J. Peltonen, T. Erho and M. Smolander, "Performance and Penetration of Laccase and ABTS Inks on Various Printing Substrates", *Colloids and Surfaces B: Biointerfaces*, **90**, 119 (2012).

36. J. Ghassemzadeh, M. Hashemi, L. Sartor and M. Sahimi, "Pore Network Simulation of Imbibition into Paper During Coating: I. Model Development", *AIChE Journal*, **47**, 519 (2001).

37. G. Ascanio, B. Taboada and P. A. Tanguy, "Misting Droplet Size Analysis in a Metered Film Coater", *Chemical Engineering Research and Design*, **86**, 215 (2008).

38. N. Triantafillopoulos and T. Grankvist, "Coating Viscoelasticity and Blade Coating Defects", *Paperi ja Puu/Paper and Timber*, **76**, 663 (1994).

39. R. L. Janes and J. D. McKenzie, The Behavior of Bentonites in Pigmented Paper Coatings-Effects on Rheology, Application, Coated Paper Properties and Printability, in *TAPPI Coating Conference*, p. 31, Boston (1976).

40. S. Pavlidou, S. Mai, T. Zorbas and C. D. Papaspyrides, "Mechanical Properties of Glass Fabric/Polyester Composites: Effect of Silicone Coatings on the Fabrics", *Journal of Applied Polymer Science*, **91**, 1300 (2004).

41. J. Hopkins, "Nordson: Porous Coating with Hot Melts", *Textile World*, **146**, 79 (1996).

42. J. Ghassemzadeh and M. Sahimi, "Pore Network Simulation of Fluid Imbibition into Paper During Coating-Iii: Modeling of the Two-Phase Flow", *Chemical Engineering Science*, **59**, 2281 (2004).

43. O. J. Romero, W. J. Suszynski, L. E. Scriven and M. S. Carvalho, "Low-Flow Limit in Slot Coating of Dilute Solutions of High Molecular Weight Polymer", *Journal of Non-Newtonian Fluid Mechanics*, **118**, 137 (2004).

44. Y.-N. Lin, T.-J. Liu and S.-J. Hwang, "Minimum Wet Thickness for Double-Layer Slide-Slot Coating of Poly (Vinyl-Alcohol) Solutions", *Polymer Engineering and Science*, **45**, 1590 (2005).

45. S.-Y. Lu, Y.-P. Lin and T.-J. Liu, "Coating Window for Double Layer Extrusion Slot Coating of Poly (Vinyl-Alcohol) Solutions", *Polymer Engineering and Science*, **41**, 1823 (2001).

46. M. Schrödner, S. Sensfuss, H. Schache, K. Schultheis, T. Welzel, K. Heinemann, R. Milker, J. Marten and L. Blankenburg, "Reel-to-Reel Wet Coating by Variation of Solvents and Compounds of Photoactive Inks for Polymer Solar Cell Production", *Solar Energy Materials and Solar Cells* (2012).

47. H. F. Dam and F. C. Krebs, "Simple Roll Coater with Variable Coating and Temperature Control for Printed Polymer Solar Cells", *Solar Energy Materials and Solar Cells*, **97**, 191 (2012).

48. T. T. Larsen-Olsen, B. Andreasen, T. R. Andersen, A. P. L. Bottiger, E. Bundgaard, K. Norrman, J. W. Andreasen, M. Jrgensen and F. C. Krebs, "Simultaneous Multilayer Formation of the Polymer Solar Cell Stack Using Roll-to-Roll Double Slot-Die Coating from Water", *Solar Energy Materials and Solar Cells*, **97**, 22 (2012).

49. X. Ding, S. Didari, T. F. Fuller and T. A. Harris, "A New Fabrication Technique to Manufacture an Mea Using Direct Coating of Nafion onto Catalyzed Gdl", *ECS Transactions*, **33**, 255 (2010).

50. X. Ding, S. Didari, T. F. Fuller and T. A. L. Harris, "Membrane Electrode Assembly Fabrication Process for Directly Coating Catalyzed Gas Diffusion Layers", *Journal of The Electrochemical Society*, **159**, B746 (2012).

51. X. Ding, S. Didari, T. F. Fuller and T. A. L. Harris, "Effects of Annealing Conditions on the Performance of Solution Cast Nafion Membranes", *Journal of The Electrochemical Society*, **160**, F793 (2013).

52. X. Ding, T. F. Fuller and T. A. L. Harris, "Effects of Annealing Conditions on the Performance of Solution Cast Nafion Membranes", *ECS Transactions*, **41**, 1537 (2011).

53. K. Iwasaki, T. Ohba, T. Miyama and M. Onodera, "Electrode for Fuel Cell, Method of Manufacturing Same, and Fuel Cell with Such Electrode", US Patent No. 7,091,149 B2 (2006).

54. H. Tang, S. Wang, S. P. Jiang and M. Pan, "A Comparative Study of Ccm and Hot-Pressed Meas for Pem Fuel Cells", *Journal of Power Sources*, **170**, 140 (2007).

55. S.-I. Han, I.-H. Son, M.-Y. Jang and H.-K. Lee, "Membrane-Electrode Assembly for Fule Cell, Method of Preparing Same, and Fuel Cell System Comprising Same", US Patent No. 2008/0268314 A1 (2008).

56. C. Wang and J. Dong, "Methods for Fabricating Membrane Electrode Assembles of Fuel Cells", US Patent No. 2006/0090317 A1 (2006).

57. J. Kohler, K.-A. Starz, S. Wittpahl and M. Diehl, "Process for Producing a Membrane Electrode Assembly for Fuel Cells", US Patent No. 6,998,149 B2 (2006).

58. P. STRASSER, P. MANI and R. SRIVASTAVA, "De-Alloyed Membrane Electrode Assemblies in Fuel Cells", US Patent No. 2009/0098420 A1 (2009).

59. H.-L. Chang, H.-R. Chang, Kuo-Lon, Shieh and P.-H. Cheng, "Method for Fabricating Membrane Electrode Assembly", US Patent No. 2010/0201021 A1 (2010).

60. S.-D. Yim, S.-H. Park, G.-G. Park, Y.-J. Sohn, M. Kim, T.-H. Yang, Y.-G. Yoon, C.-S. Kim and W.-Y. Lee, "Membrane Electrode Assembly (Mea) Fabrication Procedure on Polymer Electrolyte Membrane Fuel Cell", US Patent No. 2011/0097651 A1 (2011).

61. K. S. Lee and Y. S. Kim, "Method of Manufacturing Membrane-Electrode Assembly for Fuel Cell", US Patent No. 7,837,819 B2 (2010).

62. C.-Y. Ning, C.-C. Tsai and T.-J. Liu, "The Effect of Polymer Additives on Extrusion Slot Coating", *Chemical Engineering Science*, **51**, 3289 (1996).

63. K.-Y. Lee, L.-D. Liu and T.-J. Liu, "Minimum Wet Thickness in Extrusion Slot Coating", *Chemical Engineering Science*, **47**, 1703 (1992).

64. K. L. Bhamidipati, S. Didari, P. Bedell and T. A. L. Harris, "Wetting Phenomena During Processing of High-Viscosity Shear-Thinning Fluid", *Journal of Non-Newtonian Fluid Mechanics*, **166**, 723 (2011).

65. D. A. Wald, J. M. Le, M. A. Yandrasits and P. M. Boucher, "Fuel Cell Membrane Electrode Assembly with Sealing Surfaces", US Patent No. 7,553,578 B2 (2009).

66. R. H. Barton, P. R. Gibb, J. A. Ronne and H. H. Voss, "Membrane Electrode Assembly for an Electrochemical Fuel Cell and a Method of Making an Improved Membrane Electrode Assembly", US Patent No. 6,057,054 (2000).

67. F. Liu, B. Yi, D. Xing, J. Yu and H. Zhang, "Nafion/Ptfe Composite Membranes for Fuel Cell Applications", *Journal of Membrane Science*, **212**, 213 (2003).

68. R. F. Silva, S. Passerini and A. Pozio, "Solution-Cast Nafion®/Montmorillonite Composite Membrane with Low Methanol Permeability", *Electrochimica Acta*, **50**, 2639 (2005).

69. S. M. Slade, T. R. Ralph, C. P. De Leon, S. A. Campbell and F. C. Walsh, "The Ionic Conductivity of a Nafion® 1100 Series of Proton-Exchange Membranes Re-Cast from Butan-1-ol and Propan-2-ol", *Fuel Cells*, **10**, 567 (2010).

70. G. Gebel, P. Aldebert and M. Pineri, "Structure and Related Properties of Solution-Cast Perfluorosulfonated Ionomer Films", *Macromolecules*, **20**, 1425 (1987).

71. R. B. Moore III and C. R. Martin, "Chemical and Morphological Properties of Solution-Cast Perfluorosulfonate Ionomers", *Macromolecules*, **21**, 1334 (1988).

72. S. Vengatesan, E. Cho, H.-J. Kim and T.-H. Lim, "Effects of Curing Condition of Solution Cast Nafion® Membranes on Pemfc Performance", *Korean Journal of Chemical Engineering*, **26**, 679 (2009).

73. L. A. Zook and J. Leddy, "Density and Solubility of Nafion: Recast, Annealed, and Commercial Films", *Analytical Chemistry*, **68**, 3793 (1996).

74. R.-J. Chung, T.-S. Chin, L.-C. Chen and M.-F. Hsieh, "Preparation of Gradually Componential Metal Electrode on Solution-Casted Nafion® Membrane", *Biomolecular Engineering*, **24**, 434 (2007).

75. C.-H. Ma, T. L. Yu, H.-L. Lin, Y.-T. Huang, Y.-L. Chen, U. S. Jeng, Y.-H. Lai and Y.-S. Sun, "Morphology and Properties of Nafion Membranes Prepared by Solution Casting", *Polymer*, **50**, 1764 (2009).

76. S. Werner, L. Jörissen and U. Heider, "Conductivity and Mechanical Properties of Recast Nafion Films", *Ionics*, **2**, 19 (1996).

77. MEA Preconditioning and Qualification Protocol, Available from Web: Http://9gfgw.Qdok6.Servertrust.Com/V/Meapreconditioningqualificationprotocol.Pdf. Last Retrieved on Oct. 30, 2012., in.

78. M. Falk, *Chaper 8 in "Perfluorinated Ionomer Membranes"*, Washington, D.C. (1982).

79. C. Huang, K. Seng Tan, J. Lin and K. Lee Tan, "XRD and XPS Analysis of the Degradation of the Polymer Electrolyte in H_2–O_2 Fuel Cell", *Chemical Physics Letters*, **371**, 80 (2003).

80. K. Kidena, T. Ohkubo, N. Takimoto and A. Ohira, "PFG-NMR Approach to Determining the Water Transport Mechanism in Polymer Electrolyte Membranes Conditioned at Different Temperatures", *European Polymer Journal*, **46**, 450 (2010).

81. J. G. Sargent, J. S. Lee, E. Reynaud, M. D. Gilbert and J. M. Sloan, "Study of Selectively Permeable Coatings to Textiles." in 2010 MRS Fall Meeting, Materials Research Society Symposium Proceedings, Boston, 2010.

82. H. J. Lee, "Design and Development of Anti-icing Textile Surfaces", *Journal of Materials Science*, **47**, 5114 (2012).

83. A. Schwarz, J. Hakuzimana, P. Westbroek, G. de Mey, G. Priniotakis, T. Nyokong and L. van Langenhove, "A Study on the Morphology of Thin Copper Films on Para-aramid Yarns and Their Influence on the Yarn's Electro-Conductive and Mechanical Properties", *Textile Research Journal*, **82**, 1587 (2012).

84. S. B. Vukuic, S. F. Grgac, D. Katovic and A. Katovic, "SEM Characterisation of the Cellulose Material Treated with Polycarboxylic Acid and Zeolite Nanoparticles." in 5th Biennial Conference on Advanced Materials and Nanotechnology (AMN-5), Materials Science Forum, Wellington, 2011.

85. C. Jarrell, "New Process for Coating and Laminating Face-Finished Fabrics", *Journal of Coated Fabrics*, **21**, 212 (1992).

86. S. K. Devisetti and D. W. Bousfield, "Fluid Absorption During Forward Roll Coating of Porous Webs", *Chemical Engineering Science*, **65**, 3528 (2010).

87. B. Ninness, D. W. Bousfield and N. G. Triantafillopoulos, "Fluid Dynamics Model of the Film-fed Rolling Nip with a Porous Web." in Coating/Papermakers Conference, New Orleans, 1998.

88. P. Letzelter and D. Eklund, "Coating Color Dewatering in Blade Coaters - Part 1: Mathematical Model and the Influence of Color Parameters", *Tappi Journal*, **76**, 63 (1993).

89. P. Letzelter and D. Eklund, "Coating Color Dewatering in Blade Coaters - Part 2: The Influence of Machine Configuration", *Tappi Journal*, **76**, 93 (1993).

90. K. S. A. Chen and L. E. Scriven, "Liquid Penetration into a Deformable Porous Substrate", *Tappi Journal*, **73**, 151 (1990).

91. A. N. Kalarakis, V. K. Michalis, E. D. Skouras and V. N. Burganos, "Mesoscopic Simulation of Rarefied Flow in Narrow Channels and Porous Media", *Transport in Porous Media*, **94**, 385 (2012).

92. S. Hirabayashi, T. Sato, K. Mitsuhori and Y. Yamamoto, "Microscopic Numerical Simulations of Suspension with Particle Accumulation in Porous Media", *Powder Technology*, **225**, 143 (2012).

93. S. Sadhukhan, P. Gouze and T. Dutta, "Porosity and Permeability Changes in Sedimentary Rocks Induced by Injection of Reactive Fluid: A Simulation Model", *Journal of Hydrology*, **450-451**, 134 (2012).

94. S. H. Tasnim, S. Mahmud and R. A. Fraser, "Modeling and Analysis of Flow, Thermal, and Energy Fields within Stacks of Thermoacoustic Engines Filled with Porous Media", *Heat Transfer Engineering*, **34**, 84 (2013).

95. J. Ghassemzadeh and M. Sahimi, "Pore Network Simulation of Fluid Imbibition into Paper During Coating-II. Characterization of Paper's Morphology and Computation of Its Effective Permeability Tensor", *Chemical Engineering Science*, **59**, 2265 (2004).

96. I. K. Dien and H. G. Elrod, "A Generalized Steady-State Reynolds Equation for Non-Newtonian Fluids, with Application to Journal Bearings", *ASME Transactions Journal Lubrication Technology*, **105**, 385 (1983).

97. J. G. Savins, "Non-Newtonian Flow through Porous Media", *Industrial and Engineering Chemistry*, **61**, 18 (1969).

98. R. H. Christopher and S. Middleman, "Power-Law Flow through a Packed Tube", *Industrial & Engineering Chemistry Fundamentals*, **4**, 422 (1965).

99. X. Ding, T. F. Fuller and T. A. L. Harris, "Predicting Fluid Penetration During Slot Coating onto Porous Substrates", *Chemical Engineering Science*, **99**, 67 (2013).

100. A. Marmur, "Kinetics of Penetration into Uniform Porous Media: Testing the Equivalent-Capillary Concept", *Langmuir*, **19**, 5956 (2003).

101. A. Marmur and R. D. Cohen, "Characterization of Porous Media by the Kinetics of Liquid Penetration: The Vertical Capillaries Model", *Journal of Colloid and Interface Science*, **189**, 299 (1997).

102. B. Lavi, A. Marmur and J. Bachmann, "Porous Media Characterization by the Two-Liquid Method: Effect of Dynamic Contact Angle and Inertia", *Langmuir*, **24**, 1918 (2008).

103. X. Ding, T. F. Fuller and T. A. L. Harris, "A Simulation Model to Approximate Penetration of a Non-Newtonian Fluid into a Porous Media During Slot Die Coating", *Journal of coatings Technology and Research*, **11**, 83 (2013).

104. W.-B. Chu, J.-W. Yang, Y.-C. Wang, T.-J. Liu, C. Tiu and J. Guo, "The Effect of Inorganic Particles on Slot Die Coating of Poly (Vinyl Alcohol) Solutions", *Journal of Colloid and Interface Science*, **297**, 215 (2006).

105. Y.-R. Chang, H.-M. Chang, C.-F. Lin, T.-J. Liu and P.-Y. Wu, "Three Minimum Wet Thickness Regions of Slot Die Coating", *Journal of Colloid and Interface Science*, **308**, 222 (2007).

106. H.-M. Chang, Y.-R. Chang, C.-F. Lin and T.-J. Liu, "Comparison of Vertical and Horizontal Slot Die Coatings", *Polymer Engineering and Science*, **47**, 1927 (2007).

107. W.-B. Chu, J.-W. Yang, T.-J. Liu, C. Tiu and J. Guo, "The Effects of PH, Molecular Weight and Degree of Hydrolysis of Poly (Vinyl Alcohol) on Slot Die Coating of PVA Suspensions of TIO2 and SIO2", *Colloids and Surfaces A: Physicochem. Eng. Aspects*, **302**, 1 (2007).

108. C. K. Yang, D. S. H. Wong and T. J. Liu, "The Effects of Polymer Additives on the Operating Windows of Slot Coating", *Polymer Engineering and Science*, **44**, 1970 (2004).

109. W.-J. Yu and T.-J. Liu, "Reduction of the Minimum Wet Thickness in Extrusion Slot Coating", *Chemical Engineering Science*, **50**, 917 (1995).

110. S. H. Lee, H. J. Koh, B. K. Ryu, S. J. Kim, H. W. Jung and J. C. Hyun, "Operability Coating Windows and Frequency Response in Slot Coatings Flows from a Viscocapillary Model", *Chemical Engineering Science*, **66**, 4953 (2011).

111. J. Nam and M. S. Carvalho, "Two-layer Tensioned-web-over-slot Die Coating: Effect of Operating Conditions on Coating Window", *Chemical Engineering Science*, **65**, 4065 (2010).

112. O. J. Romero, L. E. Scriven and M. S. Carvalho, "Slot Coating of Mildly Viscoelastic Liquids", *Journal of Non-Newtonian Fluid Mechanics*, **138**, 63 (2006).

113. K. J. Ruschak, "Limiting Flow in a Pre-metered Coating Device", *Chemical Engineering Science*, **31**, 1057 (1976).

114. L. Landau and B. Levich, "Dragging of a Liquid by a Moving Plate", *Acta Physicochim. URSS*, **17**, 42 (1942).

115. B. G. Higgins and L. E. Scriven, "Capillary Pressure and Viscous Pressure Drop Set Bounds on Coating Bead Operability", *Chemical Engineering Science*, **35**, 673 (1980).

116. K. L. Bhamidipati, "Detection and Elimination of Defects During Manufacturing of High Temperature Polymer Electrolyte Membranes", *Ph.D. dissertation* (2011).

117. E. B. Gutoff and C. E. Kendrick, "Low Flow Limits of Coatability on a Slide Coater", *AIChE Journal*, **33**, 141 (1987).

118. H. J. Busscher, A. W. J. V. Pelt, P. D. Boer, H. P. D. Jong and J. Arends, "The Effect of Surface Roughening of Polymers on Measured Contact Angles of Liquids", *Colloids and Surfaces*, **9**, 319 (1984).

119. C. J. v. Oss, R. J. Good and M. K. Chaudhury, "Additive and Nonadditive Surface Tension Components and the Interpretation of Contact Angles", *Langmuir*, **4**, 884 (1988).

120. M. L. Sheely, "Glycerol Viscosity Tables", *Industrial & Engineering chemistry*, **24**, 1060 (1932).

121. P. Cheng, D. Li, L. Boruvka, Y. Rotenberg and A. W. Neumann, "Automation of Axisymmetric Drop Shape Analysis for Measurements of Interfacial Tensions and Contact Angles", *Colloids and Surfaces*, **43**, 151 (1990).

122. R. Flückiger, S. A. Freunberger, D. Kramer, A. Wokaun, G. G. Scherer and F. N. Büchi, "Anisotropic, Effective Diffusivity of Porous Gas Diffusion Layer Materials of Pefc", *Electrochimica Acta*, **54**, 551 (2008).

123. J. Lobato, P. Cañizares, M. A. Rodrigo, C. Ruiz-López and J. J. Linares, "Influence of the Teflon Loading in the Gas Diffusion Layer of PBI-Based PEM Fuel Cells", *Journal of Applied Electrochemistry*, **38**, 793 (2008).

124. A. Tamayol, F. McGregor and M. Bahrami, "Single Phase through-Plane Permeability of Carbon Paper Gas Diffusion Layers", *Journal of Power Sources*, **204**, 94 (2012).

125. J. T. Gostick, M. W. Fowler, M. A. Ioannidis, M. D. Pritzker, Y. M. Volfkovich and A. Sakars, "Capillary Pressure and Hydrophilic Porosity in Gas Diffusion Layers for Polymer Electrolyte Fuel Cells", *Journal of Power Sources*, **156**, 375 (2006).

126. J. T. Gostick, M. A. Ioannidis, M. W. Fowler and M. D. Pritzker, "Pore Network Modeling of Fibrous Gas Diffusion Layers for Polymer Electrolyte Membrane Fuel Cells", *Journal of Power Sources*, **173**, 277 (2007).

127. H. S. Wiklund and T. Uesaka, "Microfluidics of Imbibition in Random Porous Media", *Physical Review E*, **87**, 023006 (2013).

128. M. V. Williams, E. Begg, L. Bonville, H. R. Kunz and J. M. Fenton, "Characterization of Gas Diffusion Layers for PEMFC", *Journal of Electrochemical Society*, **151**, A1173 (2004).

129. J. D. Fairweather, P. Cheung and D. T. Schwartz, "The Effects of Wetproofing on the Capillary Properties of Proton Exchange Membrane Fuel Cell Gas Diffusion Layers", *Journal of Power Sources*, **195**, 787 (2010).

130. B. Gao, T. S. Steenhuis, Y. Zevi, J.-Y. Parlange, R. N. Carter and T. A. Trabold, "Visualization of Unstable Water Flow in a Fuel Cell Gas Diffusion Layer", *Journal of Power Sources*, **190**, 493 (2009).

131. J. Benziger, J. Nehlsen, D. Blackwell, T. Brennan and J. Itescu, "Water Flow in the Gas Diffusion Layer of PEM Fuel Cells", *Journal of Membrane Science*, **261**, 98 (2005).

132. Z. Fishman, J. Hinebaugh and A. Bazylak, "Microscale Tomography Investigations of Heterogeneous Porosity Distributions of PEMFC GDLs", *Journal of Electrochemical Society*, **157**, B1643 (2010).

133. A. B. D. Cassie and S. Baxter, "Wettability of Porous Surfaces", *Faraday Soc. Trans.*, **40**, 546 (1944).